Synchrotron Radiation-Based X-ray Photoelectron Spectroscopy

Dr. Chia-Hsin Wang (王嘉興)

08 Oct, 2025

National Synchrotron Radiation Research Center

Outline

- **The Basic Principle of X-ray Photoelectron Spectroscopy**
- **The Applications of Synchrotron-Based Photoelectron Spectroscopy**
- **Introduction of Ambient Pressure X-ray Photoelectron Spectroscopy (APXPS)**
- **APXPS End Station and Its Applications at NSRRC**
- **XPS peak fitting**

X-ray Photoelectron Spectroscopy

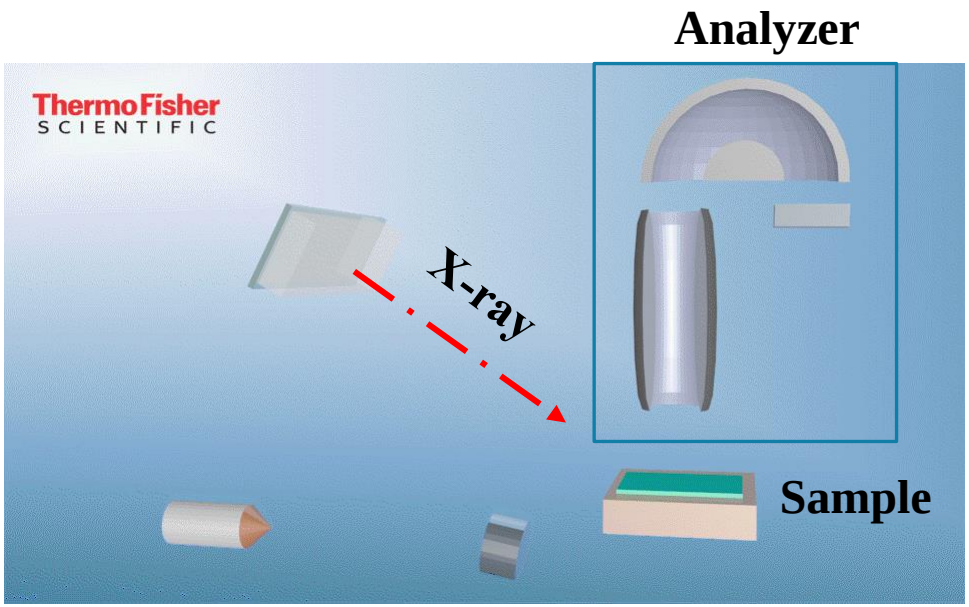

https://xpssimplified.com/whatisxps.php

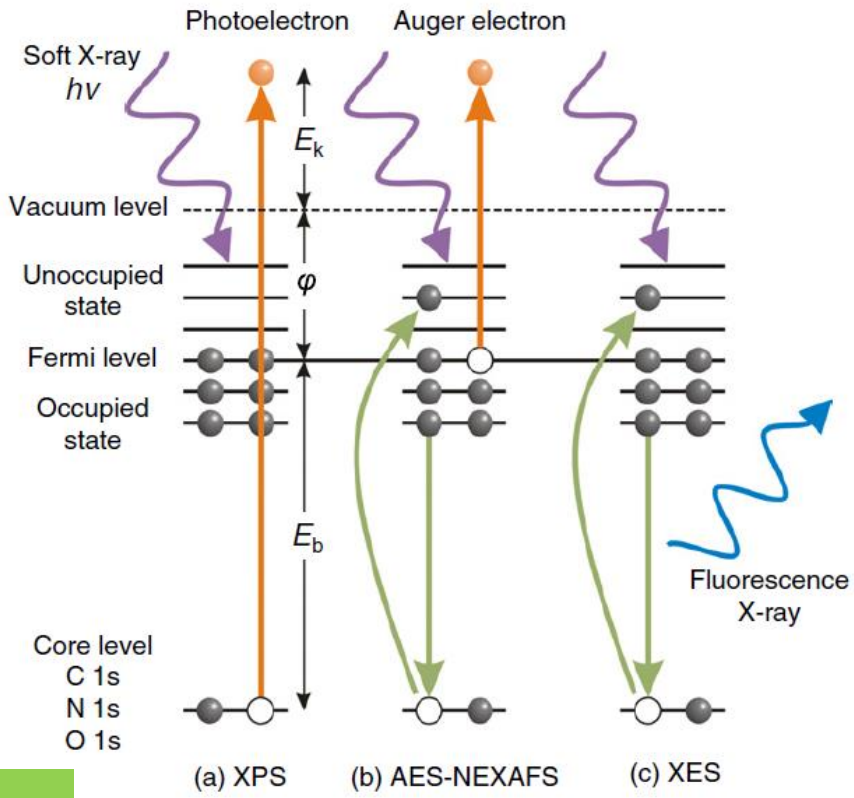

J. Phys.: Condens. Matter **2015**, *27*, 083003

Photoelectric effect
Einstein, Nobel Prize 1921

Photoemission as an analytical tool
Kai Siegbahn, Nobel Prize 1981

Energy conservation law:
$E'_{kin} = h\nu - E_b - \phi_s$

Conventional XPS needs to be performed in an environment better than high-vacuum to eliminate the electron-gaseous molecule scattering problem and be used to study the chemical state and elemental composition of surface layers in solid samples.

Keys to the elemental analyses: electronic binding energies of the elements

Table 1. Line Positions[a)] from Mg X-rays, by Element

Element	Atomic No.	Range (eV)	Photoelectron Lines[b)] 1s	2s	$2p_1$	$2p_3$	3s	$3p_1$	$3p_3$	$3d_3$	$3d_5$	4s	$4p_1$	$4p_3$	Range (eV)	Auger Lines KL_1L_1	KL_1L_{23}	$KL_{23}L_{23}$[c)]	$L_3M_{23}M_{23}$[d)]	$L_2M_{23}M_{23}$[d)]	$L_3M_{23}M_{45}$ ^1P	$L_3M_{23}M_{45}$ ^3P	$L_2M_{23}M_{45}$ ^1P	$L_3M_{45}M_{45}$[e)]	$L_2M_{45}M_{45}$
Li	3		56																						
Be	4	4	113																						
B	5	8	191															1082							
C	6	12	287															993							
N	7	9	402												12			875							
O	8	4	531	23											10		779	764	743						
F	9	6	686	30											8		645	626	599						
Ne	10	0	863	41	14										0		491	468	435						
Na	11	2	1072	64	31										4		332	303	264						
Mg	12	2		90	51																				
Al	13	4		119	74																				
Si	14	6		153	103	102																			
P	15	8		191	134	133	14																		
S	16	8		229	166	165	17								6				1103						
Cl	17	11		270	201	199	17								4				1071						
Ar	18	0		319	243	241	22								0	1037		1035							
K	19	1		378	296	293	33	17								1005		1003							
Ca	20	2		439	350	347	44	25								964		961							
Sc	21	6		501	407	402	53	31							8				920		892				
Ti	22	8		565	464	458	62	37							10				873		839				
V	23	6		630	523	515	69	40							6				822		784				
Cr	24	6		698	586	577	77	46	45										767		729				
Mn	25	4		770	652	641	83	49	48						6				715		670			620	
Fe	26	8		847	723	710	93	56	55						6				659		608			553	
Co	27	6		927	796	781	103	63	61						7	604		597			546		541	483	468
Ni	28	6		1009	873	855	112	69	67						7	548		542			482		476	410	393
Cu	29	4		1098	954	934	124	79	77						5	486		479			416		408	337	317
Zn	30	2		1196	1045	1022	140	92	89	10					7	429		422			352		343	265	242
Ga	31	2			1144	1117	160	108	105	20					7	368		361			284		275	189	162
Ge	32	4					184	128	124	32	31				10	305		297			215		205	113	82
As	33	7					207	148	143	45	44														
Se	34	8					232	169	163	58	57														
Br	35	7					256	189	182	70	69														
Kr	36	0					287	216	208	89	88	22													
Rb	37	1					322	247	238	111	110	29		14											
Sr	38						358	280	269	135	133	37		20											
Y	39						395	313	301	160	158	45		25											
Zr	40	6					431	345	331	183	181	51		29											

Handbook of X-Ray Photoelectron Spectroscopy, J.F. Moulder et al., Physical Electronics, Inc., Eden Prairie, MN, USA (1992)

Binding Energy

Koopman's Theorem

The BE of an electron is simply the difference between the initial state (atom with n electrons) and final state (atom with n-1electrons (ion) and free photoelectron)

$$BE = E_{final}(n-1) - E_{initial}(n)$$

If no relaxation* followed photoemission, BE = - orbital energy, which can be calculated from Hartree Fock. *this "relaxation" refers to electronic rearrangement following photoemission – not to be confused with relaxation of surface atoms.

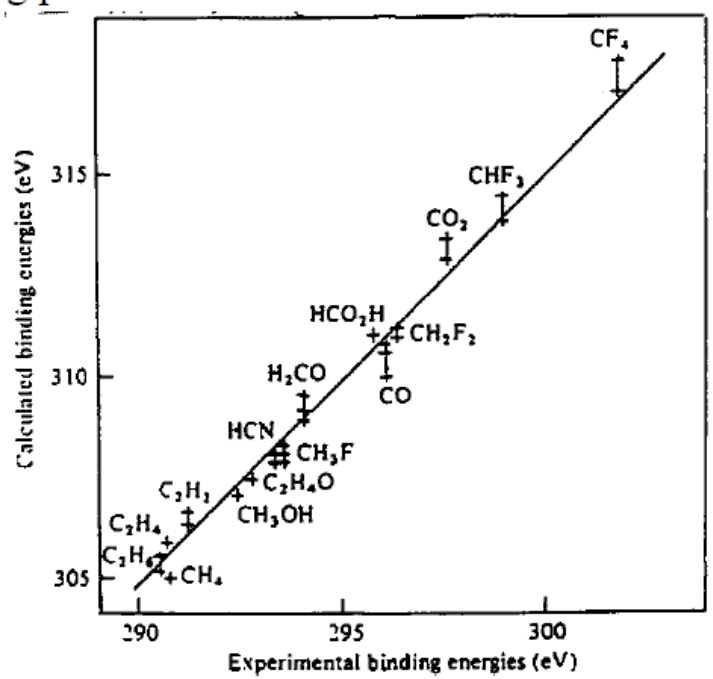

Binding energy shift vs. the localized charge on a core level

- Neglect electronic relaxation in the core-ionized final state.
- In the "charge potential model," the observed binding energy E_B is related to a reference energy E_B^0 (neutral atom), the charge q_i on atom i, and the charge q_j of the surrounding atoms j at distance r_{ij}, as follows:

$$E_B^i = E_B^{i,0} + Kq_i + \sum_{j \neq i} (q_j / r_{ij})$$

where k is a constant.

$$\Delta E_B = \Delta \varepsilon_k = \Delta q + \Delta V$$

Δq: change of charge (oxidation state)

ΔV: surrounding potential change

Binding Energy Shifts (Chemical shifts)

Chemical Shifts- Electronegativity Effects

Functional Group		***Binding Energy (eV)***
hydrocarbon	C-H, C-C	285.0
amine	C-N	286.0
alcohol, ether	C-O-H, C-O-C	286.5
Cl bound to C	C-Cl	286.5
F bound to C	C-F	287.8
carbonyl	C=O	288.0

Initial State Effect

Features observed in XPS spectra

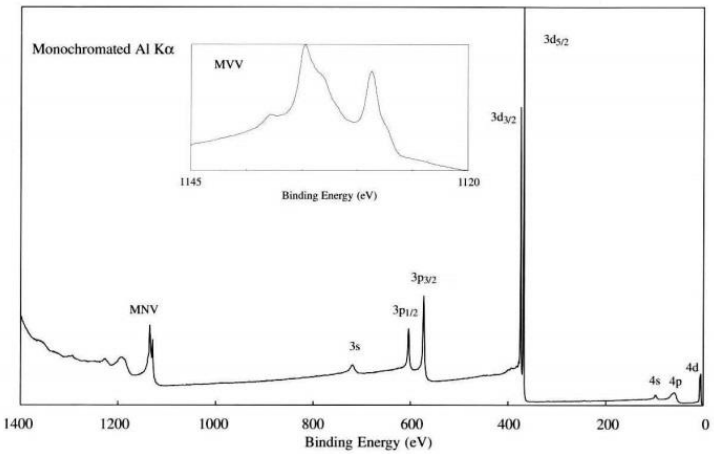

1.Photoemission peaks
- •Intense & Narrow
- •Shifted by the chemical effect

2.X-ray satellite peaks
- •Not observed with a monochromatized source
- •Always the same energy shift from the photoemission peak

3. Photon-induced Auger lines
4. Inelastic scattering background
5. *Valence band features*
6. Spin-orbit coupling
7. Multiples splitting
8.*Shake-up satellites and shake-off satellites
9.*Plasmon loss peaks

(*Loss process)

Spin-orbit (j-j) coupling

All core levels except the s levels ($l = 0$) give rise to a doublet with the two possible states having different binding energies.

l : angular momentum number,
s: spin momentum number

***j-j* coupling :**

individual electron l-s coupling

d-shell electron (or hole) $l = 2$; $s = 1/2$

$j = l \pm s = 3/2$ and $5/2$

degeneracy of the final states; $g_j = 2j + 1$

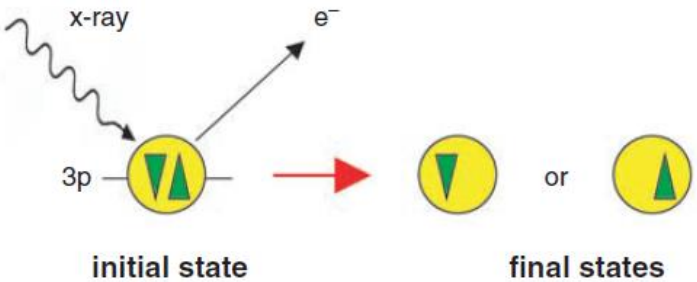

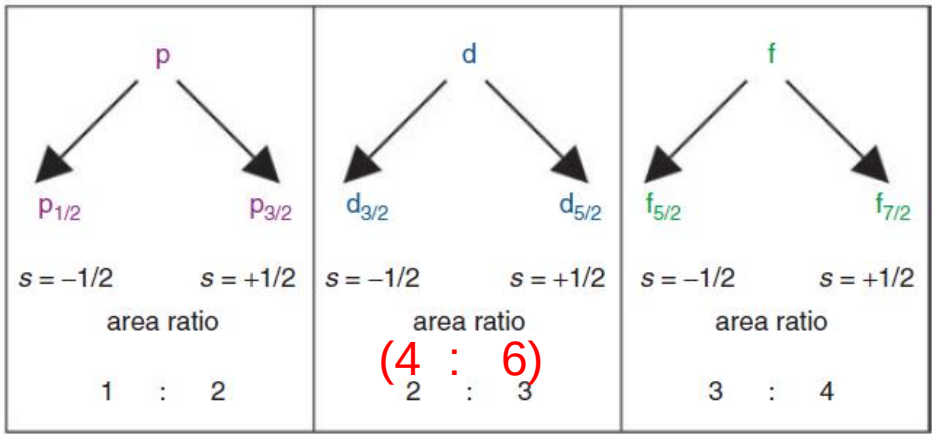

Figure 3.12 After electron emission from a 3p orbital subshell, the remaining electron can have a spin-up or spin-down state. Magnetic interaction between these electrons and the orbital angular momentum may lead to spin–orbit coupling

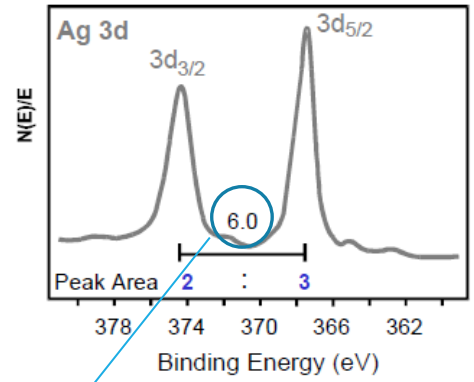

***d* orbital**
l = 2
s = ± 1/2
ls = 3/2, 5/2

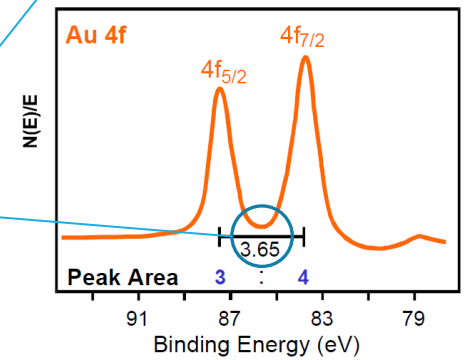

***f* orbital**
l=3
s= ± 1/2
ls=5/2, 7/2

Spin-orbit splitting value

Spin orbital splitting and peak area ratios assist in element identifications

Final State Effect

Relaxation effects can have a significant impact on the measured E_B. In all cases the **electron rearrangements** (core hole) that occur during photoemission result in the lowering of E_B. (Cu, Co, Ni….)

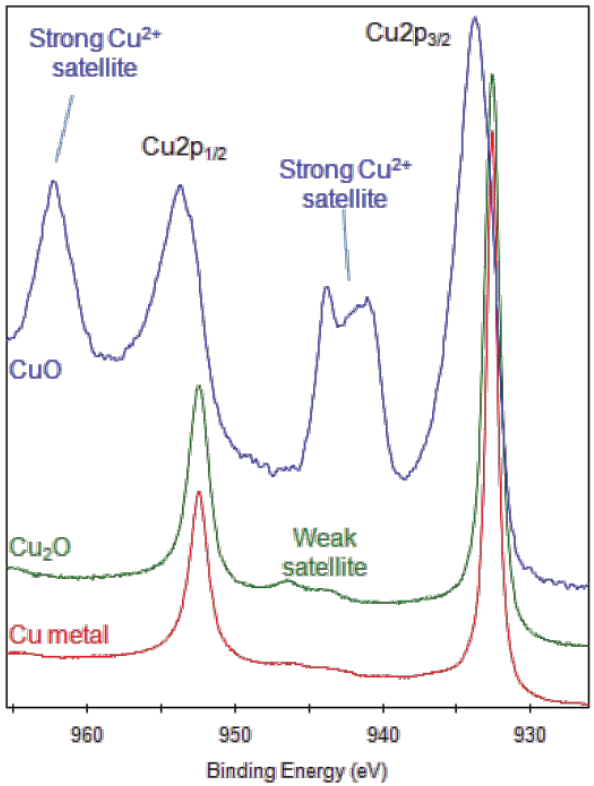

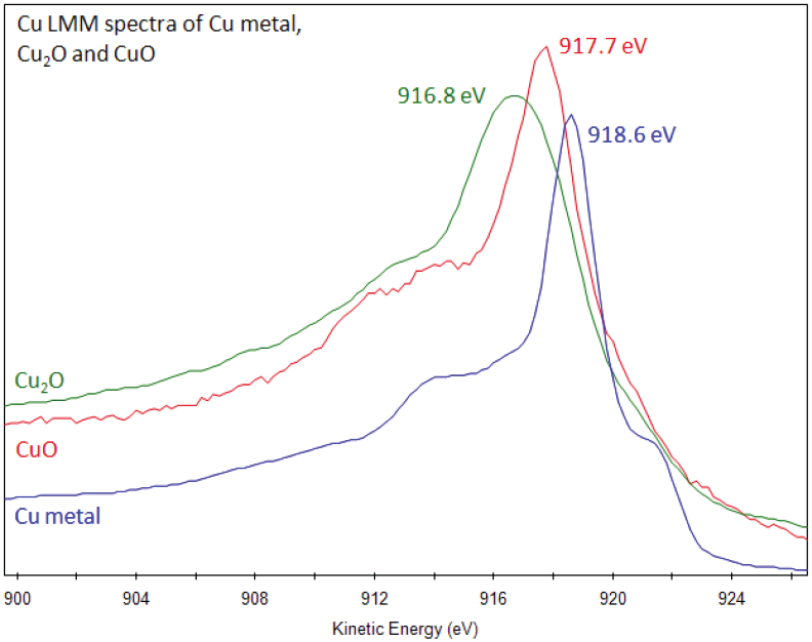

metallic Cu (Cu^0) and Cu_2O (Cu^{+1}) have the similar E_b

https://xpssimplified.com/elements/copper.php

Multiplet splitting

Multiplet splitting arises when an atom contains unpaired electrons (e.g. Cr(III), $3p^6 3d^3$). When a core electron vacancy is created by photoionization, there can be coupling between the unpaired electron in the core with the unpaired electrons in the outer shell. This can create a number of final states, which will be seen in the photoelectron spectrum as a multi-peak envelope.

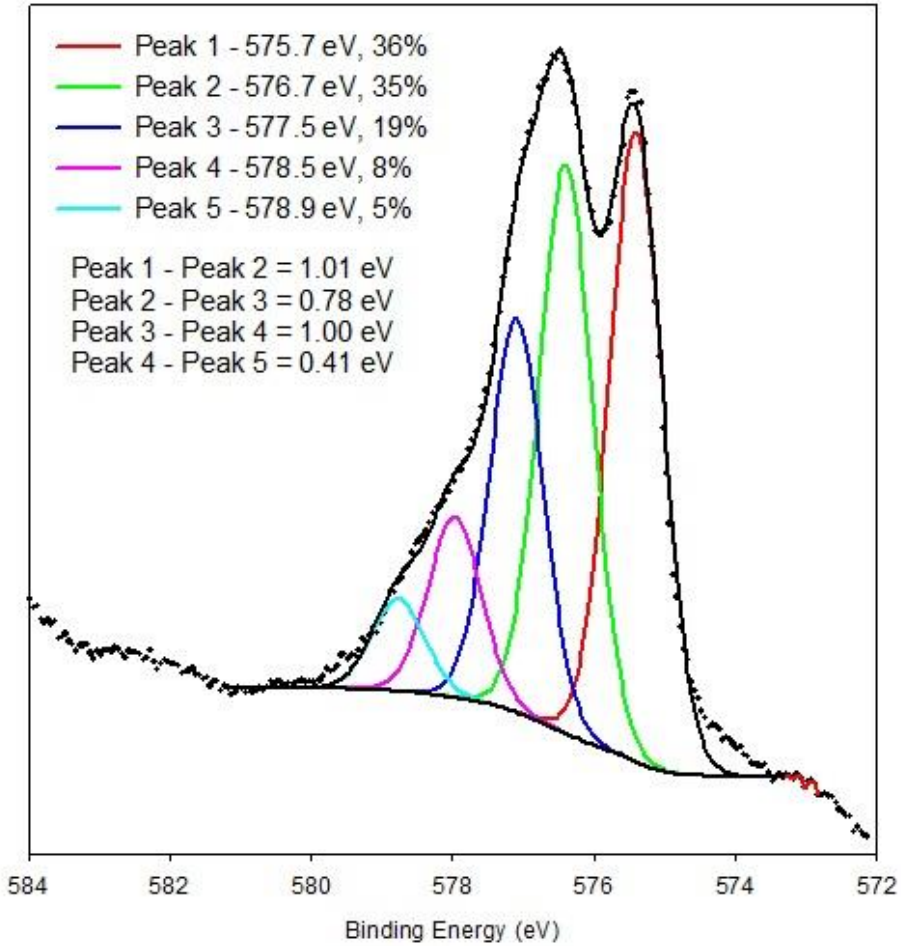

Photoelectron spectrum with shake-up and shake-off satellites

Shake-up: Photoelectrons have lost energy through promotion of valance electrons form an occupied energy level to an unoccupied higher level

Shake-off: Departing photoelectron transfers sufficient energy into the valance electron to ionize it into continuum state

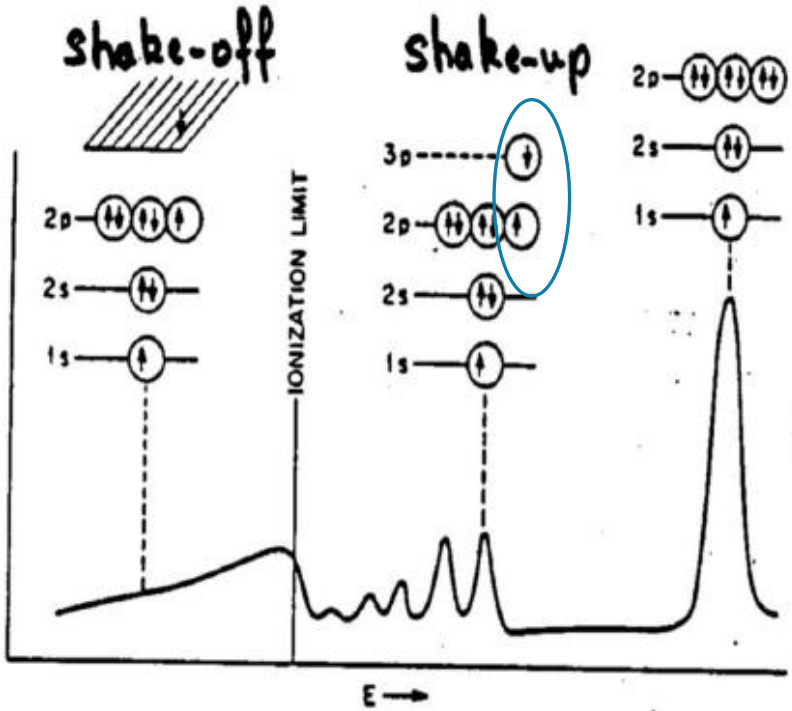

$$\Delta J = \Delta L = \Delta S = 0 \; ; \; \Delta \ell = \Delta s = 0$$

$$P_{n\ell j - n'\ell j} = \left| \int \psi^*_{n'\ell j} \, \psi_{n\ell j} \, d\tau \right|^2$$

$$\Psi_{nlm}(r,\theta,\psi) = Y_{lm}(\theta,\psi) R_n(r)$$

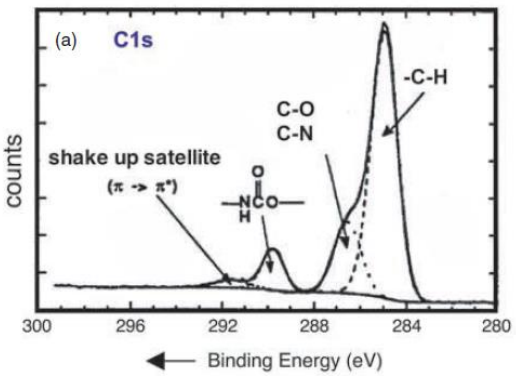

Peaks are most apparent for systems with aromatic structure, unsaturated bonds, or transition metal ions.

Plasmon loss peaks

The conduction electrons in metals, in contrast to being localized on each atom, have been likened to a ‘sea’ or continuum. Characteristic collective vibrations have been noted for this continuum of electrons and are referred to as plasmon vibrations. In some cases, the exiting photoelectron can couple with the plasmon vibrations leading to characteristic, periodic energy losses.

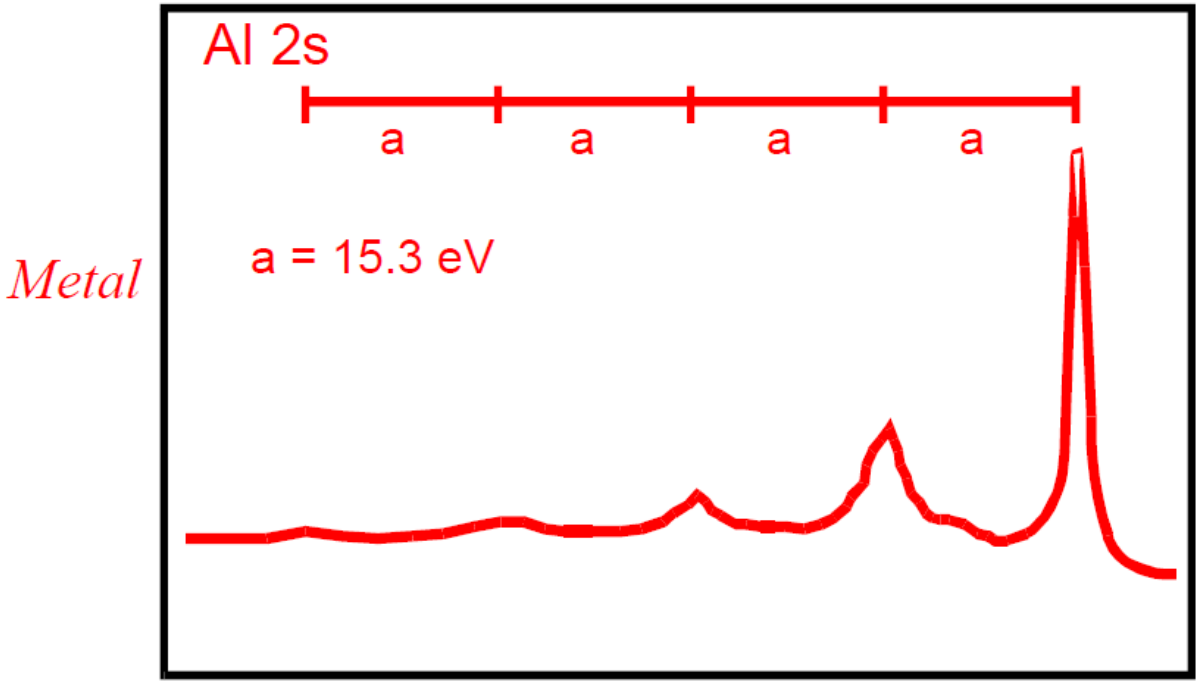

Plasmon : collective electron wave oscillation)

XPS is a powerful surface analysis technique.

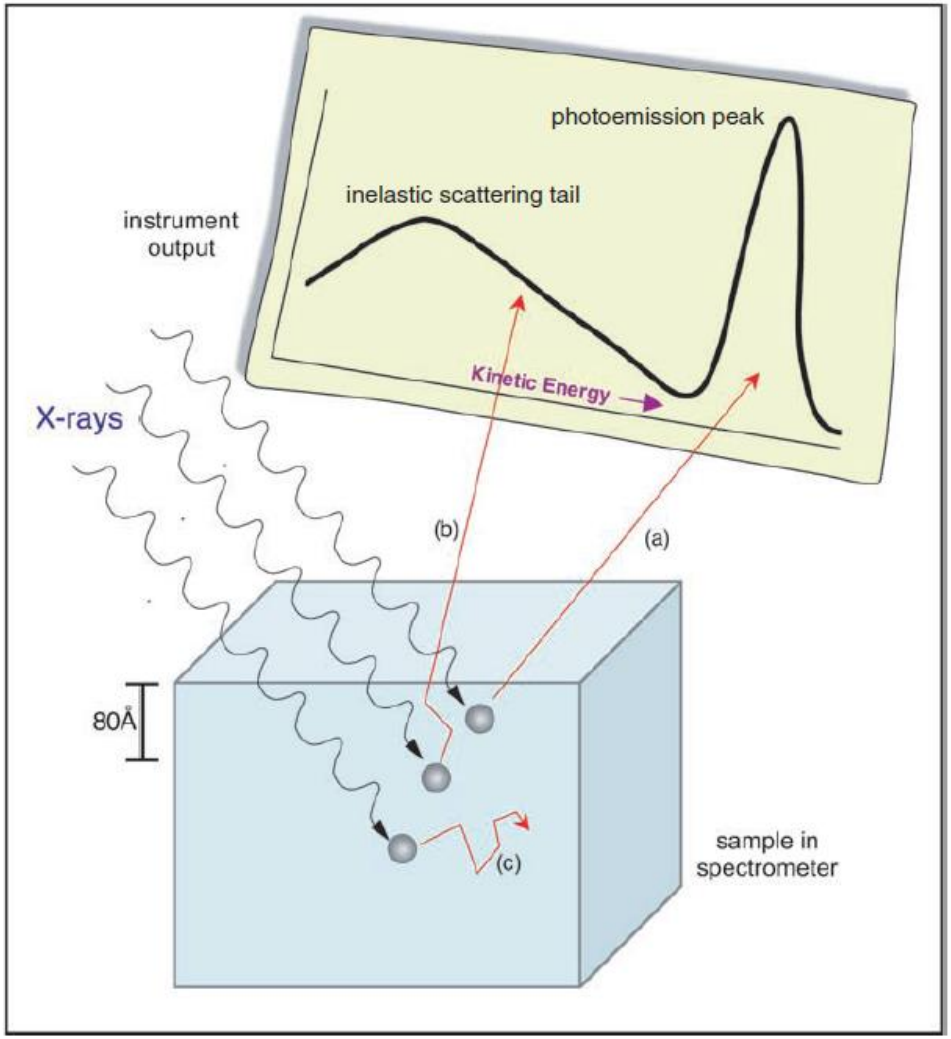

Figure 3.7 X-rays will penetrate deeply into a sample, and stimulate electron emisson throughout the specimen. Only those electrons emitted from the surface zone that have suffered no energy loss will contribute to the photoemission peak (a). Electrons emitted from the surface zone that have lost some energy due to inelastic interactions will contribute to the scattering background (b). Electrons emitted deep within a sample will lose all their kinetic energy to inelastic collisions and will not be emitted (c)

Table 1.2 Penetration depths of particles

Particle	Energy (eV)	Depths (Å)
Photon	1000	10 000
Electron	1000	20
Ions	1000	10

Inelastic Mean Free Path and Sampling Depth

Beer-Lambert law (or Beer's law) : the relationship between absorbance and concentration of an absorbing species.

- Inelastic Mean Free Path (λ):

The average distance that an electron with a given energy travels through a solid before losing energy.
(depend on density, composition, and structure of the material being analyzed)

- Sampling Depth: (θ = 0 ˚)
  = 3λ

(the depth from which 95% of the photoemission has taken place.)

- Most λ's are in the range of 1 – 3.5 nm for Al Kα radiation

- So the sampling depth (3λ) for XPS under these conditions is 3-10 nm

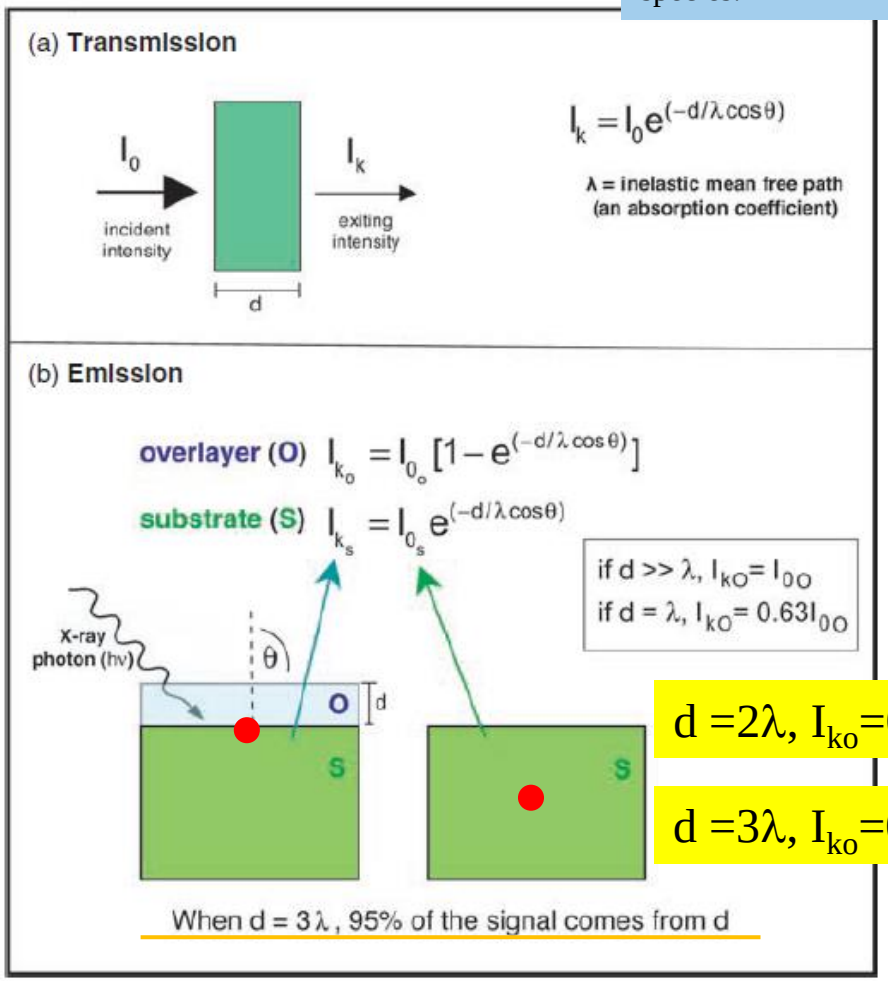

$d = 2\lambda$, $I_{ko} = 0.84 I_{0o}$

$d = 3\lambda$, $I_{ko} = 0.95 I_{0o}$

Figure 3.8 (a) For electrons transmitted through a sample, Beer's law of molecular absorption explains the total intensity loss for electrons that lose no energy in traversing the sample. (b) For electron emission from a thick sample, modifications of Beer's law can explain the photoemission intensity from an overlayer or from the substrate covered by an overlayer

Inelastic Mean free path of electrons (λ) in different solids as a function of kinetic energy of electrons (universal curve), a key to surface sensitivity

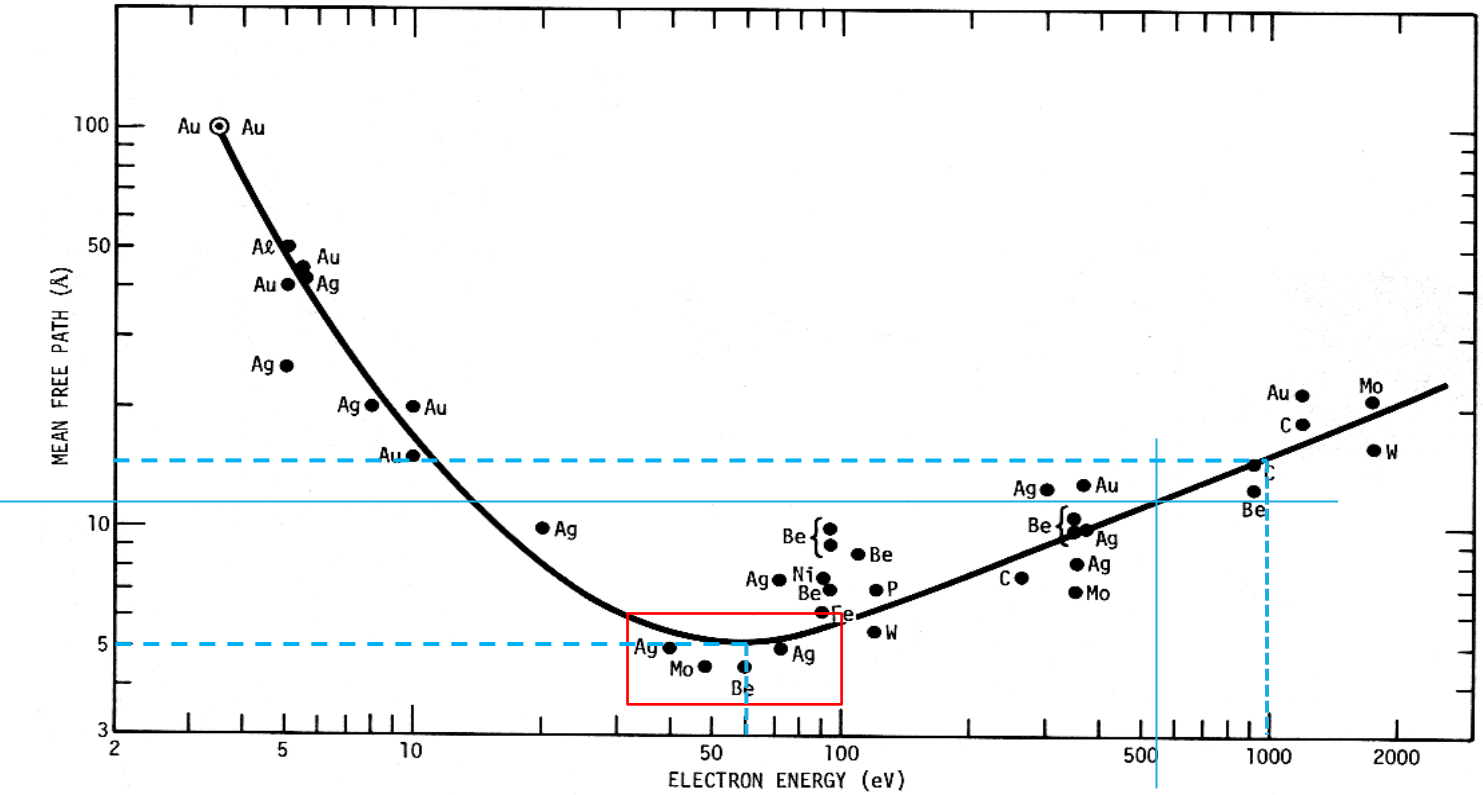

Figure 5.11. The mean free path of electrons in different solids as a function of the kinetic energy of the electrons [56].

Surface senesitive:
$h\nu = E_b + 30\sim100$ eV

λ; the average distance travelled by a given electron between two successive collisions with the other electrons of the solid atoms.

Peak widths and Intensities

Peak widths: The contributions that the intrinsic and instrumental effects make to the peak width are given, to a first approximation, by:

$$\mathrm{FWHM_{tot}} = (\mathrm{FWHM}_n^2 + \mathrm{FWHM}_x^2 + \mathrm{FWHM}_a^2 + \mathrm{FWHM}_{ch}^2 + \cdots)^{1/2} \quad (3.12)$$

where FWHM is the full-width at half-maximum of the observed peak (tot), core hole lifetime (n), X-ray source (x), analyzer (a), and charging contribution (ch).

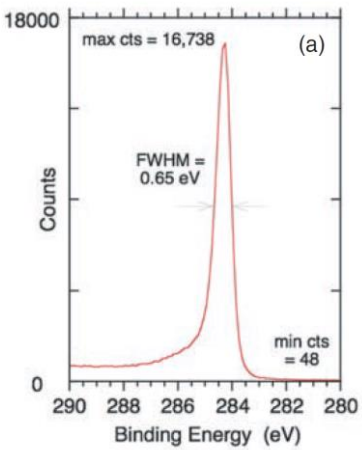

Table 2.1 Energies and widths of some characteristic soft X-ray lines

Line	Energy, eV	Width, eV
Y $M\zeta$	132.3	0.47
Zr $M\zeta$	151.4	0.77
Nb $M\zeta$	171.4	1.21
Mo $M\zeta$	192.3	1.53
Ti $L\alpha$	395.3	3.0
Cr $L\alpha$	572.8	3.0
Ni $L\alpha$	851.5	2.5
Cu $L\alpha$	929.7	3.8
Mg $K\alpha$	1253.6	0.7
Al $K\alpha$	1486.6	0.85
Si $K\alpha$	1739.5	1.0
Y $L\alpha$	1922.6	1.5
Zr $L\alpha$	2042.4	1.7
Ti $K\alpha$	4510.0	2.0
Cr $K\alpha$	5417.0	2.1
Cu $K\alpha$	8048.0	2.6

Al $K_{\alpha 1}$ with quartz monochromator: ~0.3 eV

Synchrotron X-ray

: Resolving Power

E/dE= 8000 ~ 10000

(BL24A @ NSRRC)

E= 400 eV,
dE= 400/8000=0.05 eV

Thermal broadening: 0.1 eV at 300 K

Analyzer

HEMISPHERICAL ENERGY ANALYZER (HSA)

Fig. 3.7. Cross-sectional view of a hemispherical electron spectrometer.

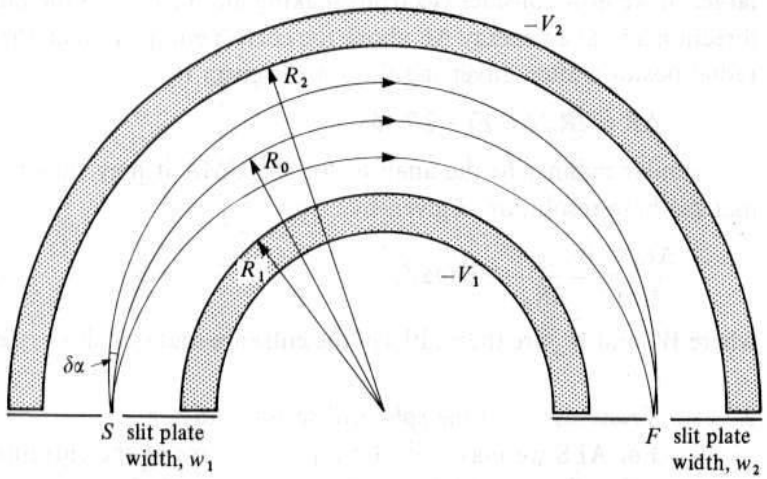

Fig. 3.9. Two possible multichannel output systems for spherical sector spectrometers.

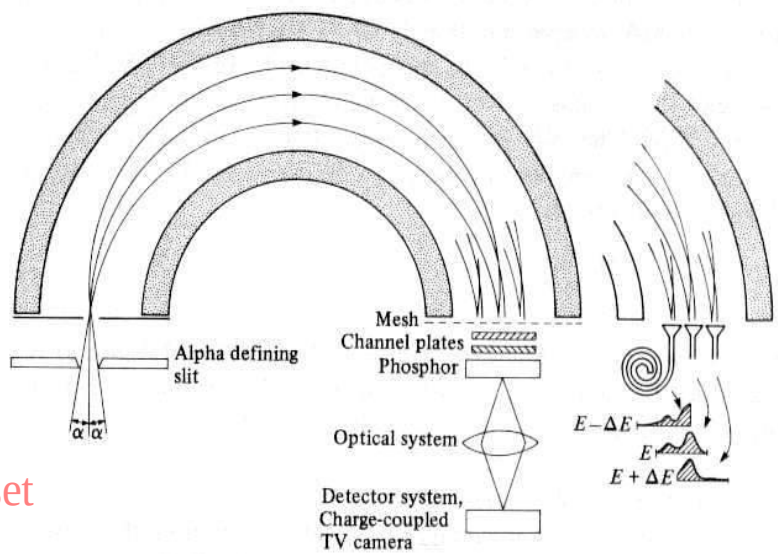

To detect electrons of E_k energy at a pass energy of E_p, set

$$V_2 = -|E_k| + \frac{R_1}{R_2}E_p, \quad V_0 = -|E_k| + E_p, \quad V_1 = -|E_k| + \frac{R_2}{R_1}E_p$$

Note: V_2, V_0, and V_1 are neg., but E_k and E_p pos.

Energy resolution:

$$\frac{\Delta E}{E_{pass}} = \frac{(w_1 + w_2)/2}{2R_0} + \frac{\alpha^2}{4}$$

Where E_{pass} is the *pass energy* of the analyzer, R_0 is the *mean radius* (= ½(R_{in}+R_{out})), w_1 and w_2 are the *widths of entrance and exit slits*, respectively, α is the *half acceptance angle* in dispersion direction.

The C1s spectrum (resolved into component peaks) for the hard-segment polyurethane

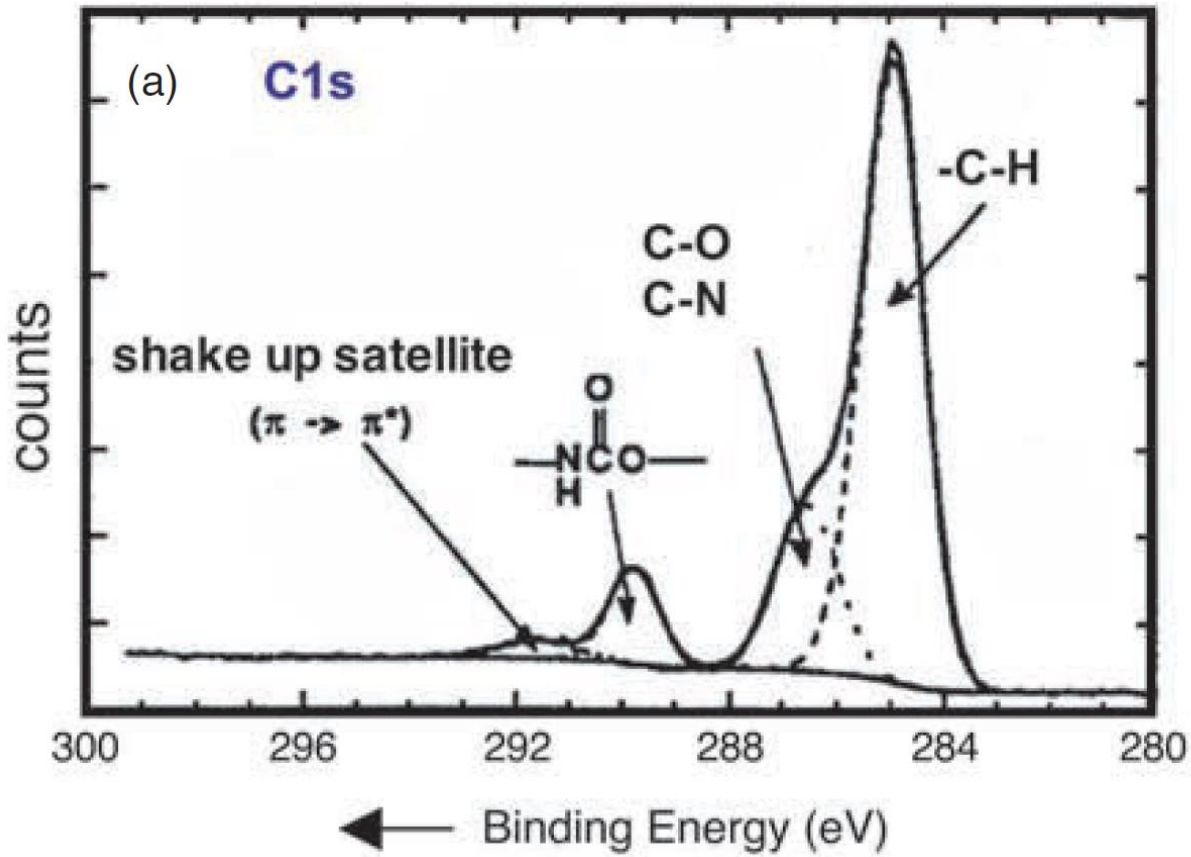

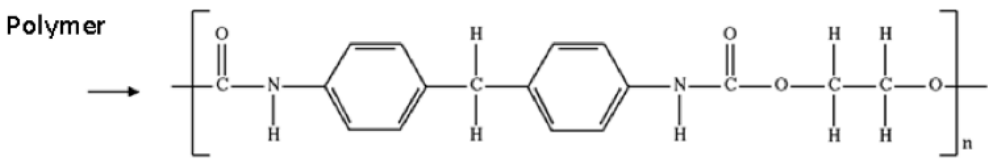

Polyurethane

Intensities

For a Homogeneous sample:

$$\mathbf{I = N \cdot \sigma \cdot D \cdot J \cdot \theta \cdot \lambda \cdot A \cdot T}$$

where: N = atoms/cm^3, the number of atoms of the element per cm^3

σ = photoelectric cross-section for the atomic orbital of interest in cm^2

D = detector efficiency

J = X ray flux, photon/cm sec X-cm^2-sec

θ(L) = the emission angle of the electron with respect to the surface normal

λ = inelastic electron mean free path,

A = analysis area, cm^2

T = analyzer transmission efficiency

Fixed Photon energy

$$\mathbf{N = I/\sigma \cdot D \cdot J \cdot \theta \cdot \lambda \cdot A \cdot T}$$

Let, S = $\sigma \cdot D \cdot J \cdot \theta \cdot \lambda \cdot A \cdot T$ ----elemental sensitivity factor

$$\mathbf{N = I/S}$$

Relative Concentration (C_x) of observed elements as a number fraction by:

$$\mathbf{C_x = N_x/\sum N_x,}$$

$$\mathbf{C_x = I_x/S_x/\sum I_x/S_x,}$$

The values of S are based on empirical data (Spectrometer- dependent)

XPS of Copper-Nickel alloy

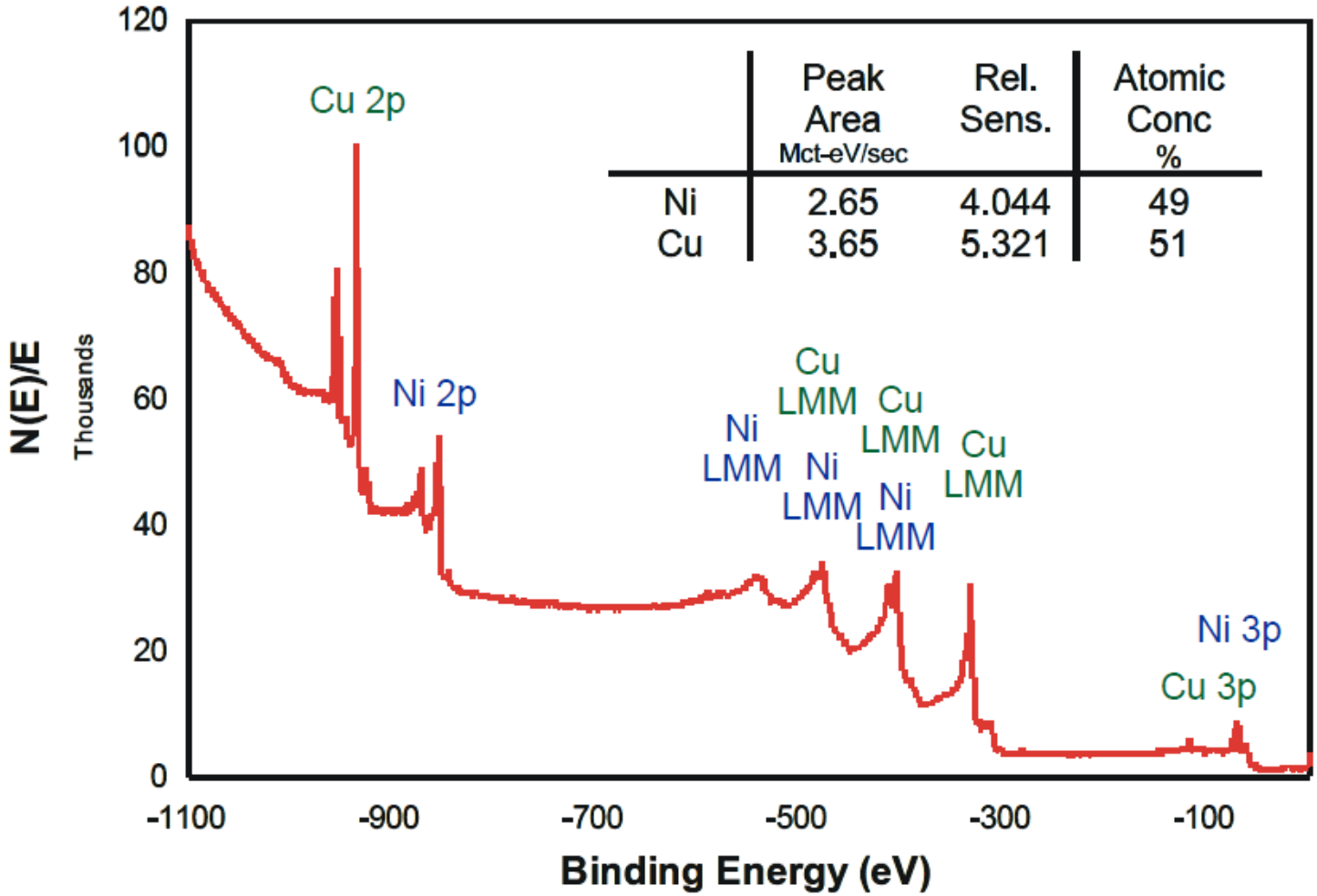

	Peak Area Mct-eV/sec	Rel. Sens.	Atomic Conc %
Ni	2.65	4.044	49
Cu	3.65	5.321	51

Depth Profiling

1. Using different X-ray energy

2.Rotating sample rod

3.Ion-sputter sample surface

maintaining the X-ray source and detector in fixed positions, the effective sampling depth decreases by a factor of cos θ

(2)

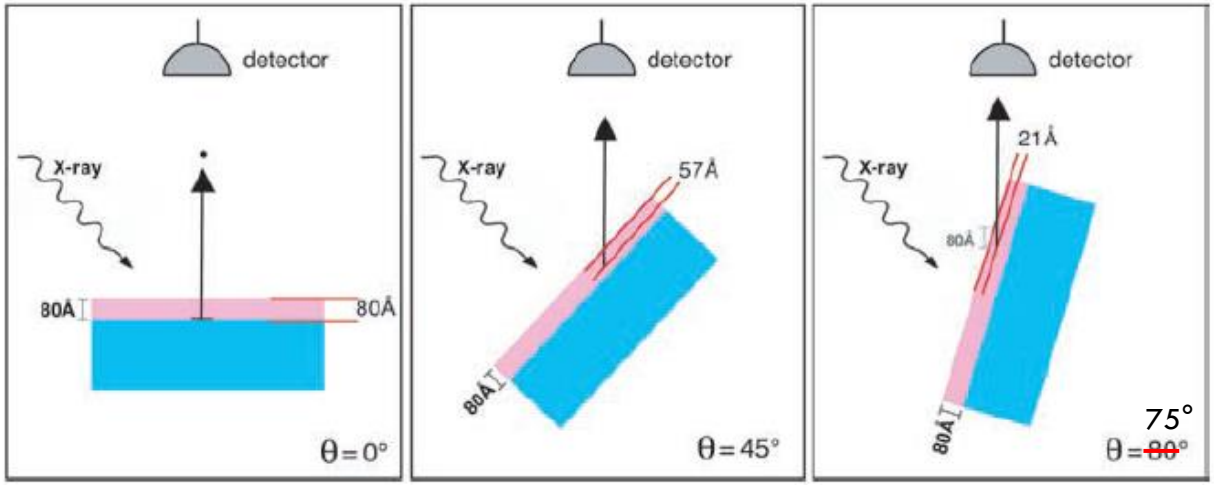

The sample angle, θ, is defined relative to the normal to the surface

(1)

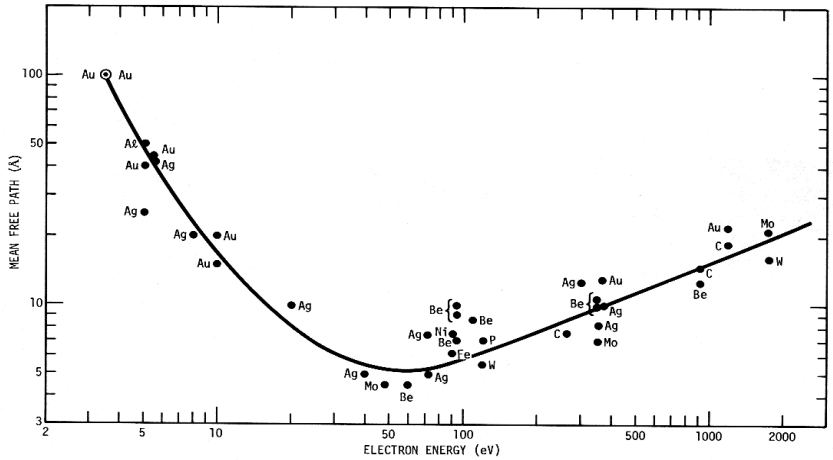

Figure 5.11. The mean free path of electrons in different solids as a function of the kinetic energy of the electrons [56].

(2)

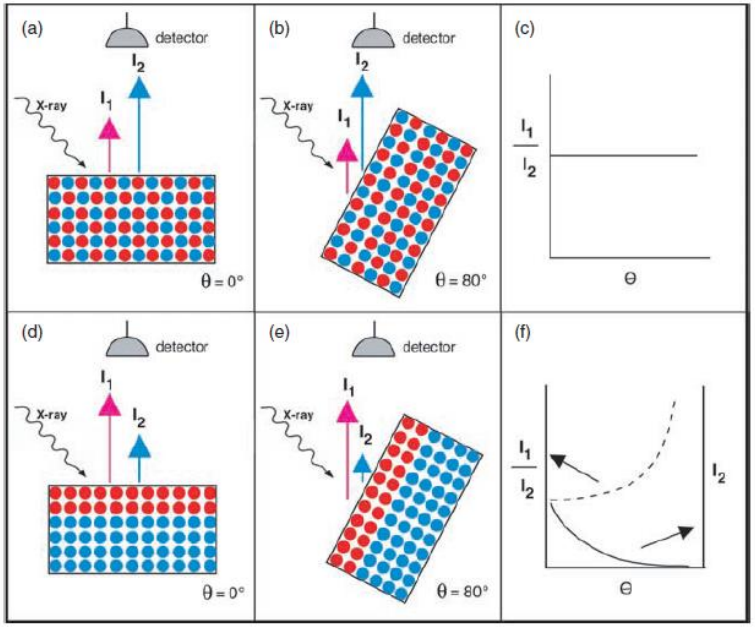

Information Provided by XPS

Table 3.1 Information derived from an ESCA experiment

In the outermost 10 nm of a surface, ESCA can provide the following:

- Identification of all elements (except H and He) present at concentrations >0.1 atomic %.
- Semiquantitative determination of the approximate elemental surface composition (error $< \pm 10\,\%$).
- Information about the molecular environment (oxidation state, covalently bonded atoms, etc.).
- Information about aromatic or unsaturated structures or paramagnetic species from shake-up ($\pi^* \rightarrow \pi$) transitions.
- Identification of organic groups using derivatization reactions.
- Non-destructive elemental depth profiles 10 nm into the sample and surface heterogeneity assessment using (1) angular-dependent ESCA studies and (2) photoelectrons with differing escape depths.
- Destructive elemental depth profiles several hundred nanometers into the sample using ion etching.
- Lateral variations in surface composition (spatial resolutions down to 5 μm for laboratory instruments and spatial resolutions down to 40 nm for sychrotron-based instruments).
- 'Fingerprinting' of materials using valence band spectra and identification of bonding orbitals.
- Studies on hydrated (frozen) surfaces.

Advantage of synchrotron radiation over lab-based x-ray sources in photoelectron spectroscopy

- High flux and brightness
- Continuous source energy
- ▲ Much higher photoionization cross section can be realized
- ▲ Surface sensitivity enhanced by selecting favorable exit kinetic energy of electrons
- High energy-resolution spectroscopy work routinely achieved
- Cleaner light, without x-ray satellites found in the lab source
- Variable polarization

Benefits from Continuous source energy

1. More Surface Sensitive

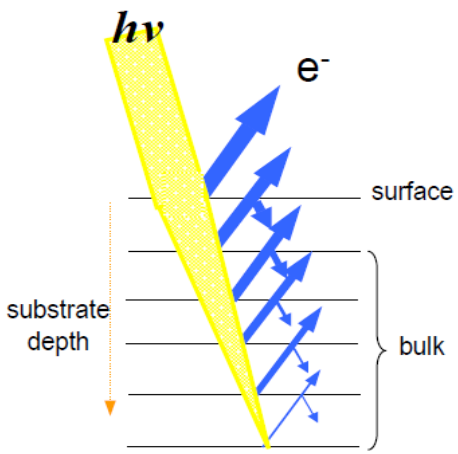

Surface senesitive :

$h\nu = E_b + 30\sim150$ eV

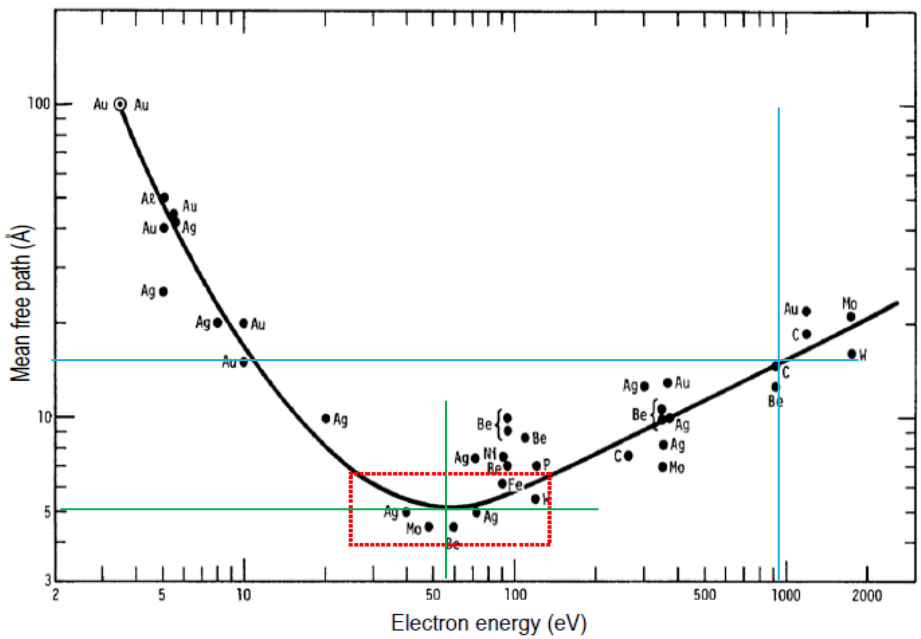

Mg K_α= 1253.6 eV, C1s binding energy =285 eV,
E_k for carbon, 968.6 eV, λ = 1.6 nm, Sampling depth = 4.8 nm

E_{SR} = 340 eV,
E_k for carbon, 55 eV, λ = 0.5 nm, Sampling depth = 1.5 nm

2. Non-destructive method for depth profiling

3. Strong photon-energy dependence of photoionization cross section

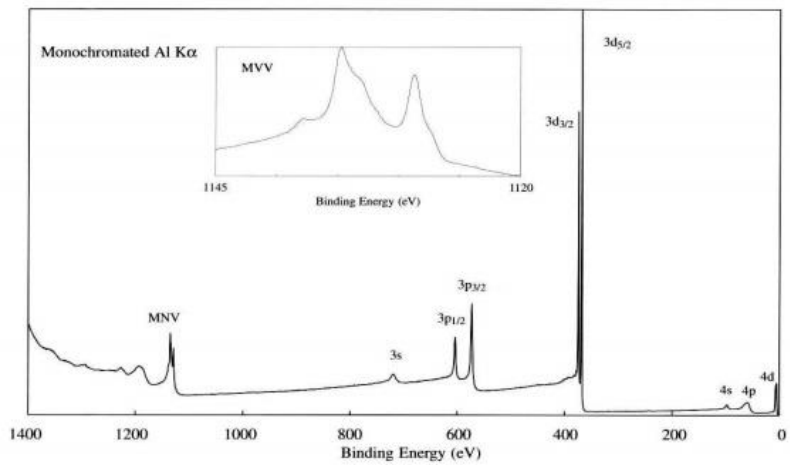

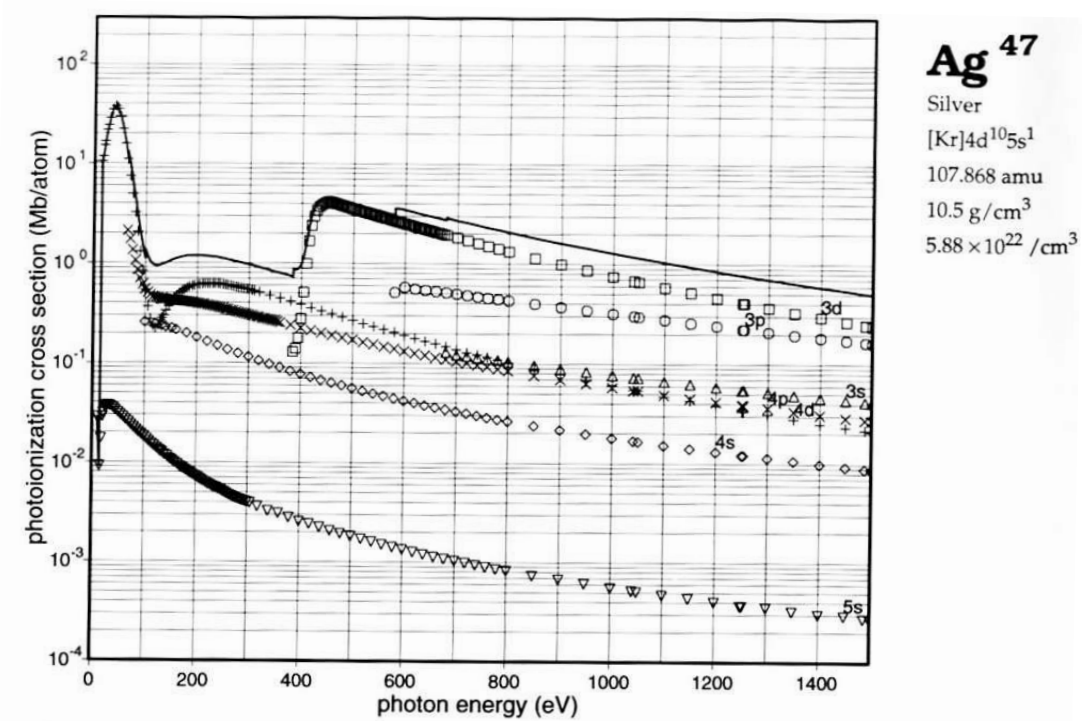

λ(Å)	1216	742	585	463	304	155	93.7	81.9	62.0	41.3	20.7	15.5	11.9	9.89	8.34
hυ(eV)	10.2	16.7	21.2	26.8	40.8	80.0	132.3	151.4	200.0	300.0	600.0	800.0	1041.0	1253.6	1486.6
(nℓ) (BE)															
3s 665.1												0.1045	0.07285	0.05493	0.04178
3p 567.2											0.5765	0.4271	0.2997	0.2225	0.1651
3d 384.4											2.503	1.329	0.6762	0.4052	0.2474
4s 94.2							0.2356	0.2222	0.1804	0.1149	0.04200	0.02622	0.01677	0.01211	.008858
4p 62.9						1.057	0.4363	0.4257	0.3974	0.3036	0.1322	0.08472	0.05410	0.03859	0.02764
4d 12.6		11.790	16.620	24.170	37.480	3.218	0.2785	0.4121	0.6052	0.5452	0.1896	0.1030	0.05517	0.03363	0.02174
5s 6.4	0.02843	0.01723	0.03113	0.03686	0.03504	0.02251	0.01287	0.01074	.007235	.003991	.001340	.000822	.000516	.000366	.000274
total	0.02843	11.810	16.650	24.210	37.520	4.298	0.9633	1.071	1.190	0.9677	3.445	2.075	1.175	0.7673	0.5128

Cross section defined as the transition probability per unit time for excitation of a single photoelectron from the core level of interest under an incident photon flux of #/cm^2•s^{-1}

Cross-section unit (from nuclear physics): barn = 10^{-24} cm^2, Mb=10^{-18} cm^2.

Photoionization cross section of Li

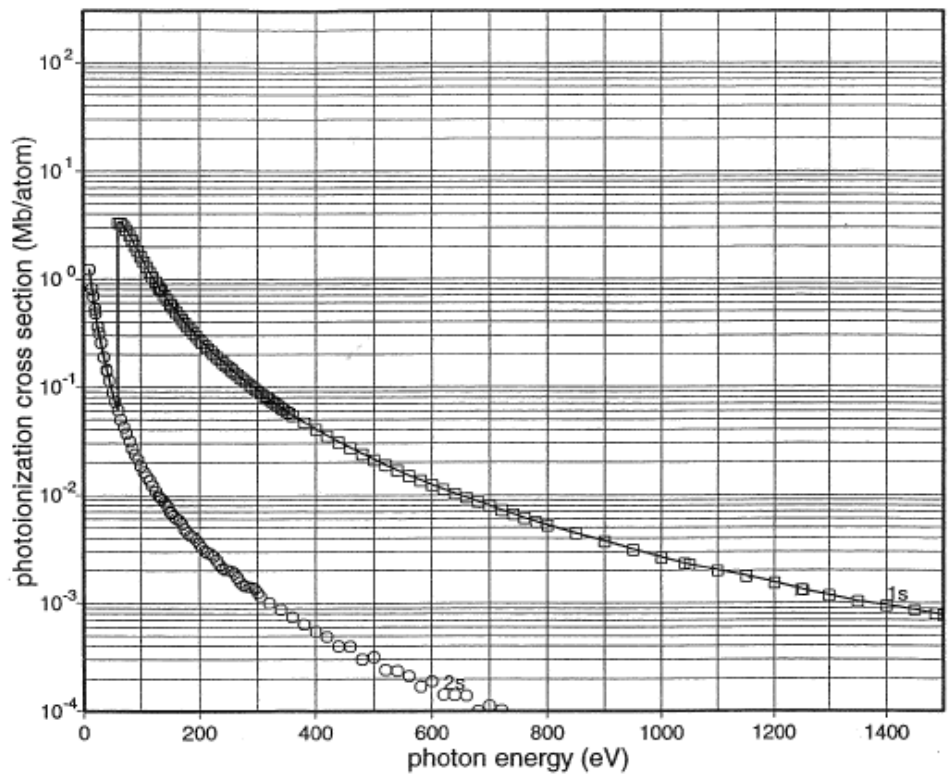

Li ^{3}

Lithium

[He]$2s^1$

6.941 amu

4.65×10^{22} /cm^3

The photoionization cross section will be enhanced dramatically by using synchrotron radiation.

	λ(Å)	1216	742	585	463	304	155	93.7	81.9	62.0	41.3	20.7	15.5	11.9	9.89	8.34
	hν(eV)	10.2	16.7	21.2	26.8	40.8	80.0	132.3	151.4	200.0	300.0	600.0	800.0	1041.0	1253.6	1486.6
(nℓ)	(BE)															
1s	59.8						2.552	0.8093	0.5707	0.2746	0.09118	0.01233	.005205	.002321	.001313	.000791
2s	5.5	1.235	0.6906	0.4805	0.3151	0.1387	0.03129	.009487	.006802	.003547	.001257	.000189	.608E-4	.289E-4	.169E-4	.103E-4
total		1.235	0.6906	0.4805	0.3151	0.1387	2.583	0.8188	0.5775	0.2781	0.09244	0.01252	.005266	.002350	.001330	.000801

0.5707 *0.001313* *0.000791*

$\sim 8 \times 10^2$

4. To Avoid the Auger electrons of Co overlap with Fe 2p peak

Cobalt **Co**
Atomic Number **27**

Handbook of X-ray Photoelectron Spectroscopy

Al Kα =1486.3 eV

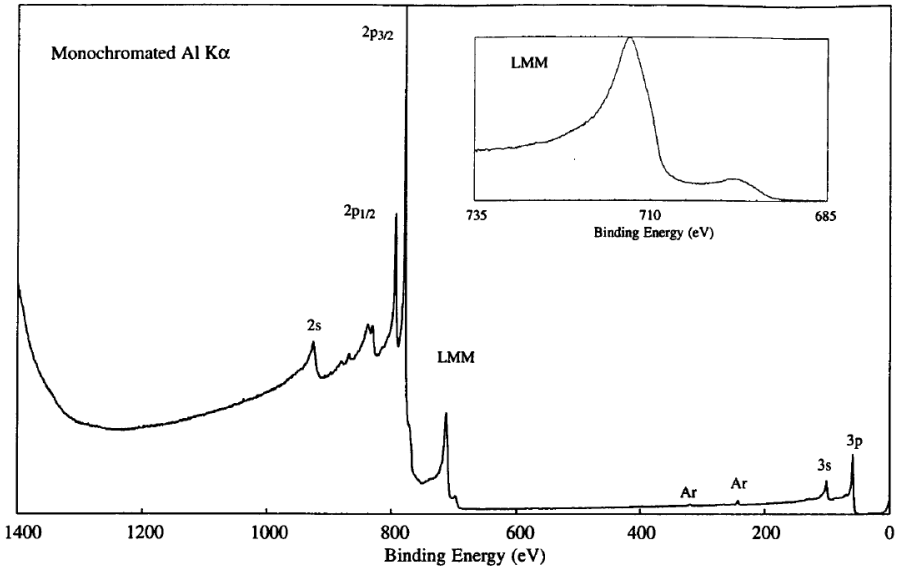

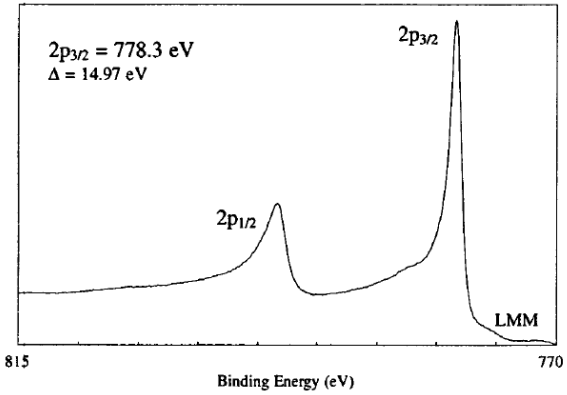

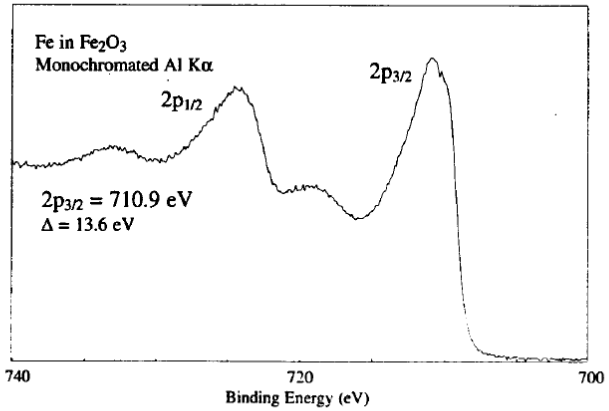

Adjust photon energy to avoid the Auger electron signal

Sample: In_2O_3

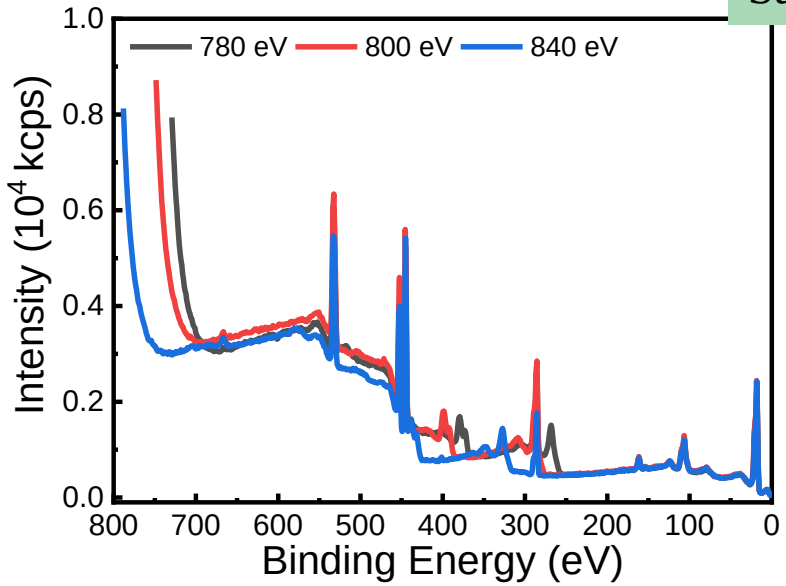

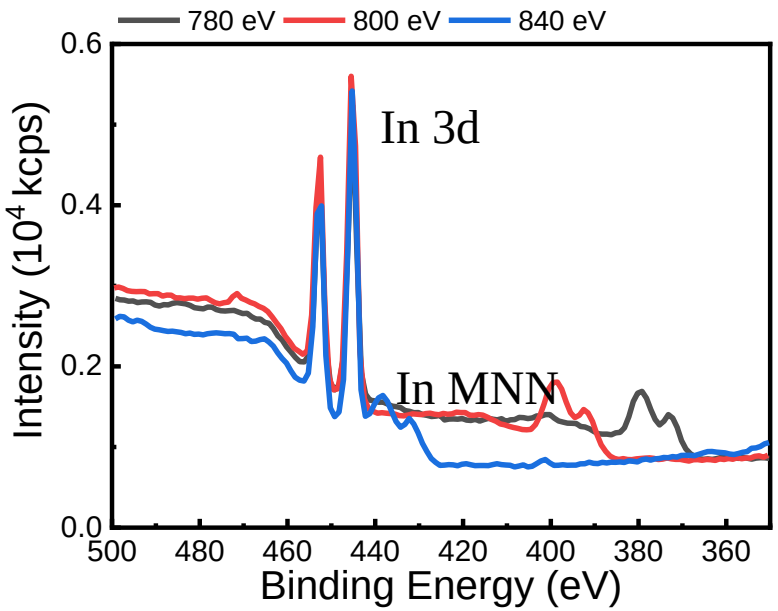

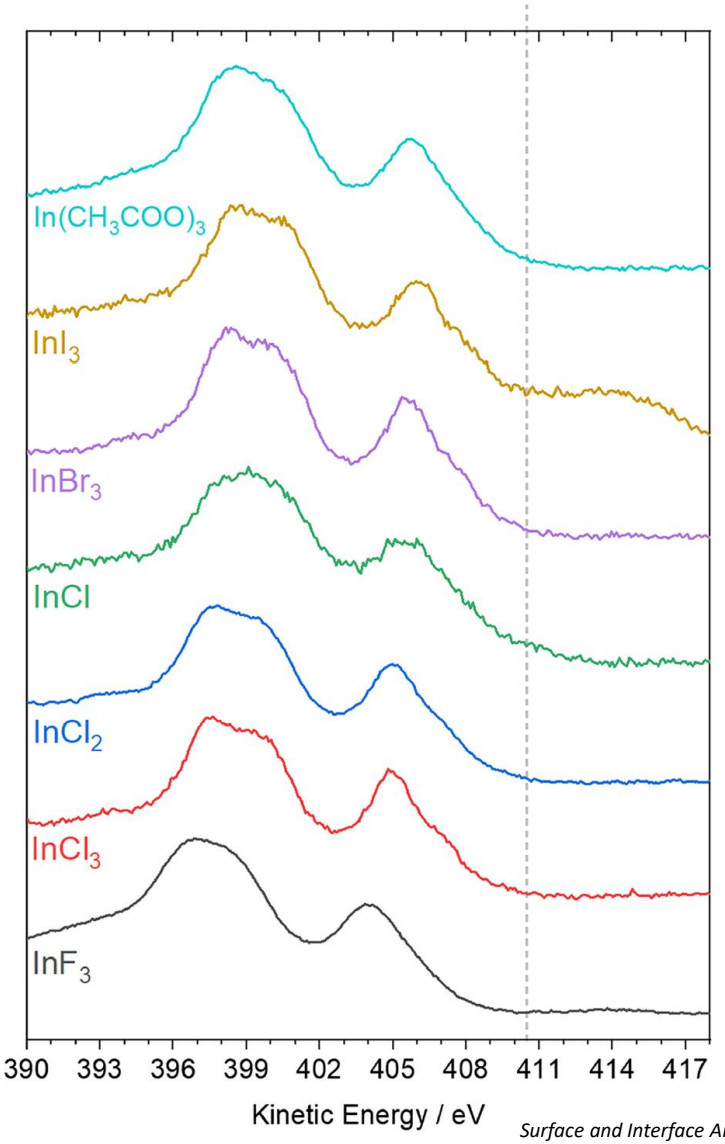

Surface and Interface Analysis, 2024

Energies and widths of commonly used soft x-ray sources

Table 2.1 Energies and widths of some characteristic soft X-ray lines

Line	Energy, eV	Width, eV
Y $M\zeta$	132.3	0.47
Zr $M\zeta$	151.4	0.77
Nb $M\zeta$	171.4	1.21
Mo $M\zeta$	192.3	1.53
Ti $L\alpha$	395.3	3.0
Cr $L\alpha$	572.8	3.0
Ni $L\alpha$	851.5	2.5
Cu $L\alpha$	929.7	3.8
Mg $K\alpha$	1253.6	0.7
Al $K\alpha$	1486.6	0.85
Si $K\alpha$	1739.5	1.0
Y $L\alpha$	1922.6	1.5
Zr $L\alpha$	2042.4	1.7
Ti $K\alpha$	4510.0	2.0
Cr $K\alpha$	5417.0	2.1
Cu $K\alpha$	8048.0	2.6

Resolving power for TLS 24A

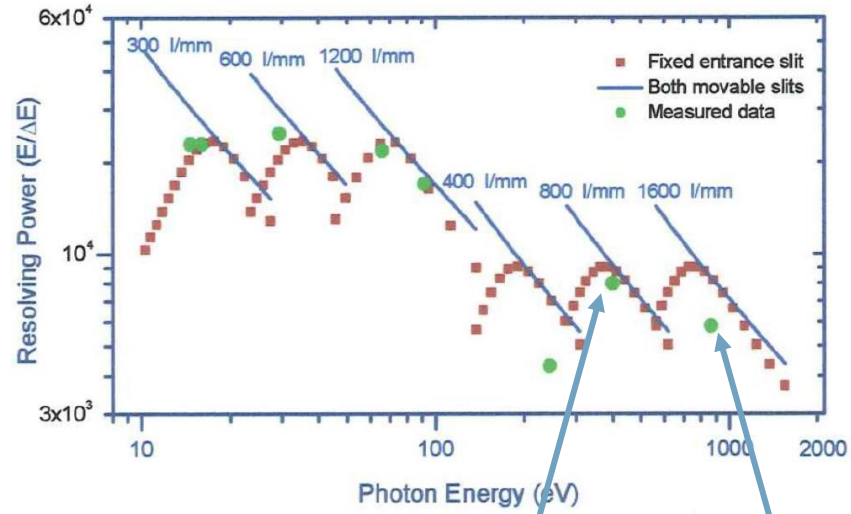

S1=S2= 10 μm,
hν :~400 eV, E/ΔE=8000
→ ΔE=0.05 eV

S1=S2= 10 μm,
hν :~850 eV, E/ΔE=6000
→ ΔE=0.15 eV

Al $K_{\alpha 1}$ with quartz monochromator: ~0.3 eV

$$\mathrm{FWHM_{tot}} = (\mathrm{FWHM}_n^2 + \mathrm{FWHM}_x^2 + \mathrm{FWHM}_a^2 + \mathrm{FWHM}_{ch}^2 + \cdots)^{1/2} \quad (3.12)$$

where FWHM is the full-width at half-maximum of the observed peak (tot), core hole lifetime (n), X-ray source (x), analyzer (a), and charging contribution (ch).

XPS End stations at TLS

Beamline	Source	Energy (eV)	Major Technology
05B2	undulator	60- 1400	PEEM (TPS 27A2)
08B1	Bending	15- 200	ARPES
09A1, A2	undulator	60- 1500	SPEM, (XPS, XAS)
20A	Bending	10- 1250	XAS, XPS
21B	undulator	5- 100	ARPES
24A	Bending	10- 1600	XPS, XAS

Beamline 24 A at TLS

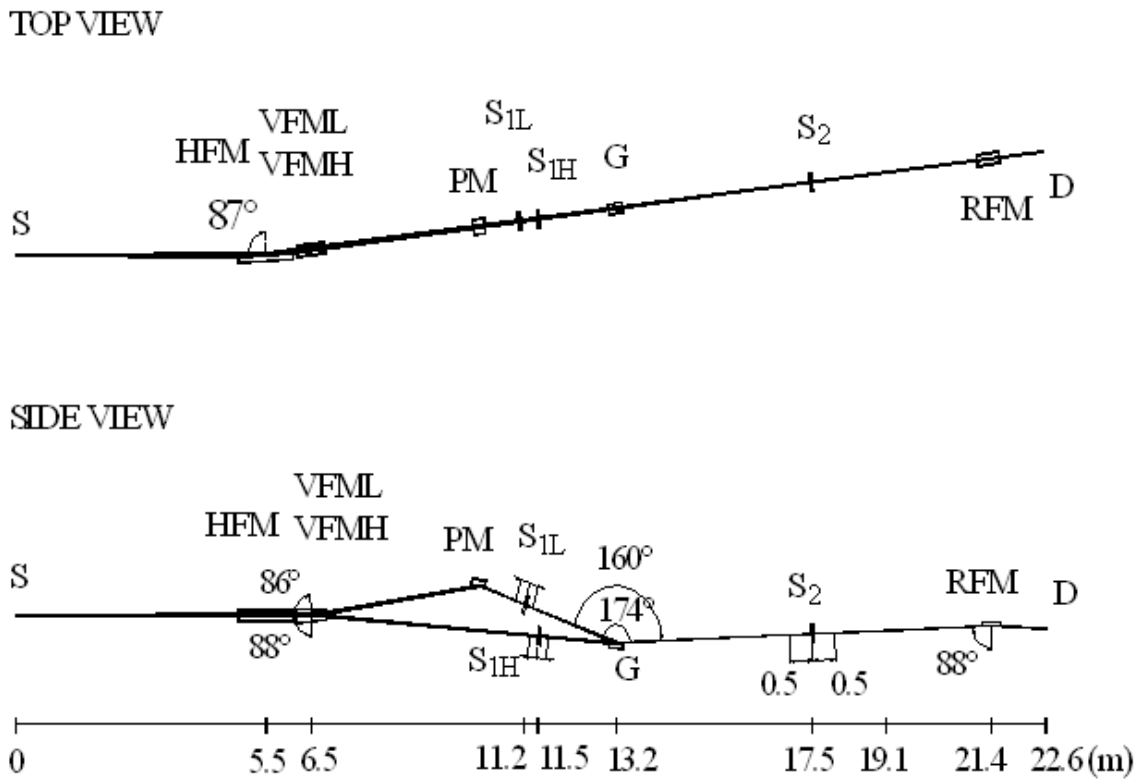

Source	Energy (eV)	Focusing Mirror	Focused Beam Size FWHM H × V (mm)	Resolving Power E/dE
BM	15 ~ 175 120 ~ 1600	Toroidal RFM	0.7 × 0.3	20000 8000

Six spherical gratings are used to cover photon energies from 15 to 1600 eV.

	Grating Ruling Density (l/mm)	Usable Photon Energy Range (eV)
Low Energy Branch	300	15-40
	600	16-63
	1200	32-175
High Energy Branch	400	120-380
	800	240-840
	1600	500-1600

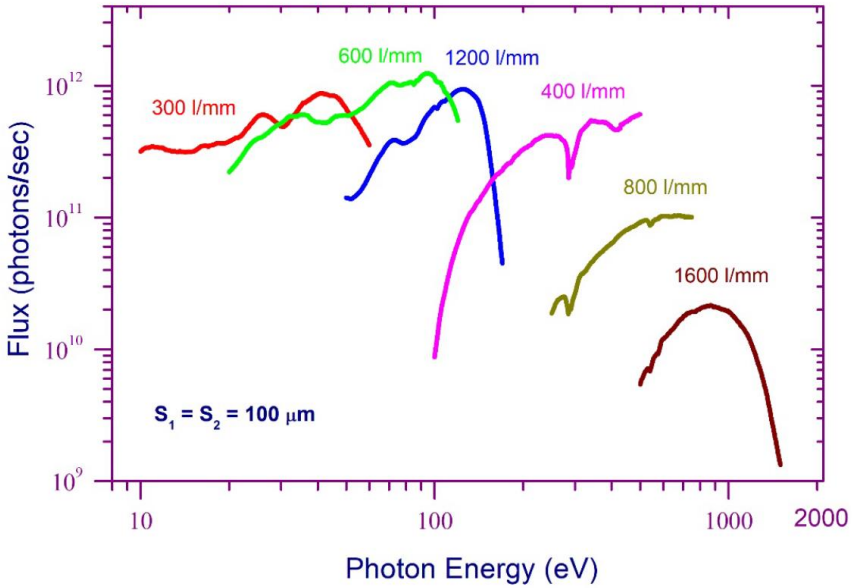

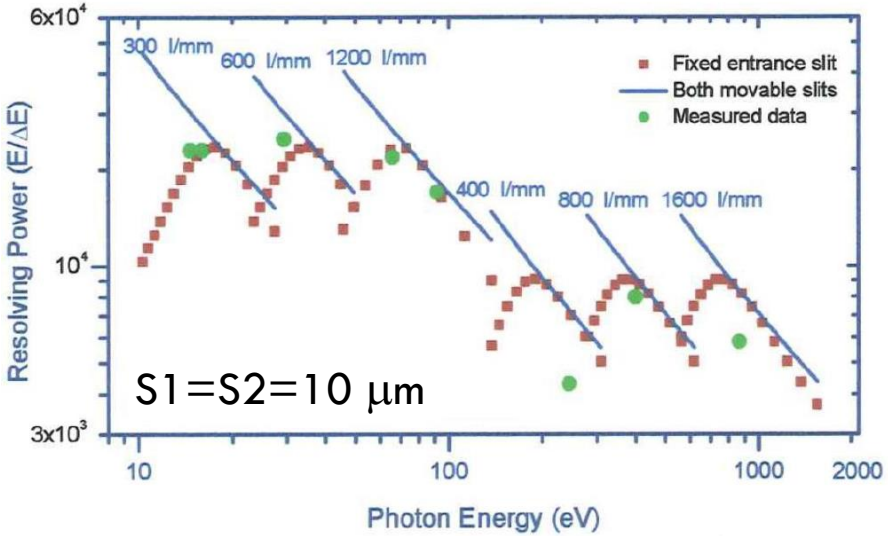

End stations at BL24A of TLS

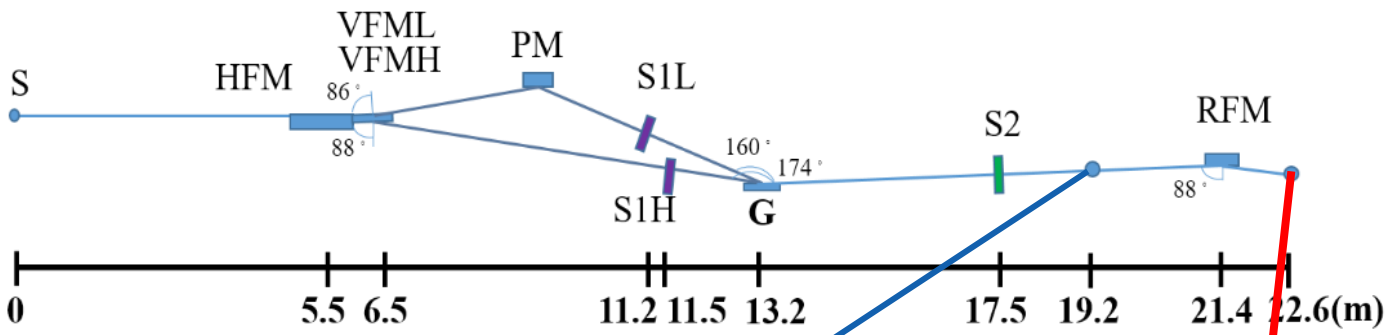

L: Low energy branch, H: High energy branch, S: Slit, G: Grating

Conventional XPS endstation (SPECS PHOIBOS 150 analyzer)

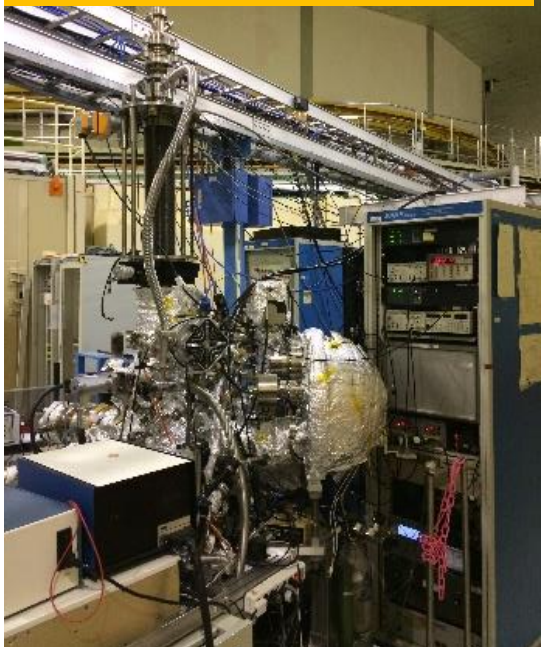

APXPS endstation (SPECS PHOIBOS 150 NAP analyzer)

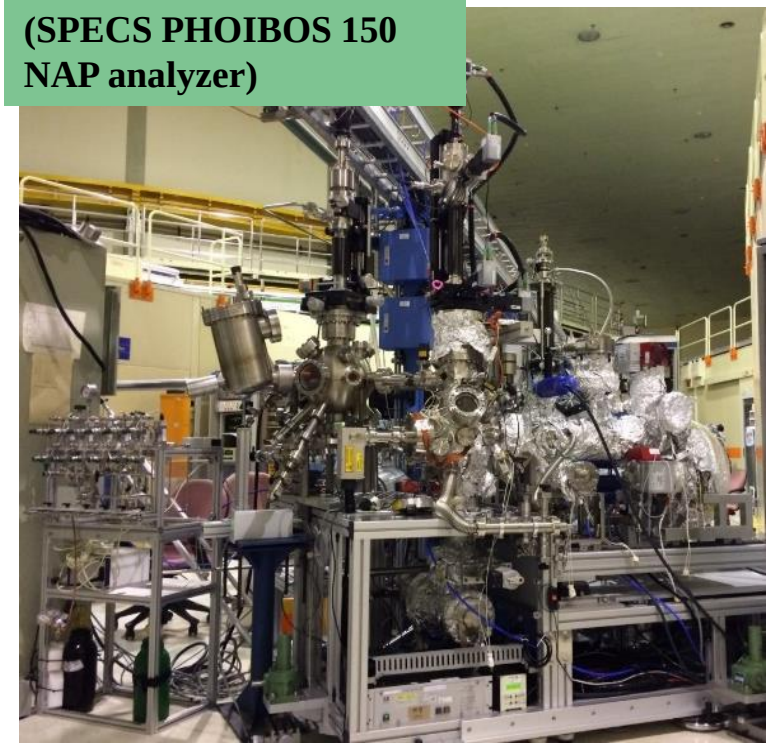

Beamline 24 A

Photoemission Spectroscopy :

Conventional X-Ray Photoemission Spectroscopy (XPS)

Chemical state, Elements compositions, ….

(Near) Ambient pressure XPS

In-situ and in operando XPS measurements

Ultraviolet Photoemission Spectroscopy (UPS)

Energy (eV): He lamp, He I : 21.21 eV, He II: 40.2 eV

SR (Lower Energy branch): 15 – 175 eV

Valence band information:

HOMO, Band structure, Work function…..

X-Ray Absorption Spectroscopy (Electron Yield):

Near Edge X-ray Absorption Fine Structure (NEXAFS)

Molecular Orientation, Molecular Fine Structure,….

TEY ~ 15 nm
PEY ~ 5 nm
AEY ~ 3 nm

Applications of Synchrotron _based X-ray Photoelectron Spectroscopy (XPS) at the conventional XPS endstation of BL 24A

Dual-Axis Alignment of Bulk Artificial Water Channels by Directional Water-Induced Self-Assembly

Yuan Chen, Hsi-Yen Chang, Mu-Tzu Lee, Zong-Ren Yang, Chia-Hsin Wang, Kuan-Yi Wu,* Wei-Tsung Chuang,* and Chien-Lung Wang*

Cite This: *J. Am. Chem. Soc.* 2022, 144, 7768–7777

Read Online

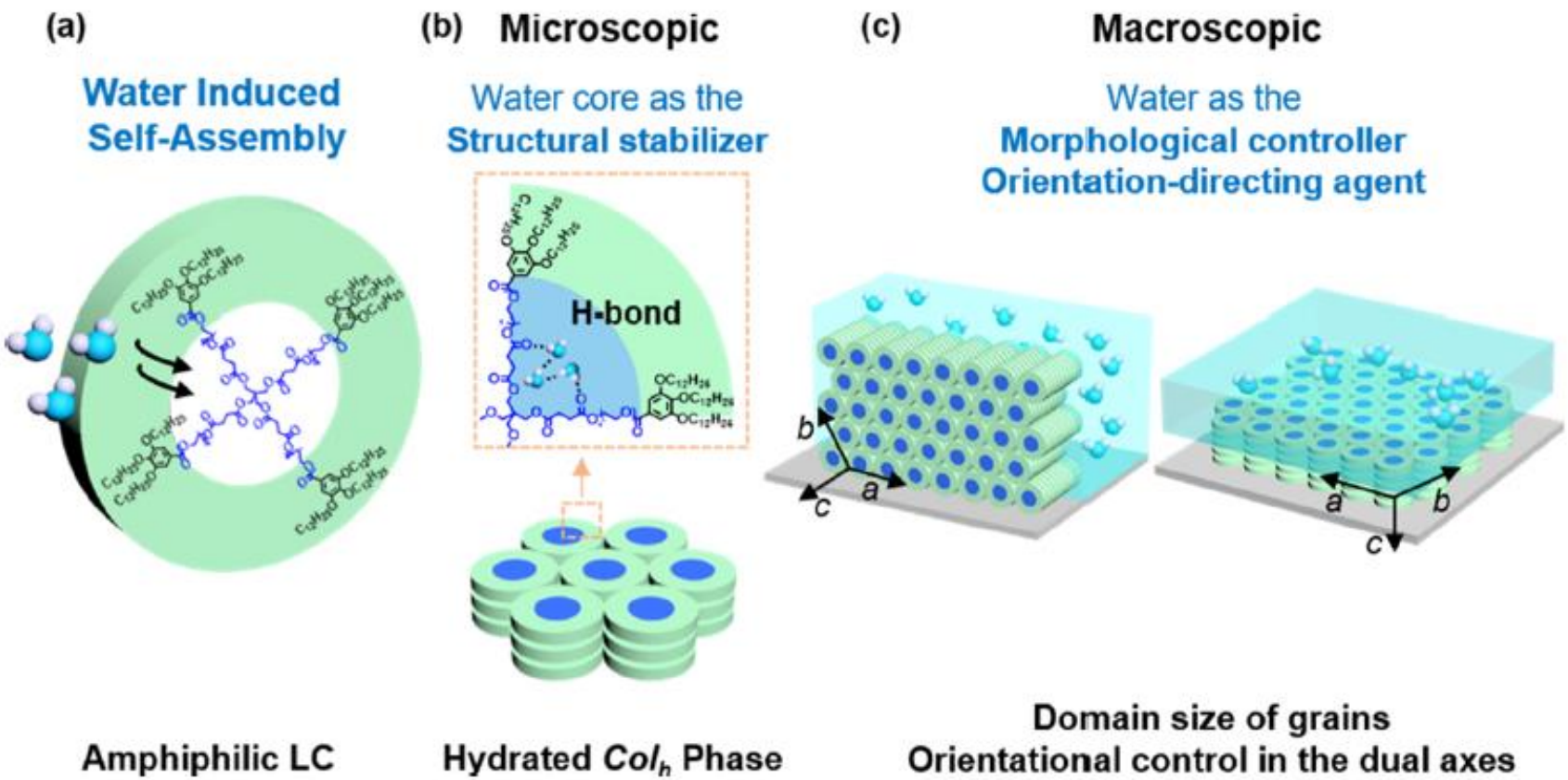

Water as an excellent structural stabilizer and orientation-directing agent of an amphiphilic discotic molecule (AD) in the water-induced self-assembly (WISA) process.

Depth profile of XPS measurements applied with different X-ray excitation photon energies

C1s

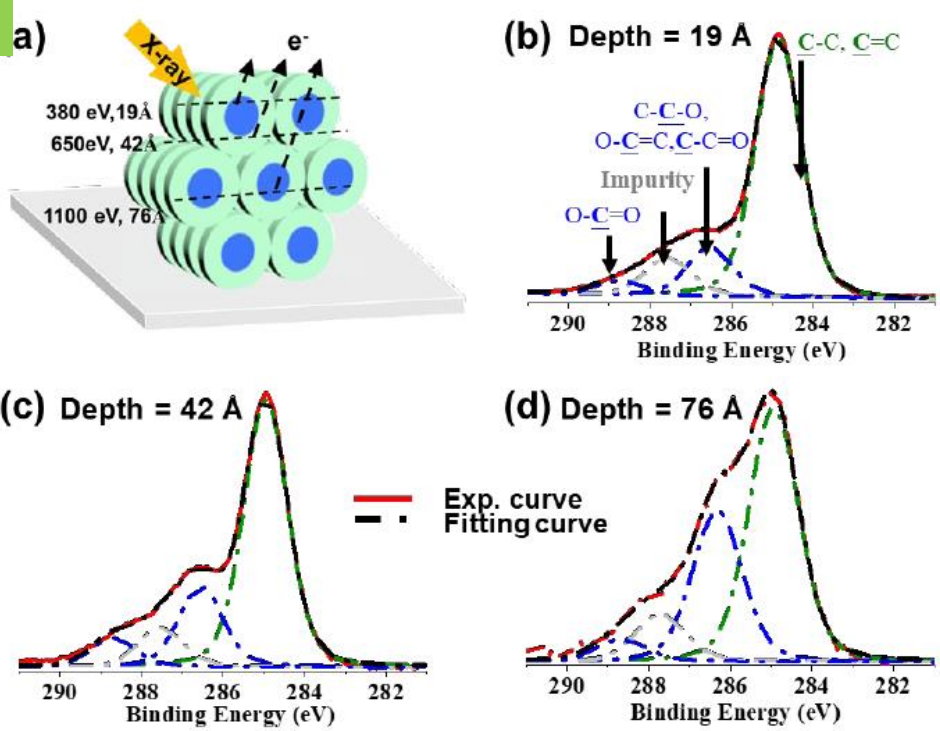

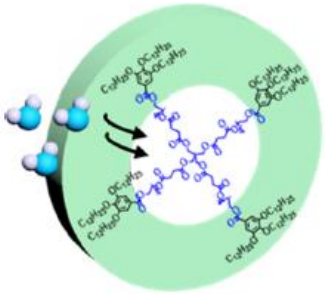

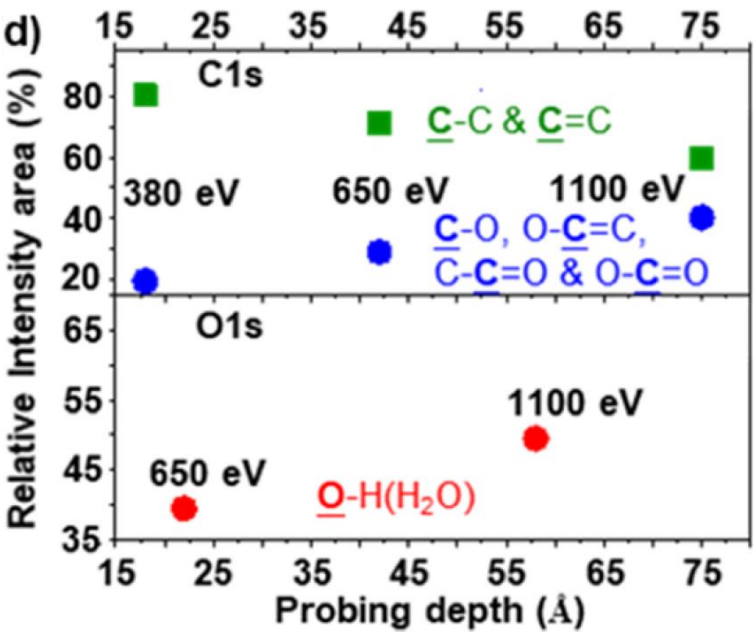

O1s

hν= 650 eV

hν= 1100 eV

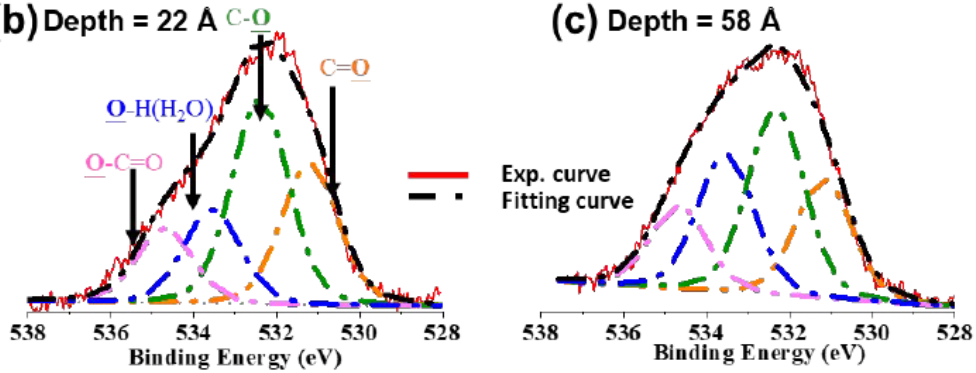

Relative intensity area (A_{rel}) of the hydrophobic (green color) and hydrophilic segments (blue color) of the AD in C 1s spectra and H_2O (red color) in O 1s spectra as functions of the probing depth.

Contents lists available at ScienceDirect

Chemical Engineering Journal

journal homepage: www.elsevier.com/locate/cej

WO_x nanowire supported ultra-fine Ir-IrO_x nanocatalyst with compelling OER activity and durability

Lu-Yu Chueh [a], Chun-Han Kuo [b], Ren-Hao Yang [a], Ding-Huei Tsai [a], Meng-Hsuan Tsai [c], Chueh-Cheng Yang [c], Han-Yi Chen [b], Chia-Hsin Wang [c], Yung-Tin Pan [a,*]

[a] Department of Chemical Engineering, National Tsing Hua University, 101 Section 2, Kuang-Fu Rd., Hsinchu City 300044, Taiwan
[b] Department of Materials Science and Engineering, National Tsing Hua University, 101 Section 2, Kuang-Fu Rd., Hsinchu City 300044, Taiwan
[c] National Synchrotron Radiation Research Center, Hsinchu City 300902, Taiwan

Chemical Engineering Journal **2023**, *464*, 142613.

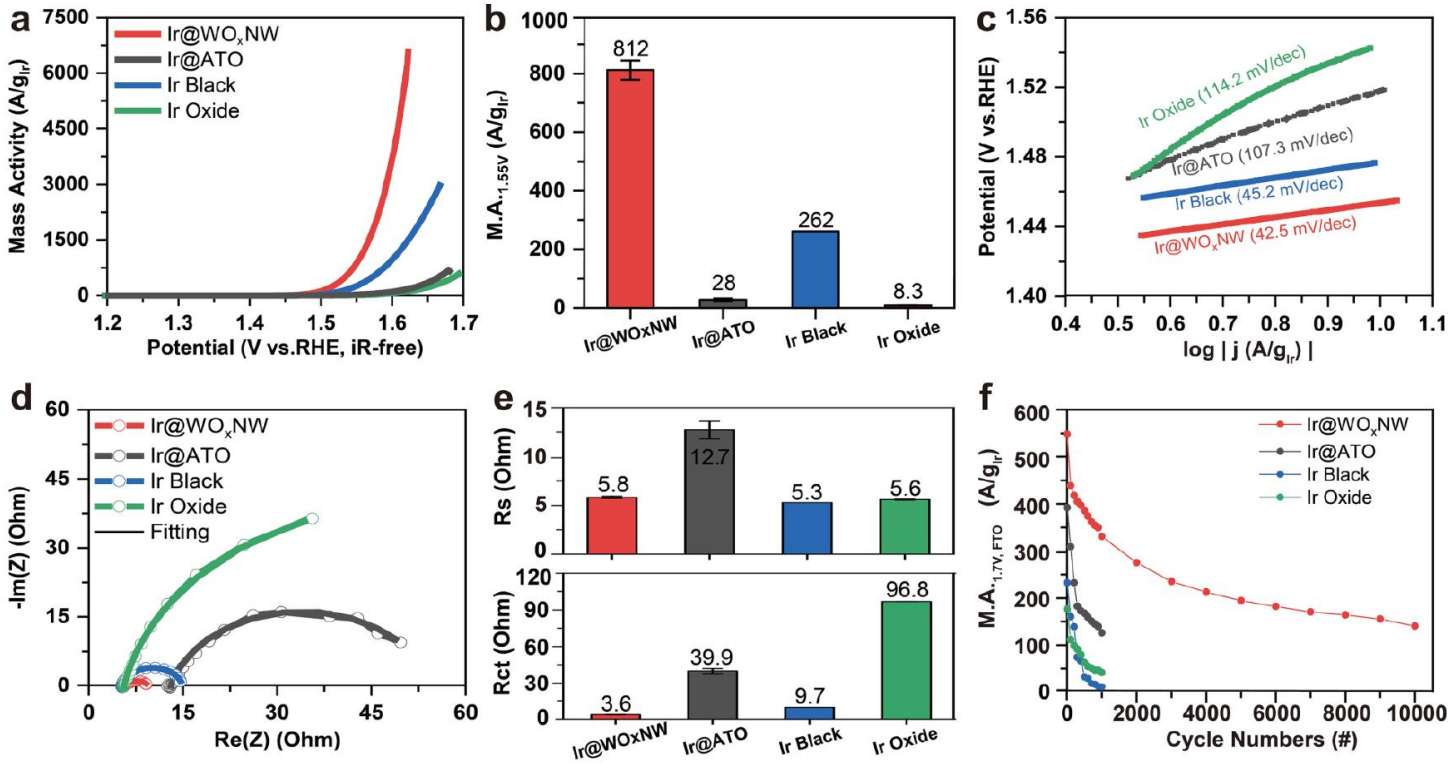

Depth profile of XPS measurements applied with different X-ray excitation photon energies

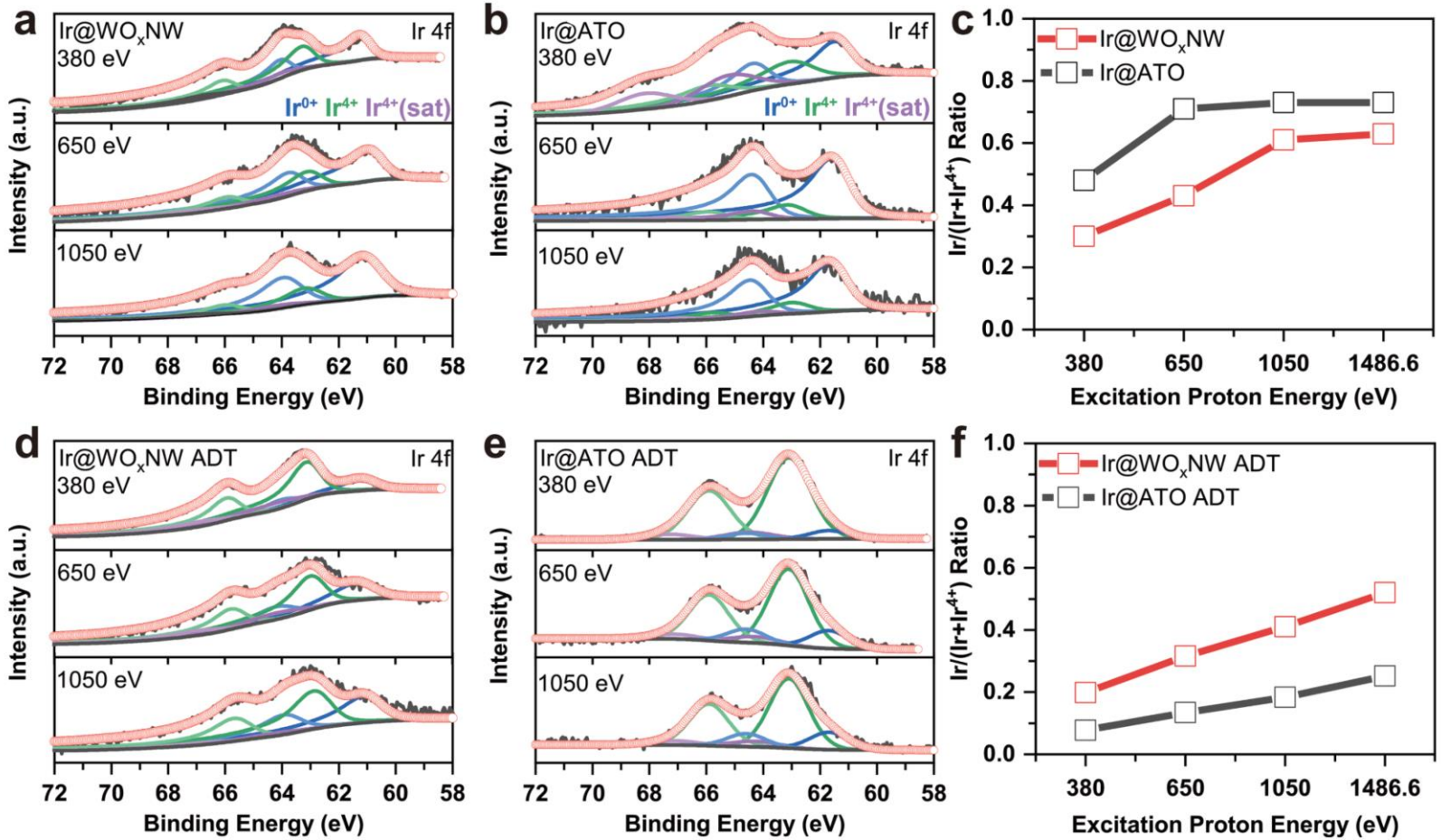

Fig. 5. Valence state depth profiling of Ir@WO_xNW and Ir@ATO by energy resolved XPS. Non-destructive depth profile Ir 4f spectra and summary of Ir^0 fraction as a function of incident X-ray energy for as-prepared Ir@WO_xNW and Ir@ATO (a-c) and after ADT (d-f).

Strong catalyst-support interaction stabilizes the OER activity

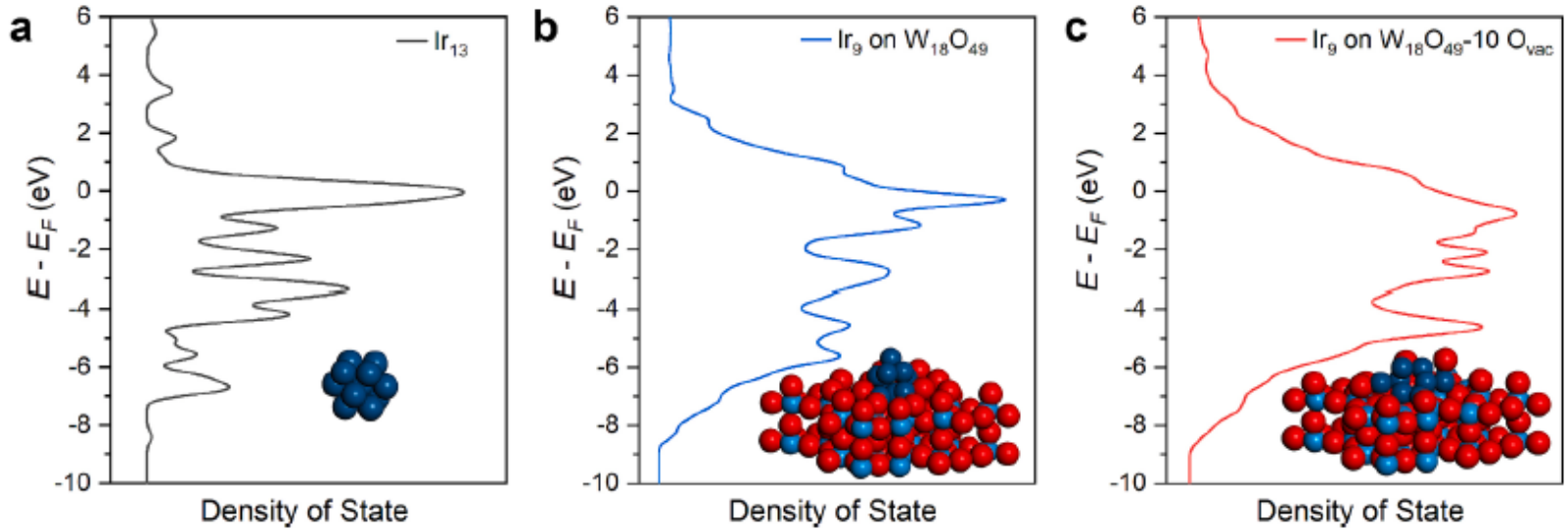

Fig. 7. Calculated DOS of *d*-band of (a) Ir_{13}, (b) Ir_9 supported on $W_{18}O_{49}$, and (c) Ir_9 supported on $W_{18}O_{49}$ with 10 surface oxygen vacancies.

The binding strength of oxygen to the surface atoms:

Ir_{13}> Ir_9 on $W_{18}O_{49}$ > Ir_9 on $W_{18}O_{49}$ -10 O_{vac}

CHEMISTRY OF MATERIALS
Article
Cite This: *Chem. Mater.* 2017, 29, 8992-9000
pubs.acs.org/cm

Selective Hydrogen Etching Leads to 2D Bi(111) Bilayers on Bi_2Se_3: Large Rashba Splitting in Topological Insulator Heterostructure

Shu Hsuan Su,[†,▲] Pei Yu Chuang,[†,▲] Sheng Wen Chen,[†] Hsin Yu Chen,[†] Yi Tung,[†] Wei-Chuan Chen,[∥] Chia-Hsin Wang,[∥] Yaw-Wen Yang,[∥] Jung Chun Andrew Huang,[*,†,‡,§] Tay-Rong Chang,[*,†] Hsin Lin,[#,∇] Horng-Tay Jeng,[⊥,◆] Cheng-Maw Cheng,[*,∥,¶] Ku-Ding Tsuei,[∥] Hai Lin Su,[○] and Yu Cheng Wu[○]

Photon Energy: 200 eV

Bi_2Se_3 thin film 80 nm.

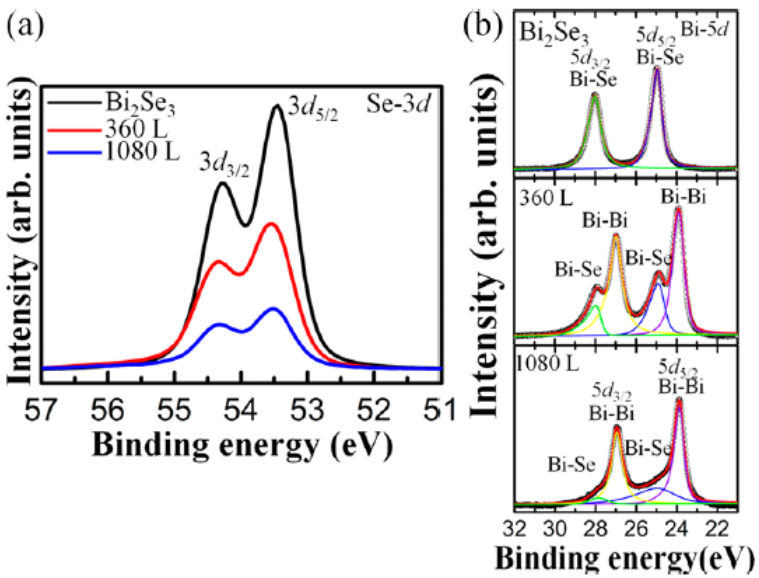

Figure 3. XPS of (a) Se 3d peaks and (b) Bi 5d peaks before and after dosing hydrogen at 360 and 1080 L, respectively.

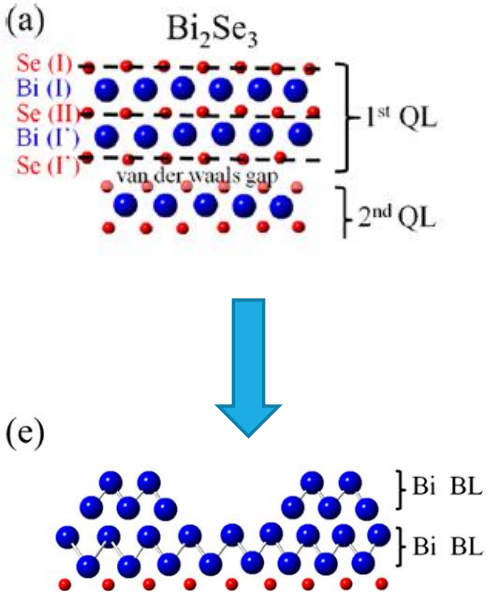

Published by NCKU

ACS APPLIED MATERIALS & INTERFACES

Research Article

Cite This: ACS Appl. Mater. Interfaces 2019, 11, 31962−31971

www.acsami.org

Effects of Concentrated Salt and Resting Protocol on Solid Electrolyte Interface Formation for Improved Cycle Stability of Anode-Free Lithium Metal Batteries

Tamene Tadesse Beyene,[†] Bikila Alemu Jote,[†] Zewdu Tadesse Wondimkun,[†] Bizualem Wakuma Olbassa,[†] Chen-Jui Huang,[†] Balamurugan Thirumalraj,[†] Chia-Hsin Wang,[#] Wei-Nien Su,[*,‡] Hongjie Dai,[*,§] and Bing-Joe Hwang[*,†,#,φ]

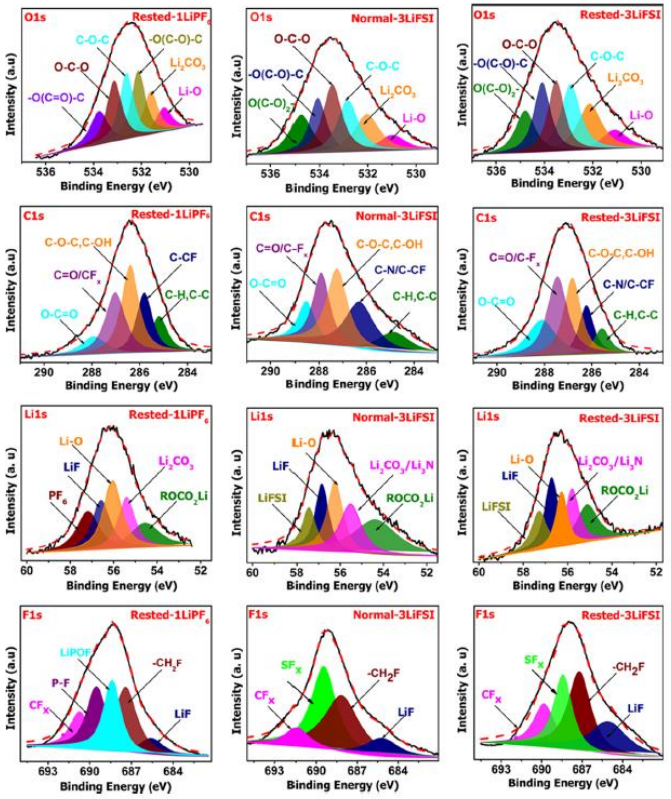

Li spectra

Published by NTUST

(Near) Ambient Pressure X-ray Photoelectron Spectroscopy (APXPS)

- **Introduction of Ambient Pressure XPS (APXPS)**
- **Scientific Opportunities**
- **APXPS End Station at NSRRC**

UHV-XPS v.s. (Near) Ambient Pressure XPS (APXPS)

UHV- XPS

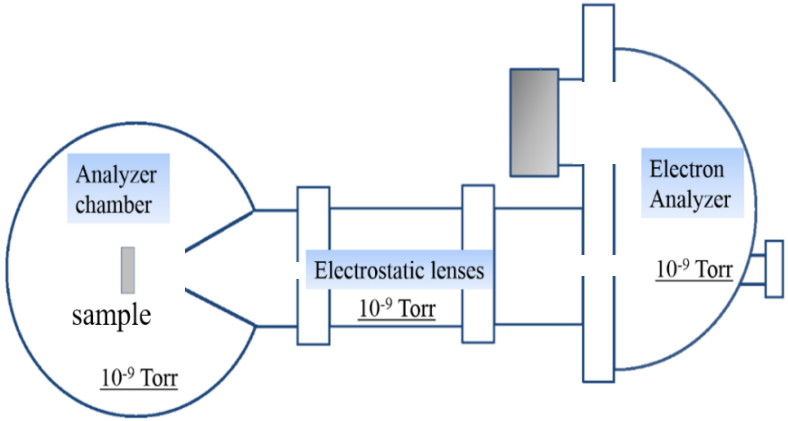

Conventional-XPS needs to be performed in an environment better than high-vacuum to eliminate electron-gaseous molecule scattering problem, and be used to study the chemical state and elemental composition of surface layers in solid samples.

APXPS

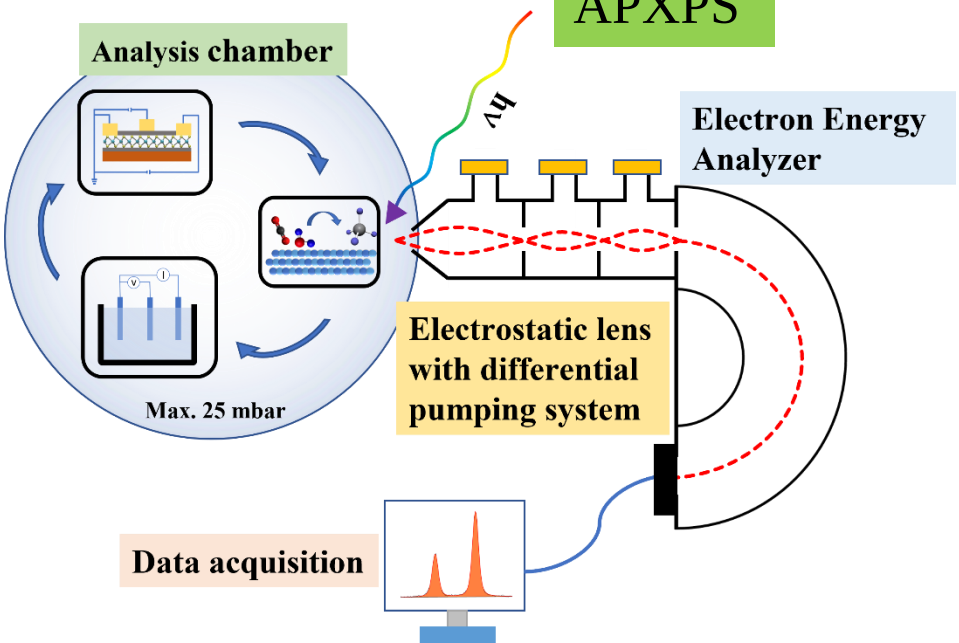

APXPS allows the photoemission spectroscopy to be carried out at an elevated pressure up to ~25 mbar, enabling an in-situ and in-operando investigation of gas-solid, liquid-solid, and liquid-gas heterogeneous reactions.

Introduction of APXPS (II)

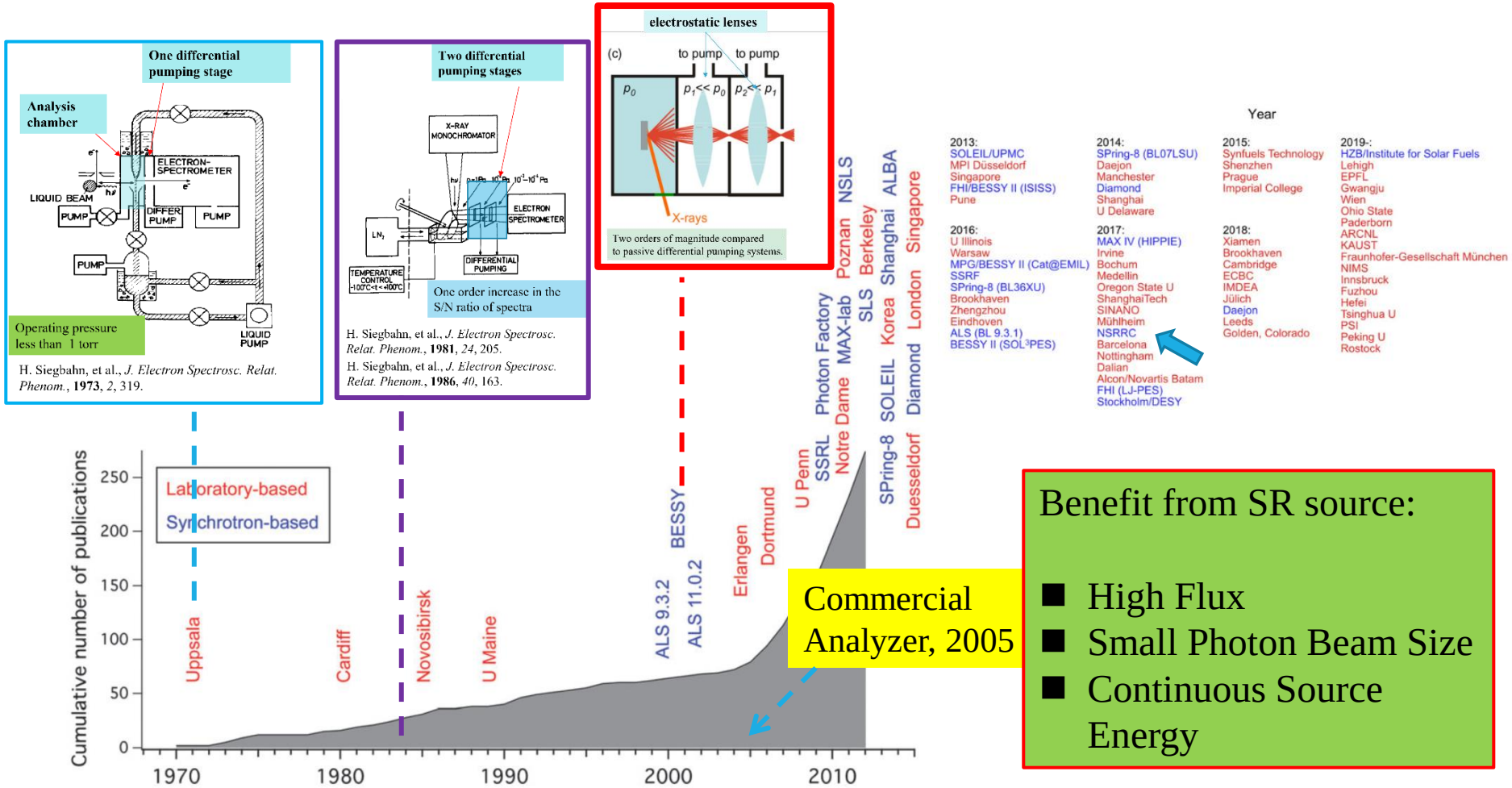

Fig. 1 Ambient pressure XPS timeline, showing both the cumulative number of publications and the installation of new instruments. Red labels denote laboratory-based, blue labels synchrotron-based instruments. The dates for the installation of the instruments are approximate and to the best of our knowledge.

D. E. Starr, et al., *Chem. Soc. Rev.* **2013**, *42*, 5833.

J. Phys.: Condens. Matter., **2020**, *32*, 413003.

Early design of APXPS instrument

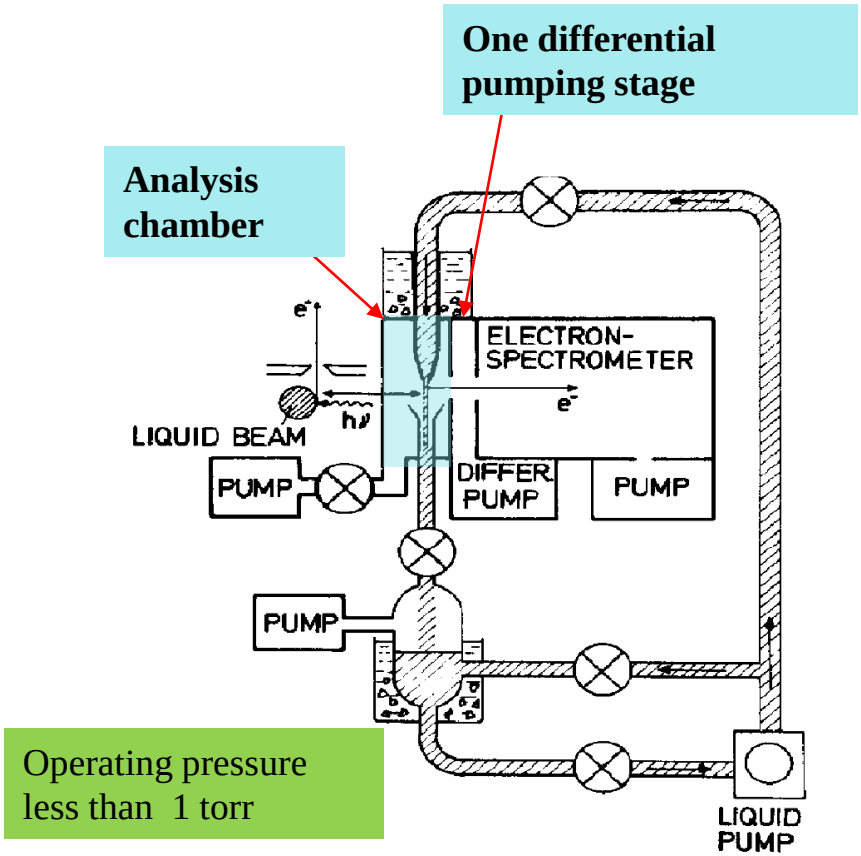

H. Siegbahn, et al., *J. Electron Spectrosc. Relat. Phenom.*, **1973**, *2*, 319.

Differential pumping concept

Differentially pumped vacuum systems use a small aperture or tube to connect two parts of a vacuum system at very different pressures.

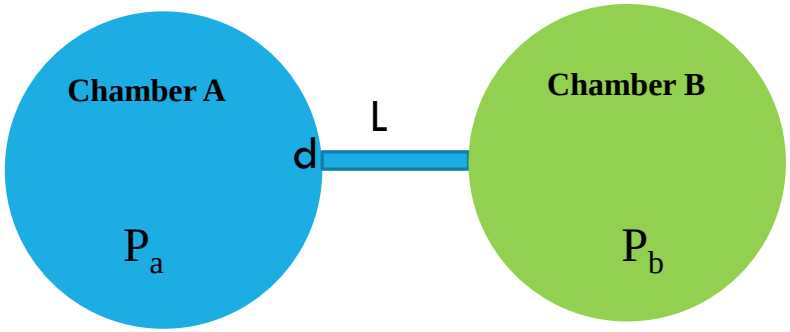

$Q=C(P_b-P_a)$, $Q=SP_b$, $P_b= C*P_a/C+S)$

If P_a= 1mbar, viscous flow, (aperture)

$C=135*d^3*(P_a+P_b)/2*L$(thickness of aperture)

Q: Gas throughput, C: conductance,

S: Pumping speed

The Pressure limit in APXPS

The attenuation of the photoelectron signal in a gas environment

$$I_p/I_0(KE,p) = \exp(-z\sigma(KE)p/kT),$$

I_0 : The signal at pressure p_0 (high vacuum).

I_p: The attenuation of the signal at pressure p

z: The distance that the electrons travel in a gas at pressure p.

σ: The electron scattering cross section (depends on the chemical composition of the gas phase)

KE: Photoelectron kinetic energy

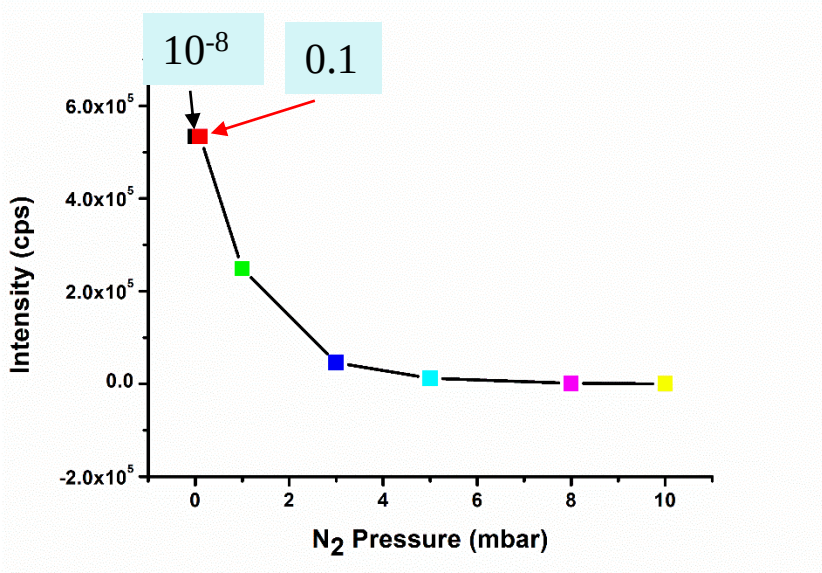

Attenuation of XPS Au 4f signal from a gold substrate by ambient N_2 gas at different pressure by using photon energy of 620 eV.

The Pressure limit in APXPS

- Photoelectron kinetic energy
- Scattering cross section of gas species
- The distance between sample to aperture (nozzle)

Photoelectron kinetic energy effect

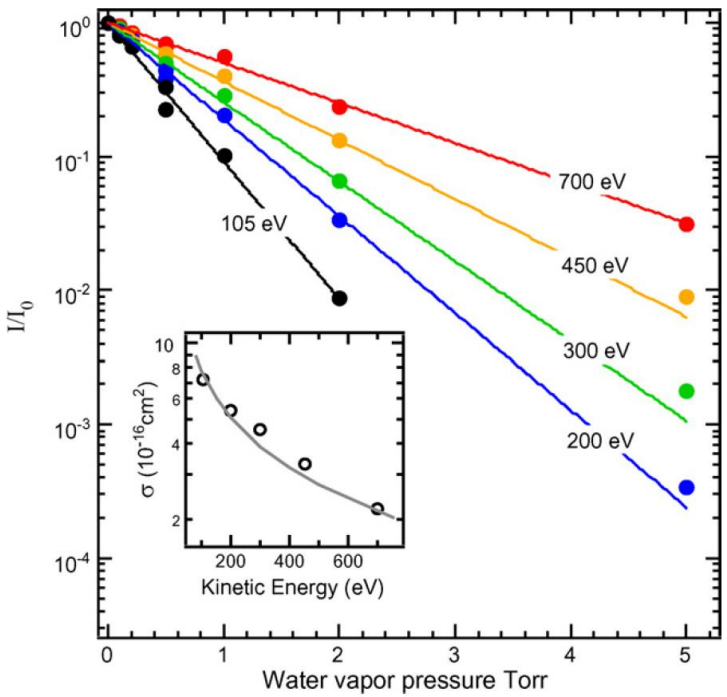

Hendrik Bluhm, *J. Electron Spectrosc. Relat. Phenom.*, **2010**, *177*, 71.

Scattering cross section of gas species

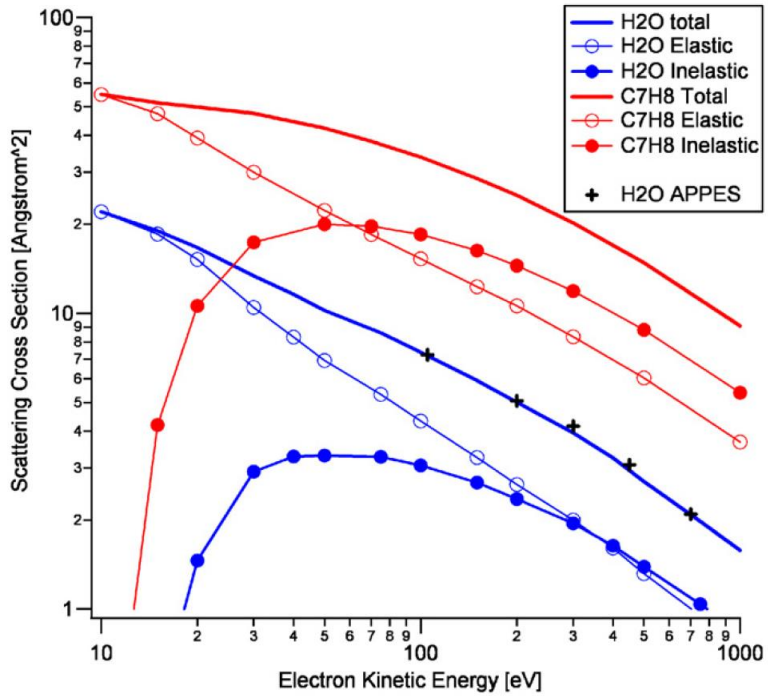

D. Frank Ogletree, et al., *Nucl. Instrum. Methods A*, **2009**, *601*, 151.

The distance between sample to aperture (nozzle)

1. Inelastic mean free path of electrons

Exp:

The inelastic mean free path of electrons with 100 eV kinetic energy in 1 mbar water vapor is about 1 mm, much shorter than the typical working distance between the sample and the entrance to the electrostatic lens system of an electron analyzer, which is a few centimeters.

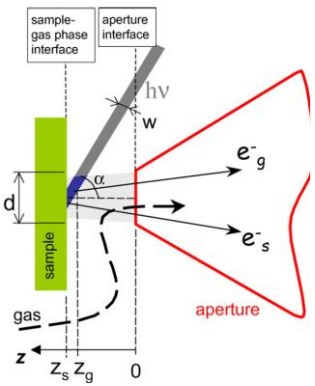

2. Pressure conditions across the sample surface

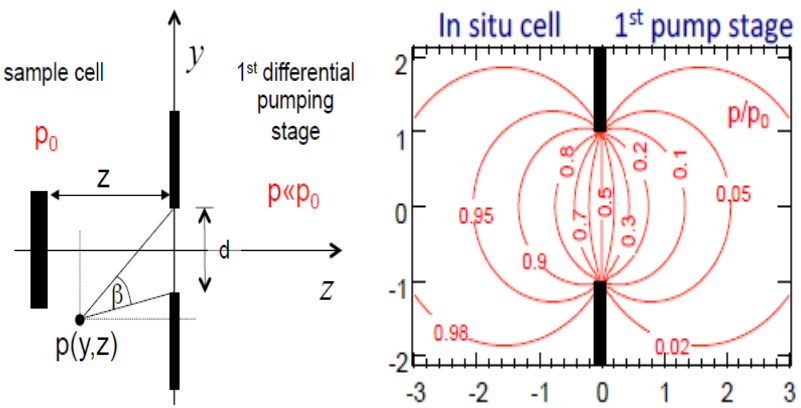

At z~2d p=0.99p_0

Since I/I_p~exp(-z), smaller beam sizes allow for smaller apertures, closer sample-aperture distances and thus higher pressures.

Hendrik Bluhm, *J. Electron Spectrosc. Relat. Phenom.*, **2010**, *177*, 71.

3. Aperture (nozzle) size

d~ P_{max}^{-1} , (Reducing the aperture size increases the working pressure)

nozzle size: 300 μm, The maximum operating pressure~ 10 mbar

(APXPS at TLS BL24A)

Photon–gas interactions

The scattering of X-ray photons by the reaction gases in APXPS experiments is generally much weaker than for electrons.

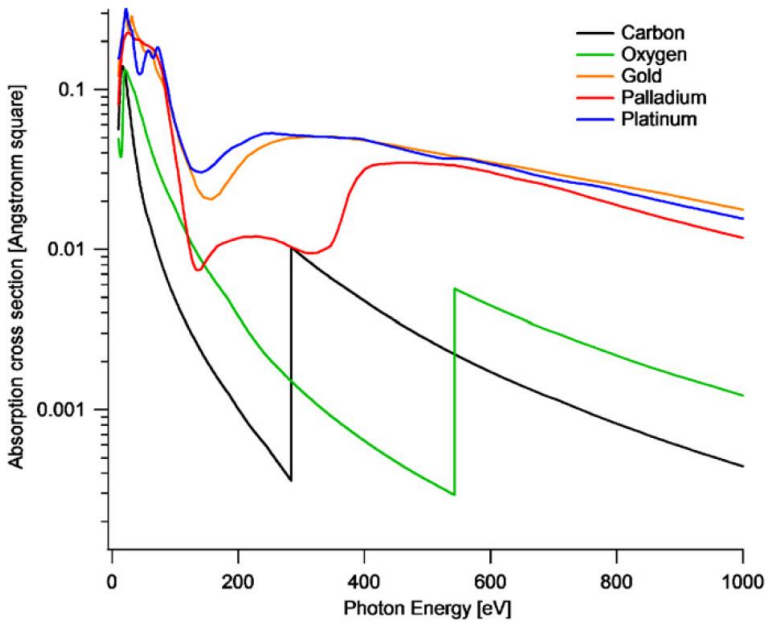

X-ray scattering cross-sections for the 1s levels of light elements like C, N, O, and H are about three orders of magnitude smaller than the electron–gas cross-sections .

Beam entrances system

Windowless system

1 (300 μm), **2** (1.5 mm), **3** (2 mm) and **4** (3mm).

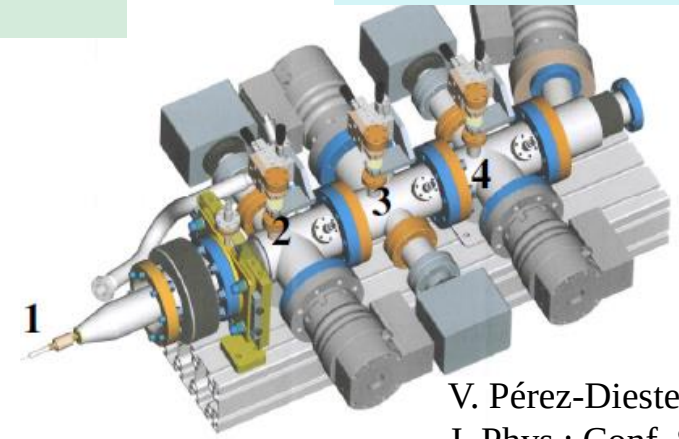

V. Pérez-Dieste, et al., J. Phys.: Conf. Series, **2013**, ***425*,** 072023.

Si_3N_4 window

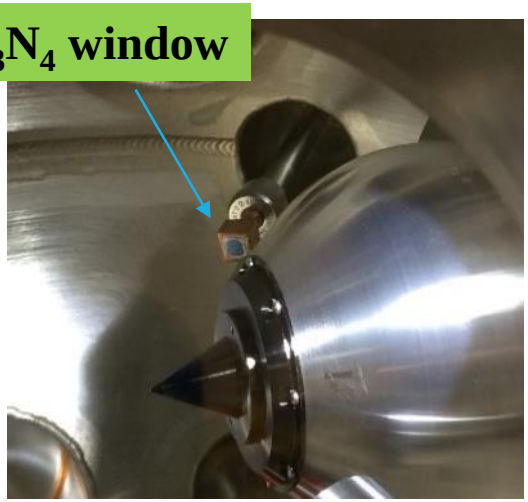

APXPS systems

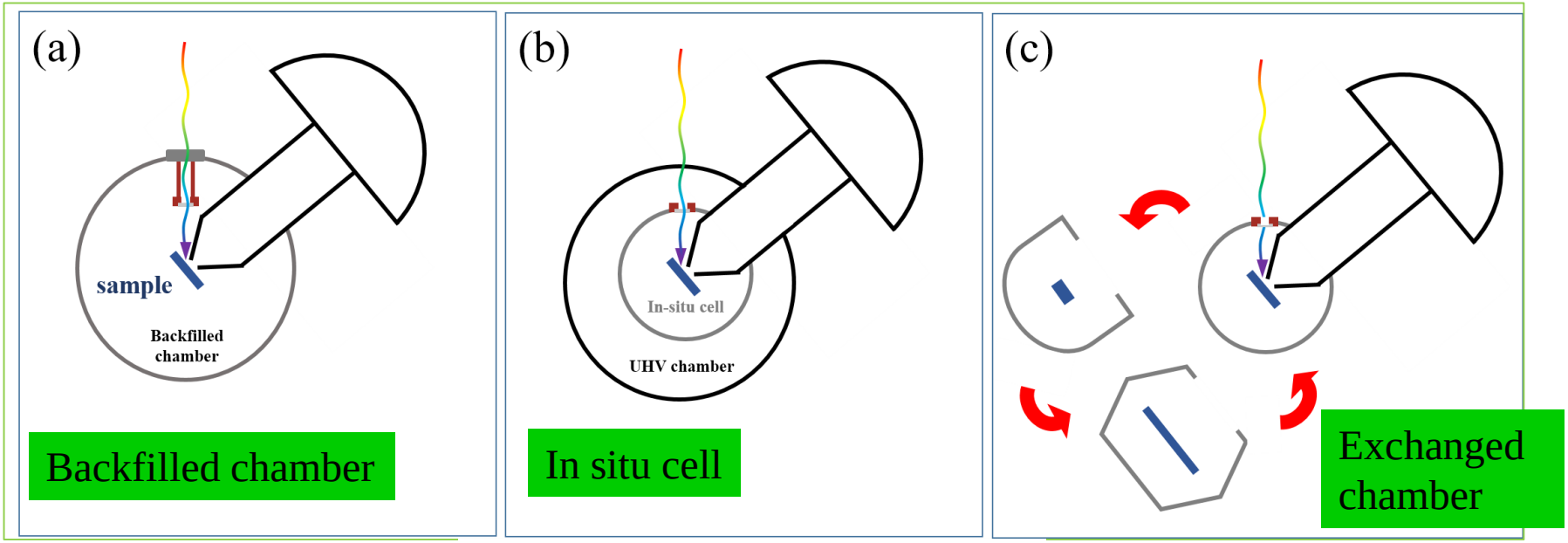

The whole chamber is exposed to gases during APXPS experiments.

(This chamber is often connected with load lock and preparation chamber)

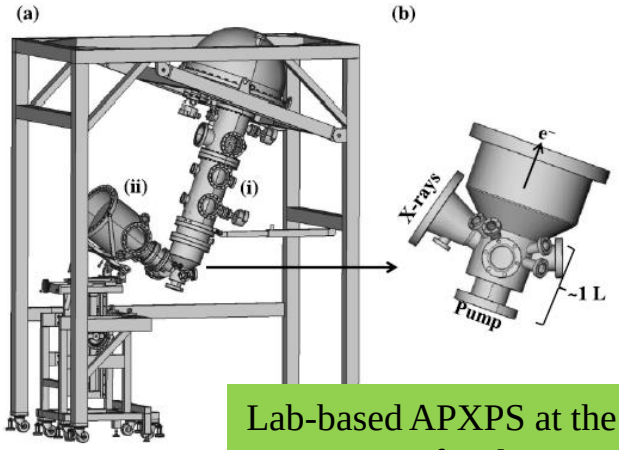

Lab-based APXPS at the University of Delaware

Scientific Opportunities

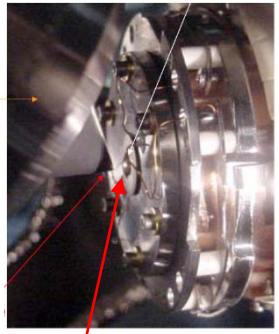

KBr sample

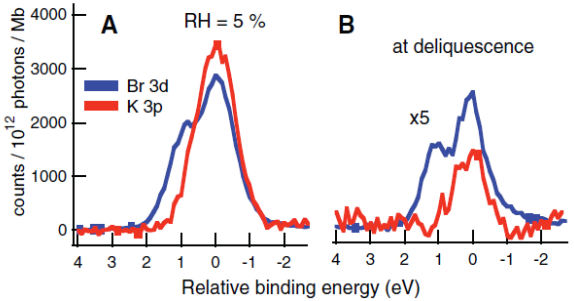

Science **2005**, *307*, 563.

In Situ Study of the Gas-Phase Electrolysis of Water on Platinum by NAP-XPS**

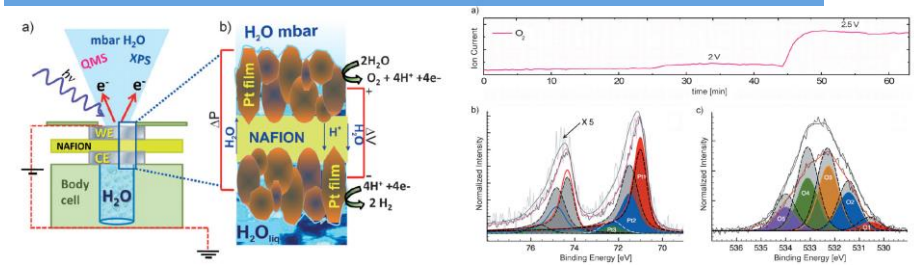

Angew. Chem. Int. Ed. **2013**, *52*, 11660 .

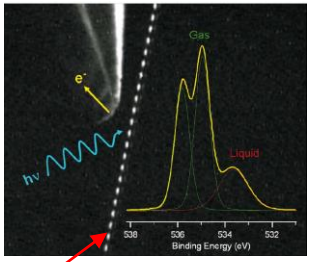

Droplets (χ=0.21 methanol aqueous) train

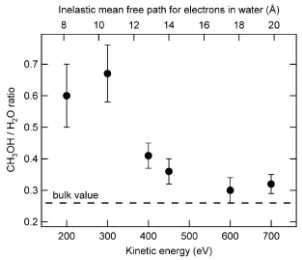

Phys. Chem. Chem. Phys. **2008**, 10, 3093.

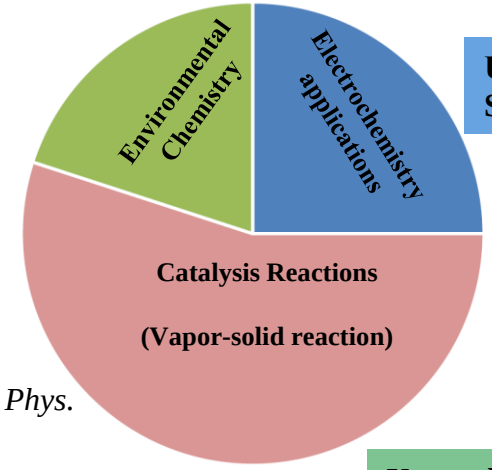

Using "Tender" X-ray APXPS as A Direct Probe of Solid-Liquid Interface

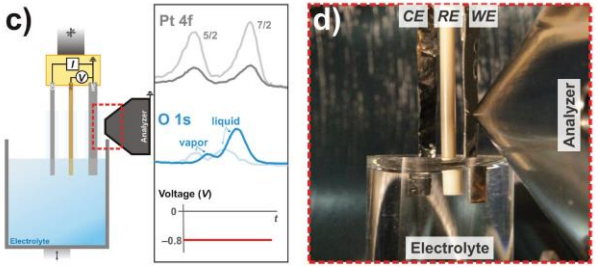

Scientific Reports, **2015**, *5*, 09788.

The Active Site of Methanol Synthesis over Cu/ZnO/Al_2O_3 Industrial Catalysts

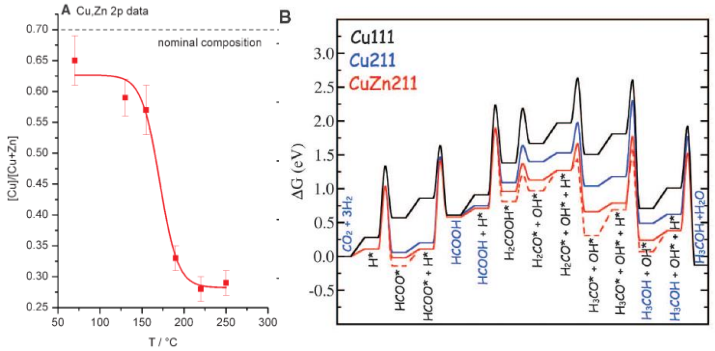

Science **2012**, *336*, 893.

Unravelling the effect of charge dynamics at the plasmonic metal/semiconductor interface for CO_2 photoreduction

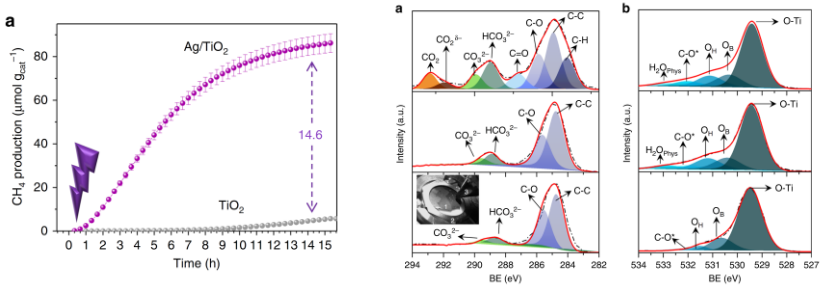

Nat. Comm. **2018**, *9*, 4986.

APXPS at TLS BL24A

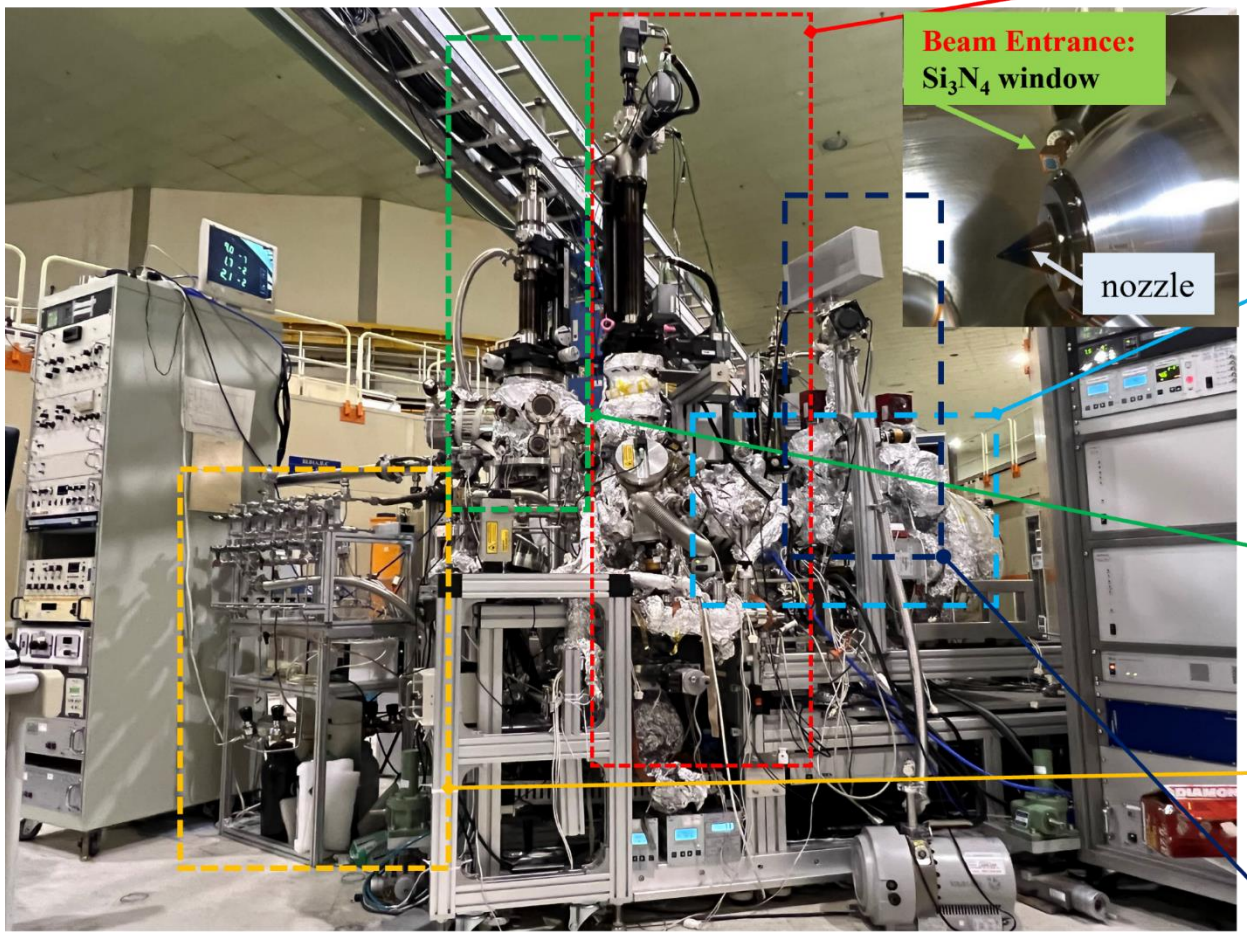

APXPS end station:
Main chamber:
- Backfilling Type mu-metal Chamber
- Five-axes manipulator (motors with TCP/IP interfaces, heating by laser heater, (Temp. RT.-1073 K)
- Ion Sputter

Analyzer:
- SPECS PHOIBOS 150 NAP Electron Energy Analyzer
- Pre-lens system
- lens cone cover with 300 um nozzle
- 1D DLD Detector

Preparation Chamber:
- hydrogen cracker
- Ion Sputter
- Four-axes manipulator (heating by e-beam heater)

Gas line system:
Gas phase: H_2, N_2, O_2, CO_2
Liquid Phase: H_2O, CH_3OH

Mass:
Hiden HAL/3F PIC 510,
Detection range: 1- 500 amu.

Commissioning results

APXPS

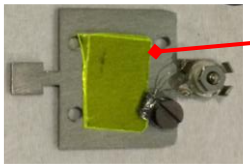

Sample: Ce:YAG fluorescent crystal coated by Au

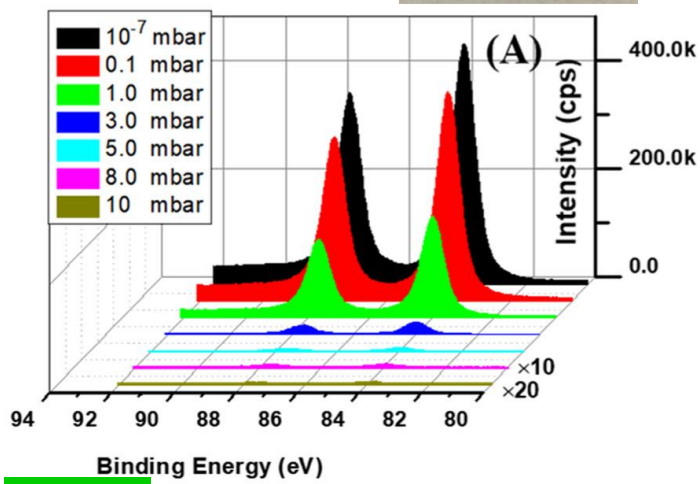

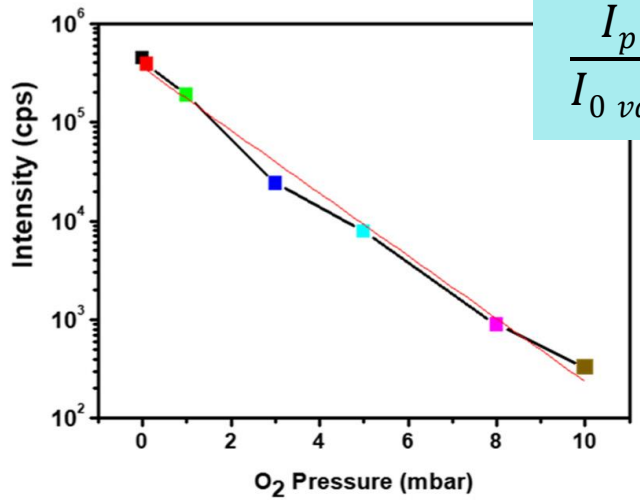

The scattering of electron by gas molecule

$$\frac{I_p}{I_{0\ vac}} \propto exp - (\sigma dp)$$

The maximum operating pressure:
10 mbar for a nozzle with a diameter of 300 um.
3 mbar for a nozzle with a diameter of 500 um.

XAS

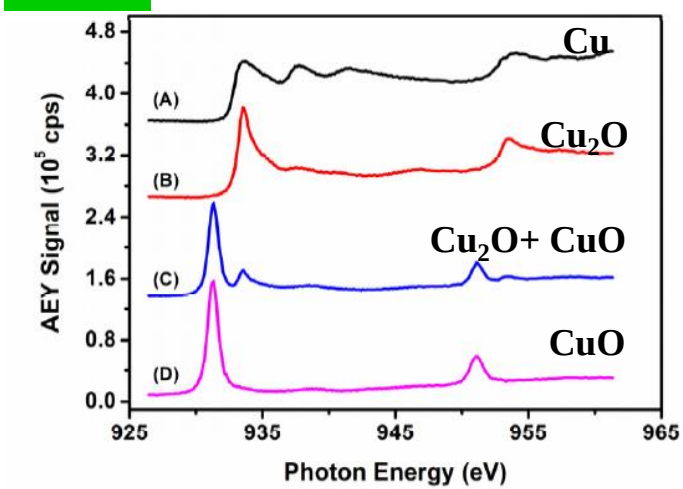

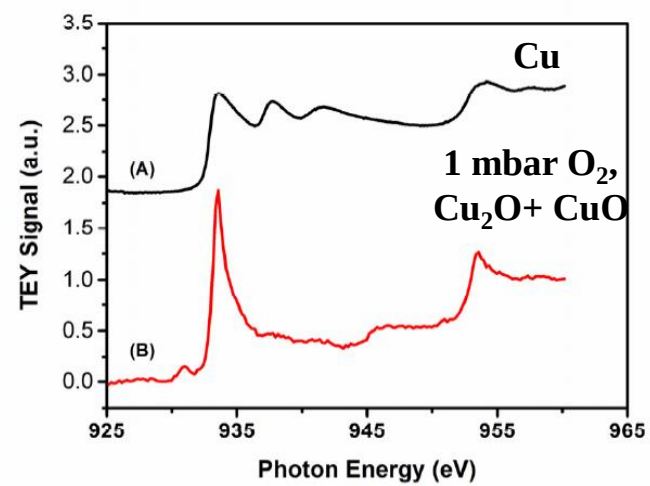

C.H. Wang, et al., AIP Conference Proceedings **2019,** *2054, 040012.*

Scientific results (1)

Journal of
Materials Chemistry A

ROYAL SOCIETY OF CHEMISTRY

PAPER

View Article Online
View Journal | View Issue

Check for updates

Cite this: *J. Mater. Chem. A*, 2020, **8**, 12744

Local synergetic collaboration between Pd and local tetrahedral symmetric Ni oxide enables ultra-high-performance CO_2 thermal methanation†

Che Yan,[a] Chia-Hsin Wang,*[b] Moore Lin,[c] Dinesh Bhalothia,[a] Shou-Shiun Yang,[a] Gang-Jei Fan,[c] Jia-Lin Wang,[c] Ting-Shan Chan,[b] Yao-lin Wang,[d] Xin Tu,[d] Sheng Dai,[e] Kuan-Wen Wang,[f] Jr-Hau He[g] and Tsan-Yao Chen *[ahi]

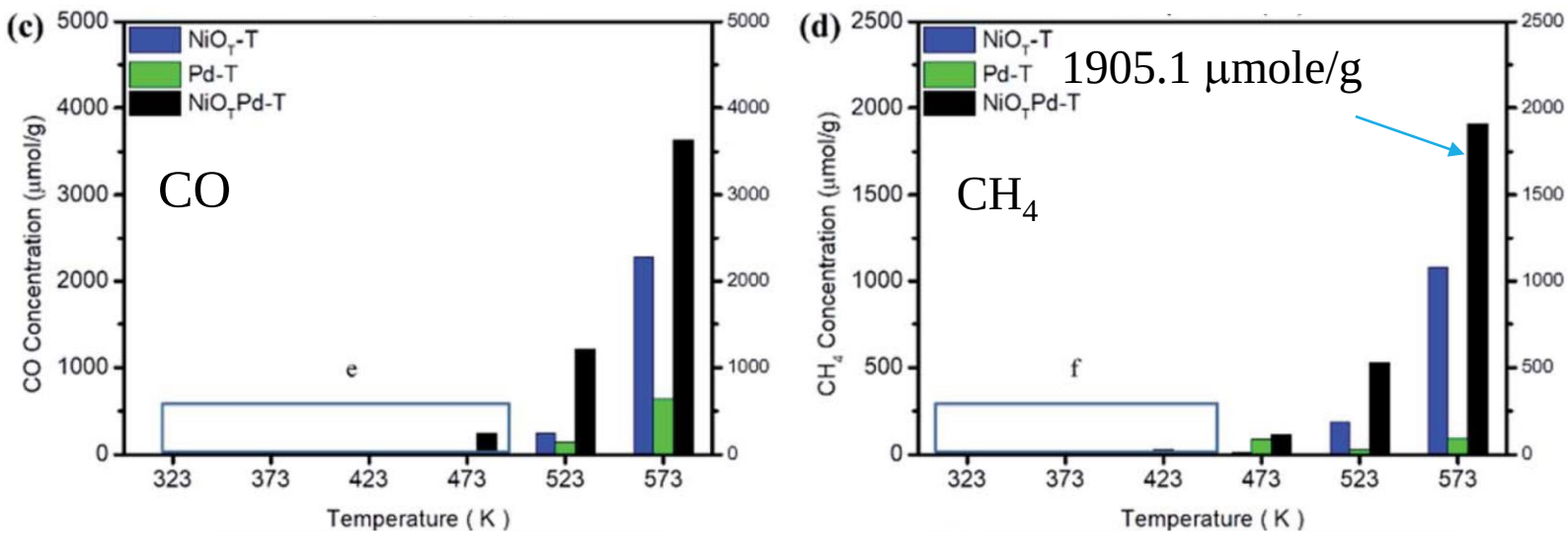

Operado-APXPS spectra for NiO_T-Pd-T nanocatalysts during CO_2RR

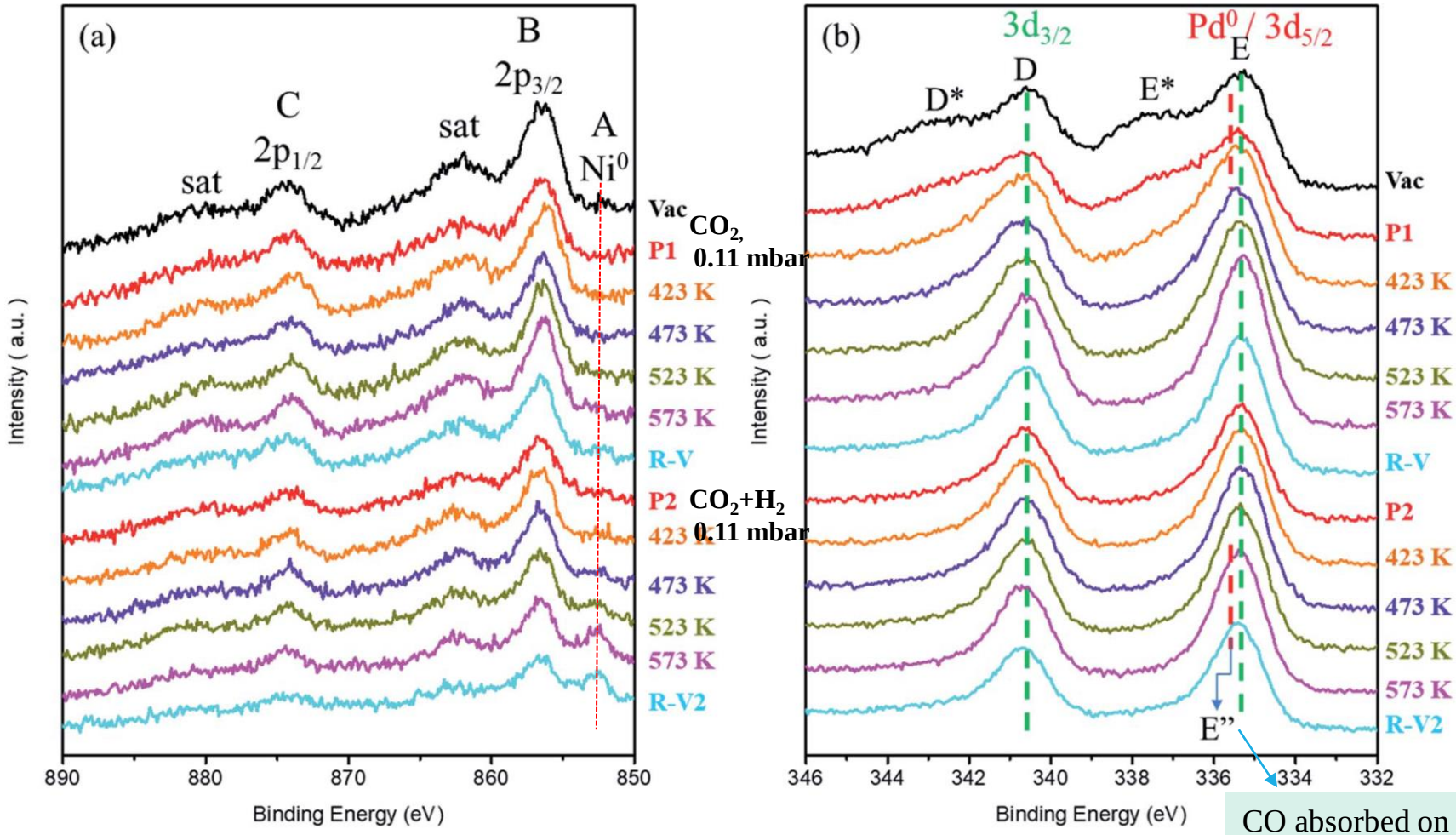

Fig. 5 *In situ* ambient-pressure X-ray photoelectron spectroscopy (APXPS) spectra of NiO_TPd-T in the (a) Ni 2p and (b) Pd 3d regions. The spectra are measured starting from under vacuum (Vac) to an atmosphere of CO_2 at 0.11 mbar at room temperature (P1) and then with the temperature increasing up to 573 K. After that, the chamber was placed under vacuum and allowed to cool to room temperature (R-V), then purged using a reaction gas of CO_2 and H_2 with a ratio of 1 : 3 for CO_2 : H_2 (P2) and heated from 423 to 573 K.

Possible Reaction Scheme

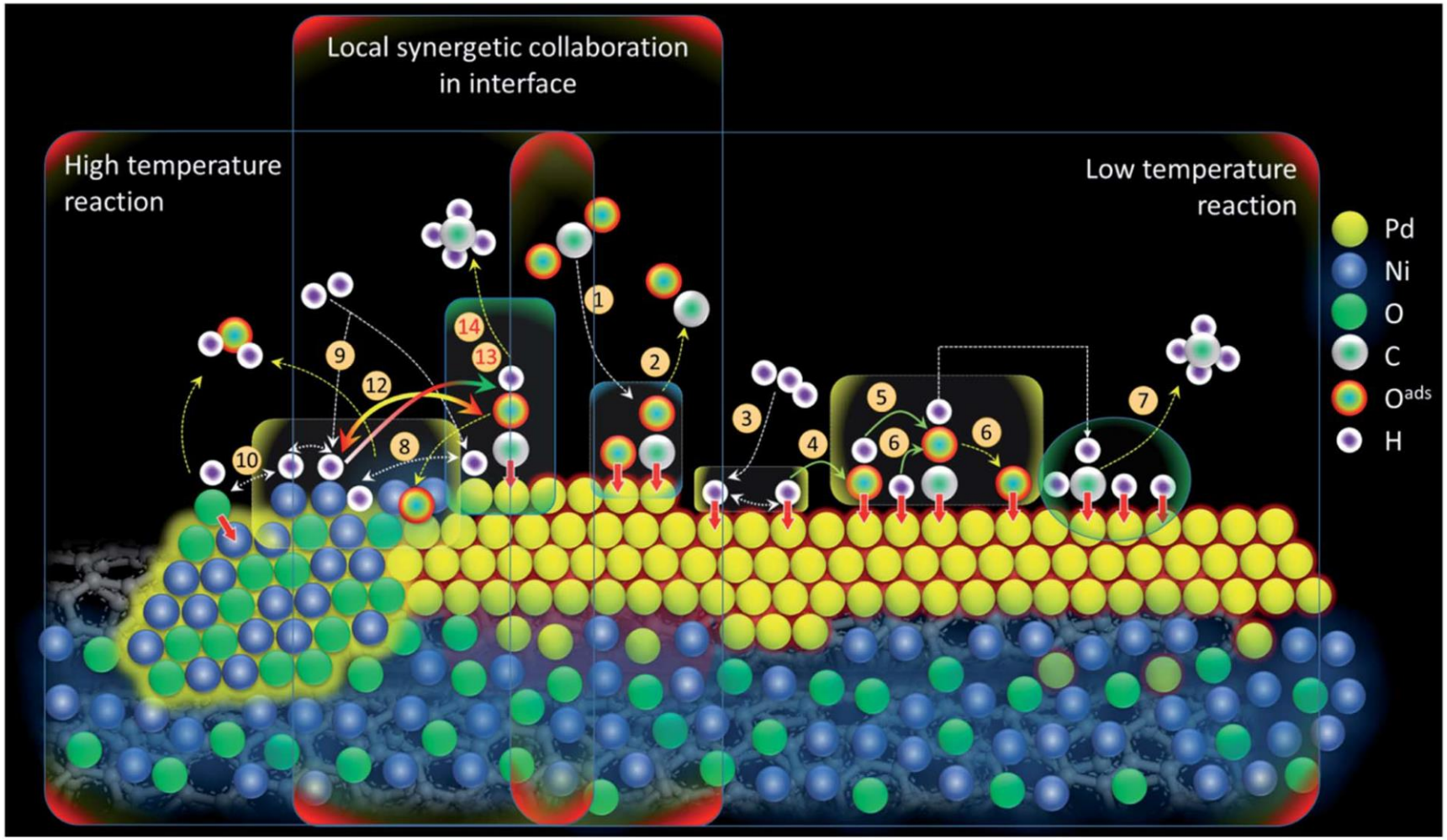

Scheme 1 Schematic representation of the reaction coordinates in the NiO_TPd-T.

Scientific results (2)

Nano Energy 83 (2021) 105830

Contents lists available at ScienceDirect

Nano Energy

journal homepage: http://www.elsevier.com/locate/nanoen

Electrochemical reduction of CO_2 in ionic liquid: Mechanistic study of Li–CO_2 batteries via *in situ* ambient pressure X-ray photoelectron spectroscopy

Yu Wang [a], Wanwan Wang [a], Jing Xie [a], Chia-Hsin Wang [b], Yaw-Wen Yang [b], Yi-Chun Lu [a,*]

The electrochemical was constructed based on a two-compartment cell configuration

LAGP: $Li_{1.5}Al_{0.5}Ge_{1.5}(PO_4)_3$ (Li-ion ceramic conductor)

CO_2 ($p(CO_2)$ = 5 mbar), CO_2/H_2O ($p(CO_2:H_2O$ = 2:1) = 5 mbar) and CO_2/O_2 ($p(CO_2: O_2$ = 2:1) = 5 mbar)

In situ APXPS data for Li-CO_2 battery under CO_2

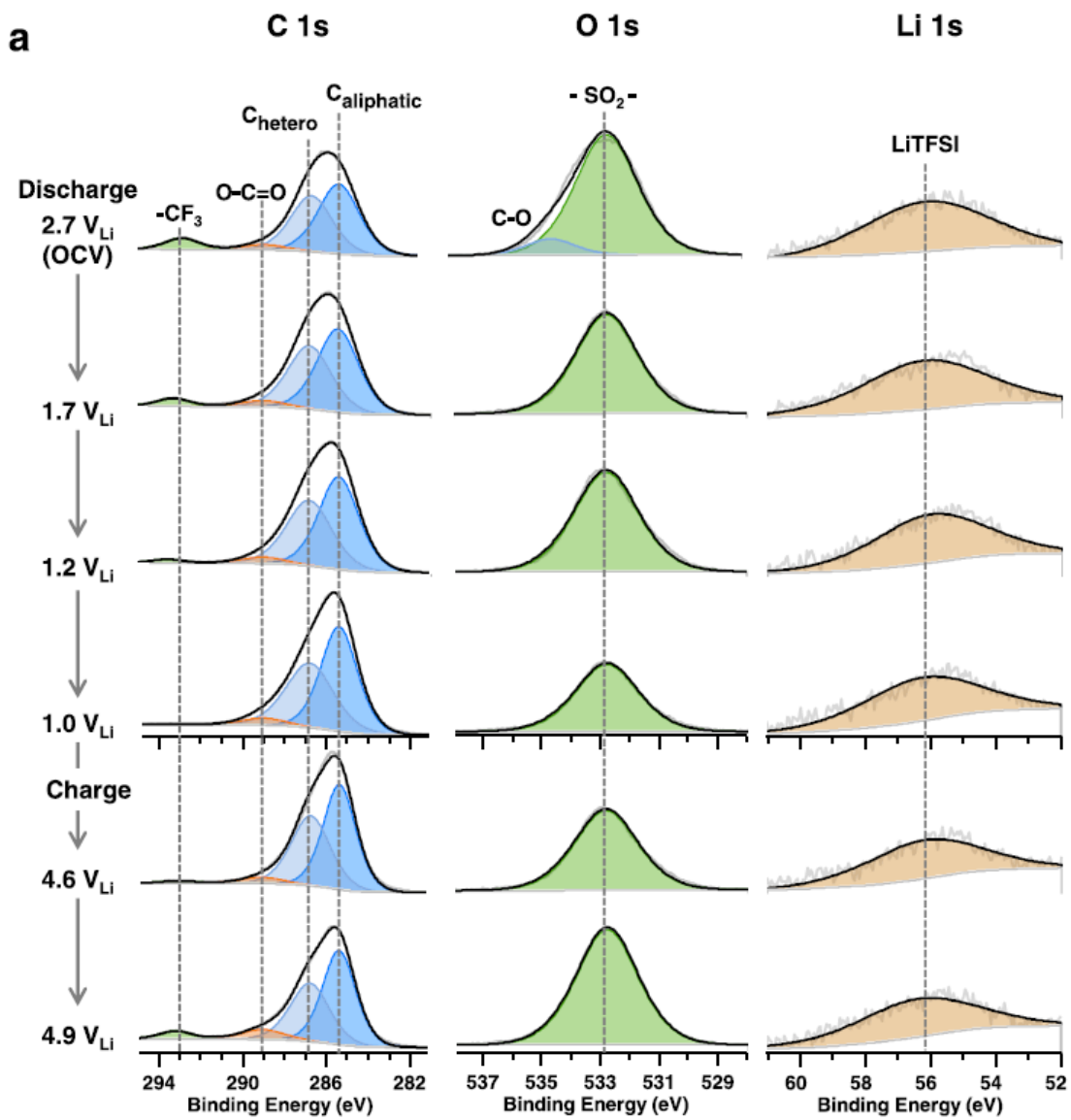

The C 1s, O 1s and Li 1s spectra as a function of potential applied across the two-compartment cell during discharge in $p(CO_2)$ = 5 mbar and charge in HV.

Li salt

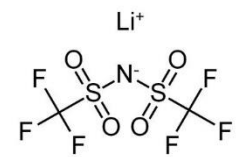

Ionic liquid

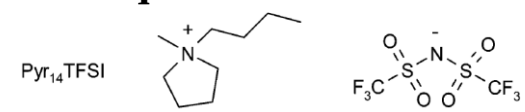

No new species were observed during the entire discharging and charge process, indicating that pure CO_2 reduction on the carbon electrode is not electrochemically active, which is in accordance with the negligible capacity observed in CO_2 gas.

In situ APXPS data for Li-CO_2 battery under CO_2 and H_2O

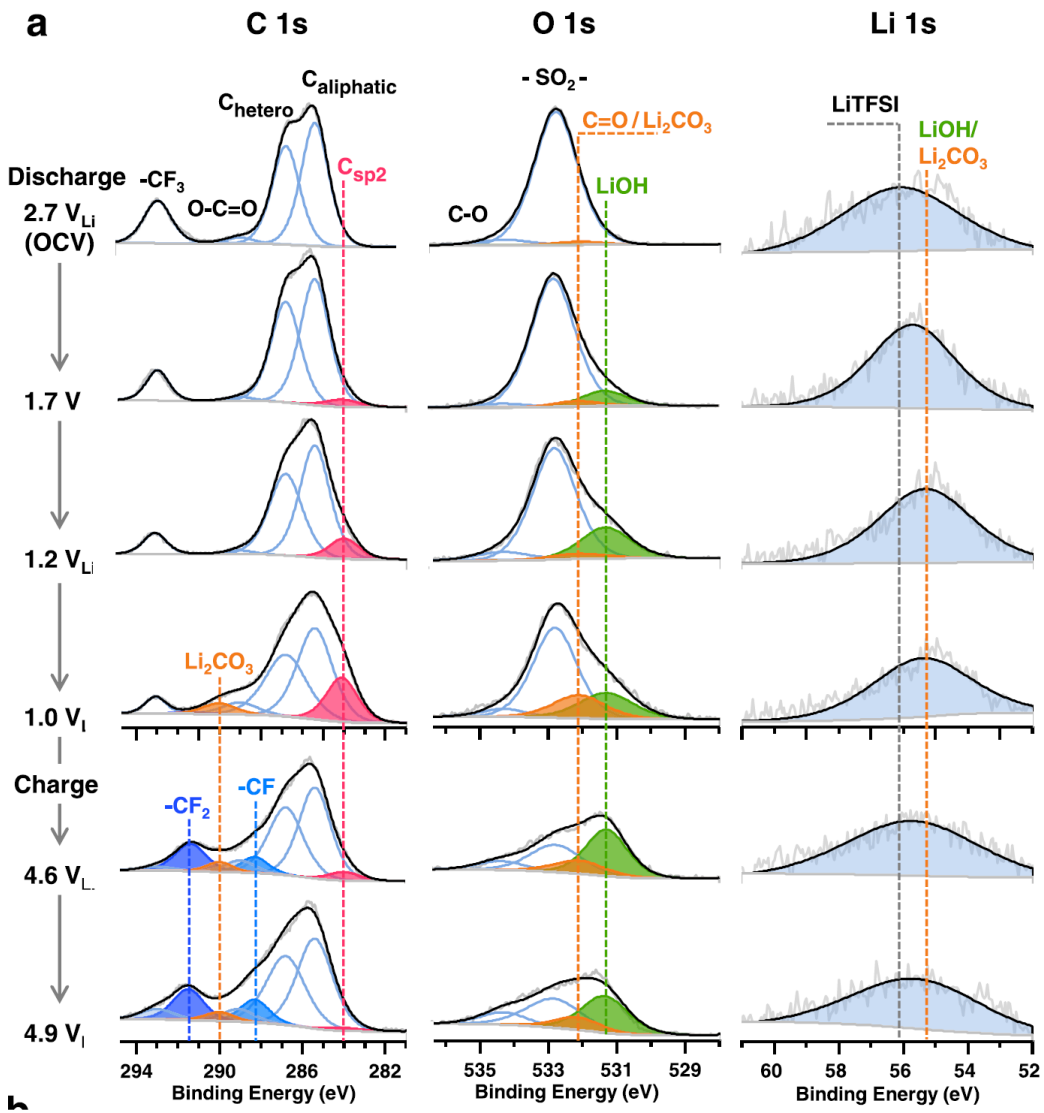

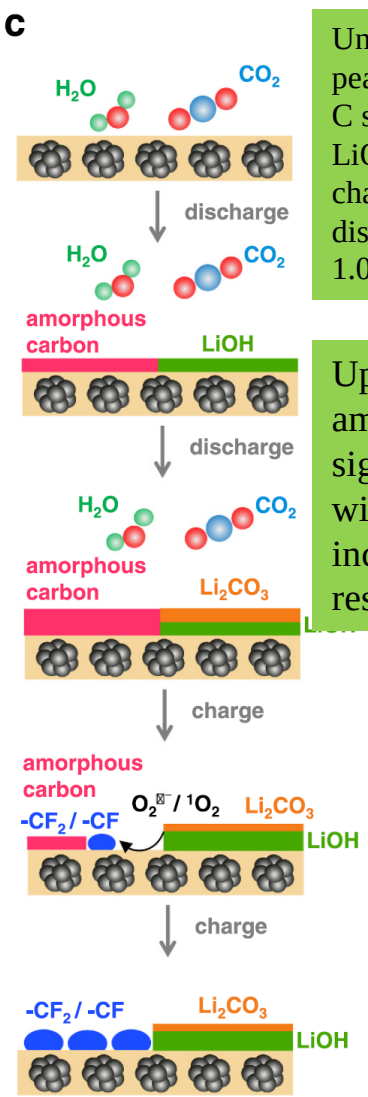

Under discharge condition, a new peak centering at ~ 284 eV (labeled C sp^2) gradually increased in C 1s. LiOH was observed first and then change to $LiCO_3$ while the discharge potential form 1.7 V to 1.0 V in O1s and Li1s.

Upon charging to 4.9 V, the amorphous carbon was significantly reduced along with a moderate decrease and increase of Li_2CO_3 and LiOH, respectively

Water plays a critical role in promoting CRR in non-aqueous electrolyte. However, the Li_2CO_3 and LiOH remained on the electrode when charged to 4.9 V, indicating a poor rechargeability of Li_2CO_3 and LiOH, which is consistent with the literature report.

In situ APXPS data for Li-CO_2 battery under CO_2 and O_2

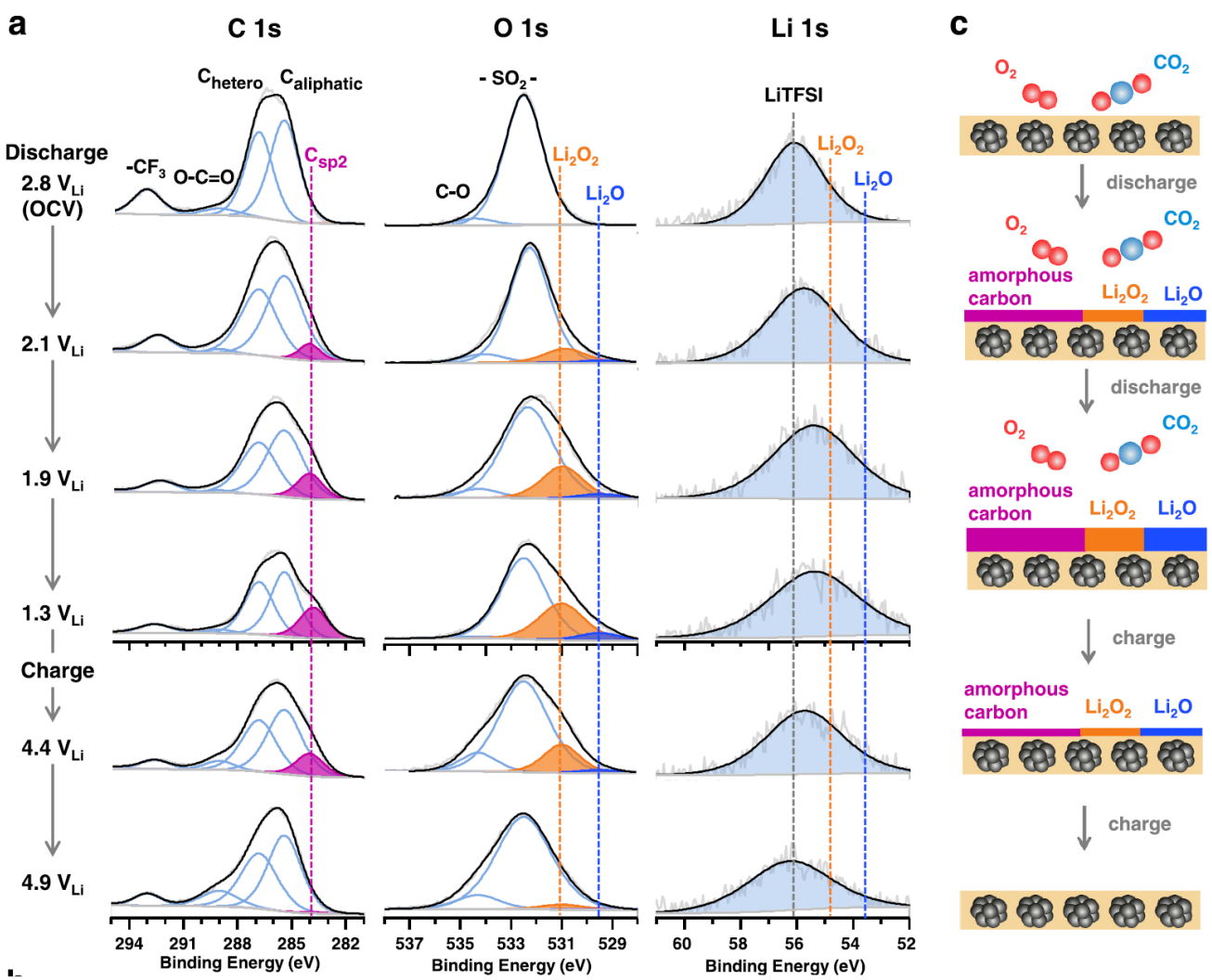

Under discharge conditions, a new peak centering at ~ 284 eV (labeled C sp^2) gradually increased in C 1s. Li_2O, and Li_2O_2 increased as well in O1s and Li1s.

Upon charge conditions, the amorphous carbon, Li_2O, and Li_2O_2 were completely removed at the end of the charging of 4.9 V.

The formed amorphous carbon, Li_2O_2 and Li_2O show higher rechargeability and faster kinetics compared with Li_2CO_3-oxidation. These new findings provide direct evidence of CRR mechanism and insights in resolving the discrepancy on CRR kinetics in Li–CO_2 batteries.

From Vapor-Solid Reaction to Liquid-Solid Reaction

Vapor-Solid Reaction

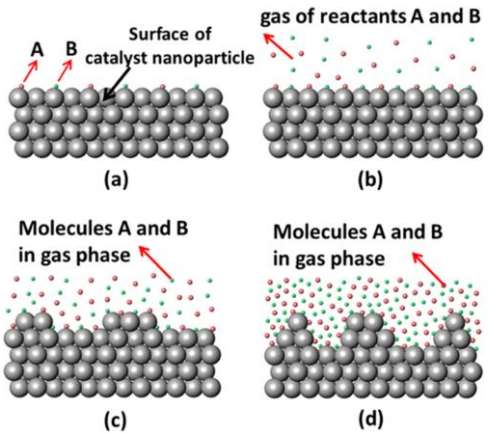

Chem. Rev. 2019, 119, 6822−6905

Electron inelastic mean free path in solid as a function of electron kinetic energy.

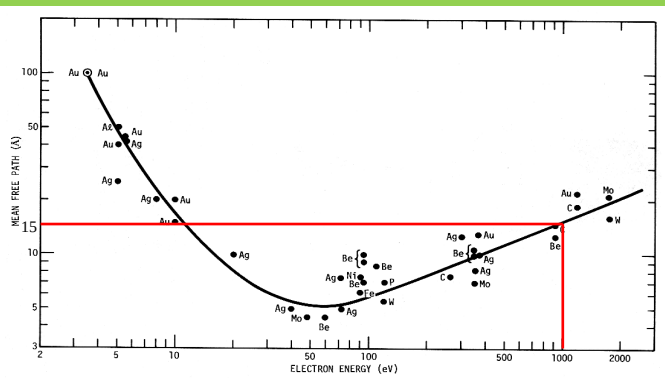

Figure 5.11. The mean free path of electrons in different solids as a function of the kinetic energy of the electrons [56].

Liquid-Solid Reaction

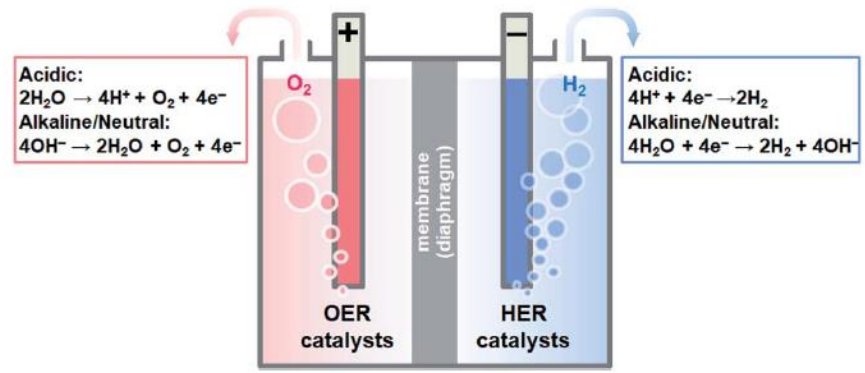

Sustainable Energy Fuels, 2020, 4, 3211

Electron inelastic mean free path in liquid water as a function of electron kinetic energy.

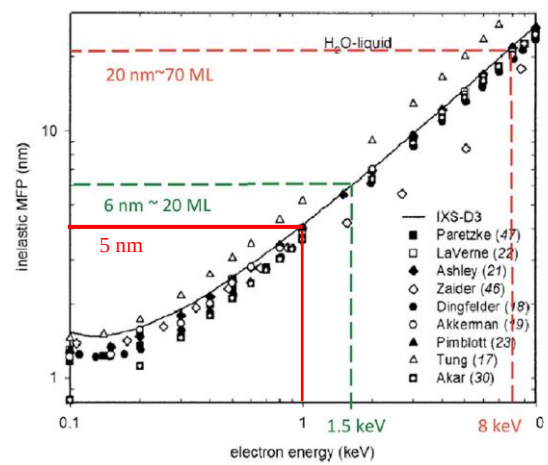

Faraday Discuss., 2015, 180, 35–53

Electrochemical cells for *in situ* X-ray spectroscopies

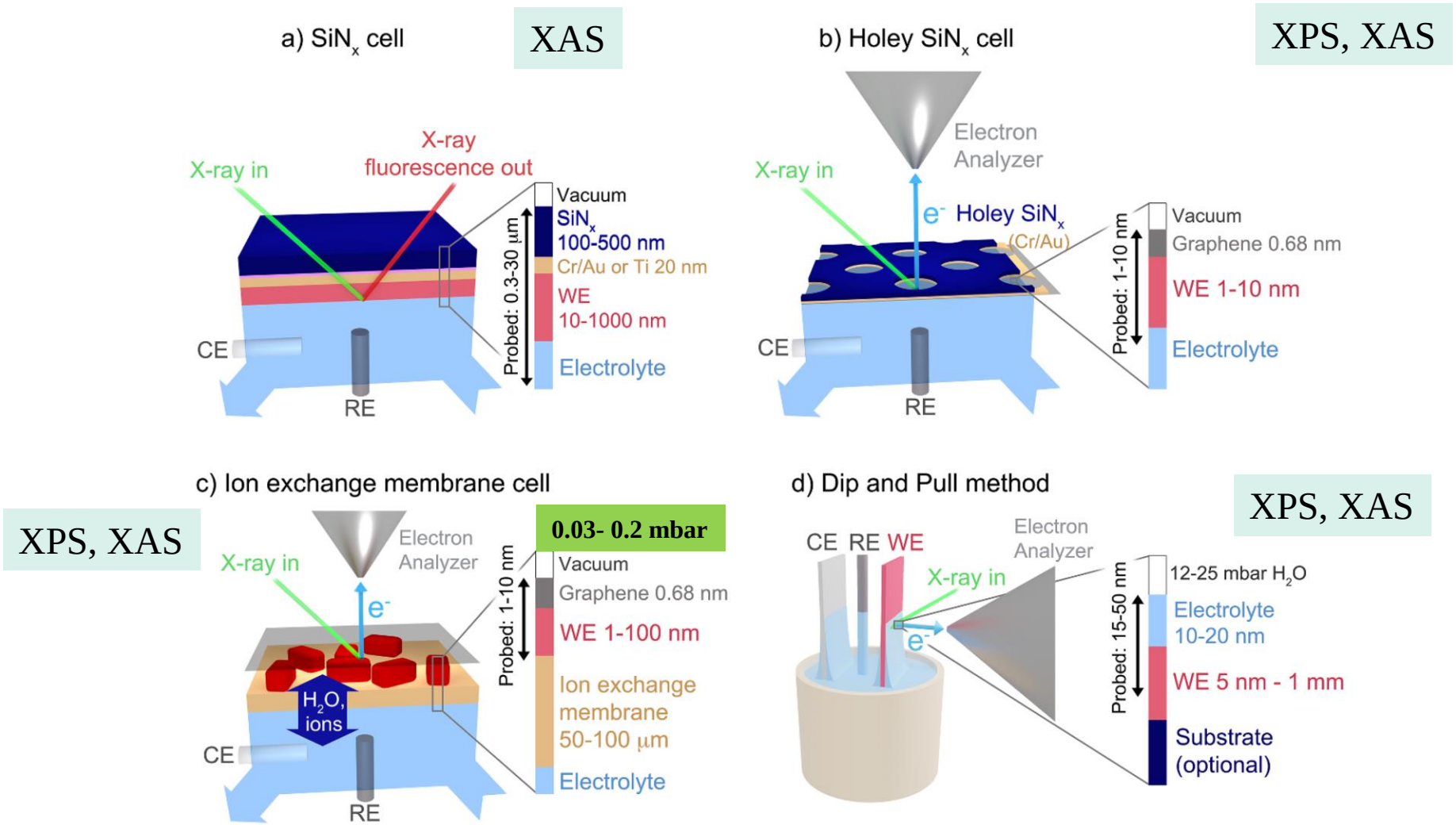

J. Phys. D: Appl. Phys. **2021**, *54*, 124003.

Three-Electrode electrochemical cells at TLS BL24A

- Static electrochemical cell

Chamber pressure ~ 0.3 mbar

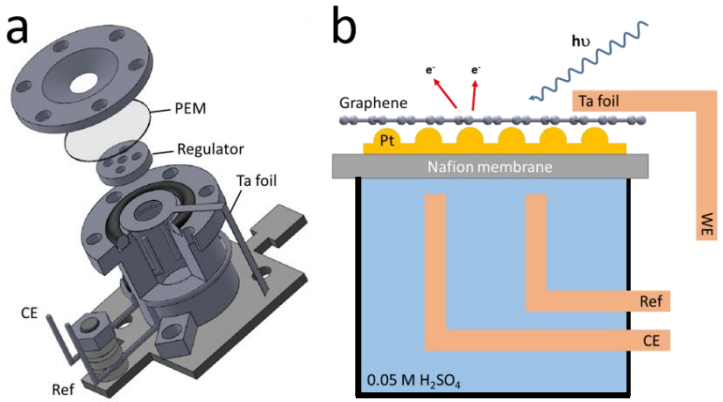

- Constant flow electrochemical cell system

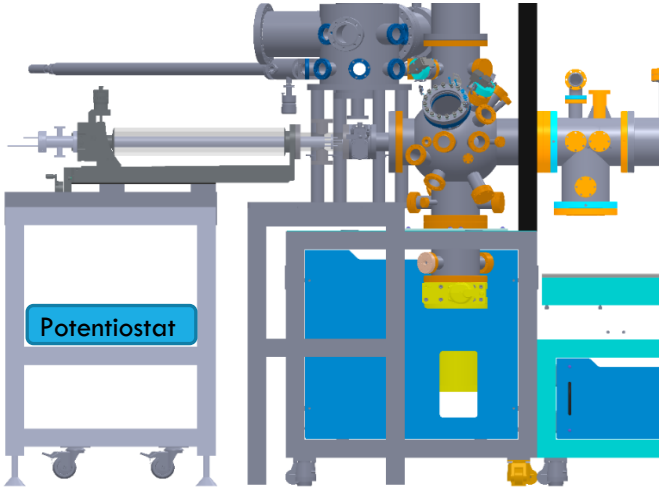

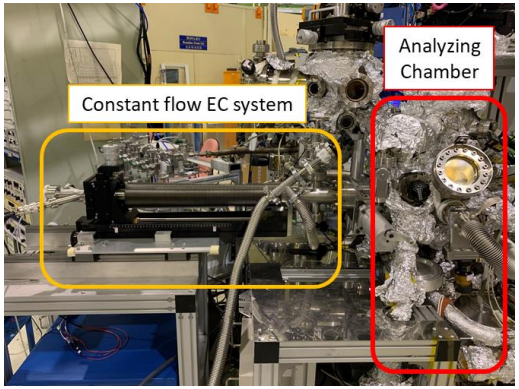

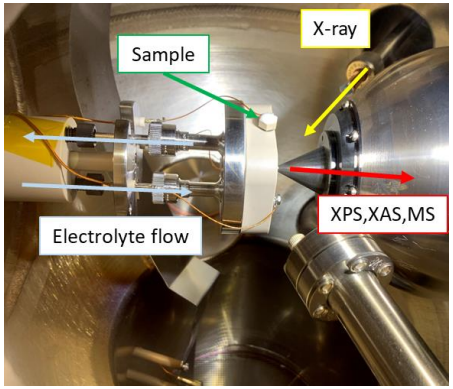

- As static EC cell could be transferred on the standard sample holder, we also come up with the constant flow electrolyte system for extending the measuring time.

Revealing the Surface Species Evolution on Low-loading Platinum in an Electrochemical Redox Reaction by Operando Ambient-Pressure X-ray Photoelectron Spectroscopy

- Sample : ML Graphene/Pt(1, 3 or 5)/Nafion117

  (Pt1, 3 or 5 for depositions amounts of 1, 3, 5 nm)
- Reaction environment: 0.05 M H_2SO_4
- Morphology characterization of the as-deposited samples

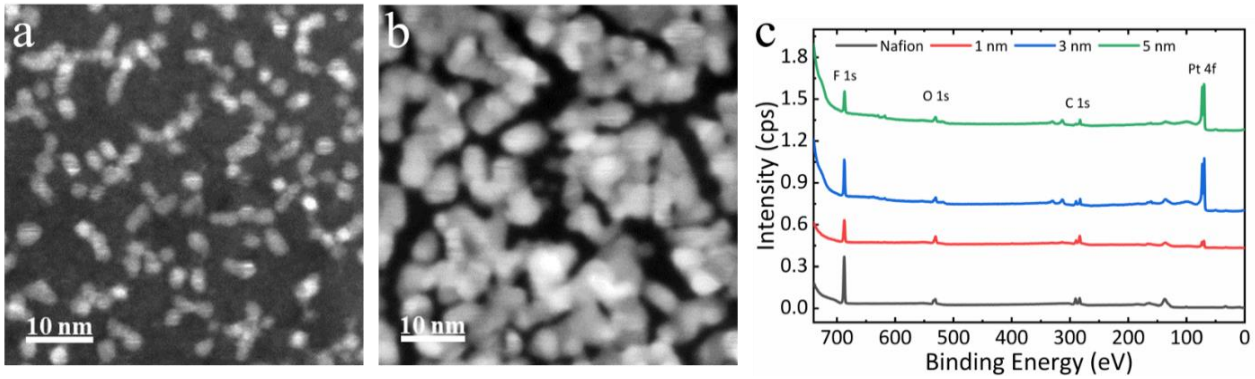

- Peak intensity ratio: F 1s : Pt 4f = 3.2, 0.78, 0.4
- Probing depth (3λ): 790 eV ≈ 1.6 nm

- The catalyst morphology was concluded as a discontinuous film on the Nafion substrate. This discontinuous film allows water and ions from the back side of the Nafion substrate to diffuse onto the Pt catalyst's surface and then act as the reactant during OER.

Operando XPS results during the redox process

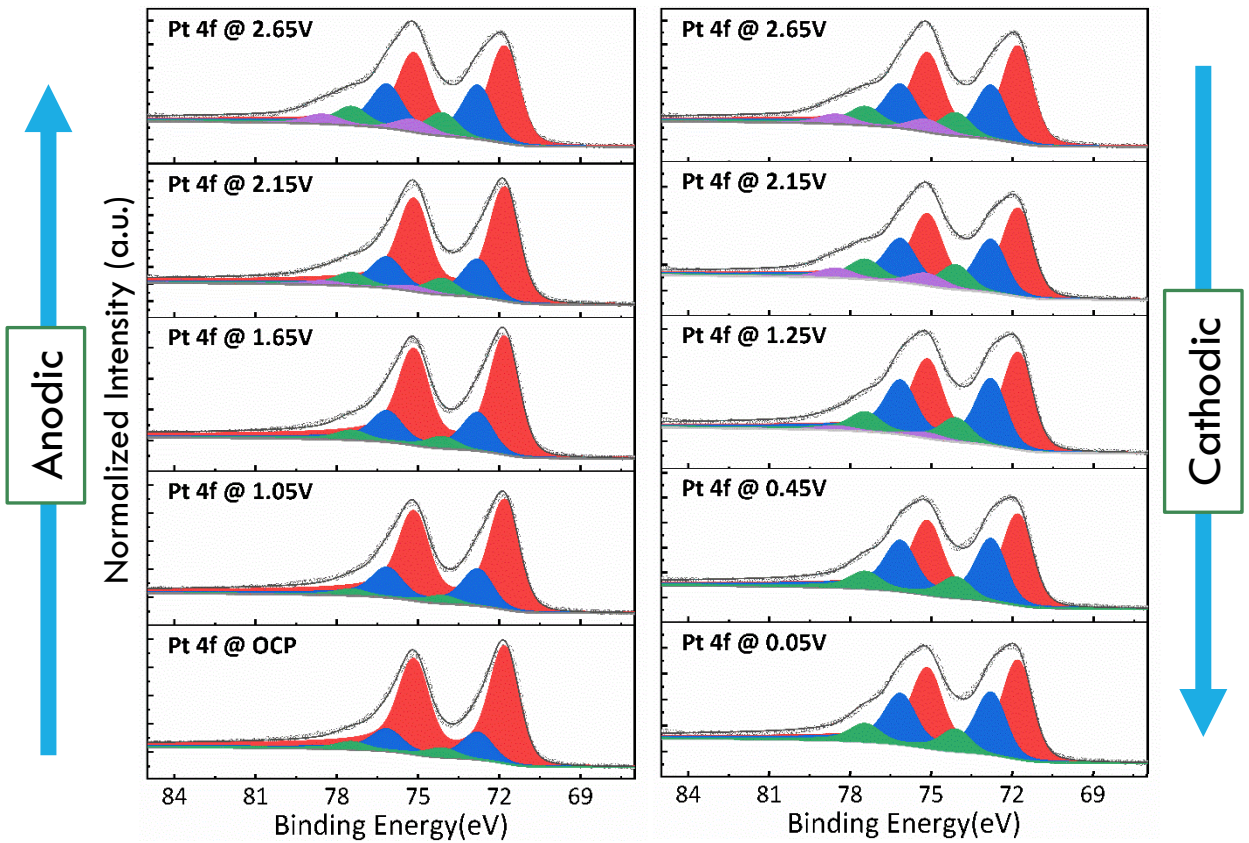

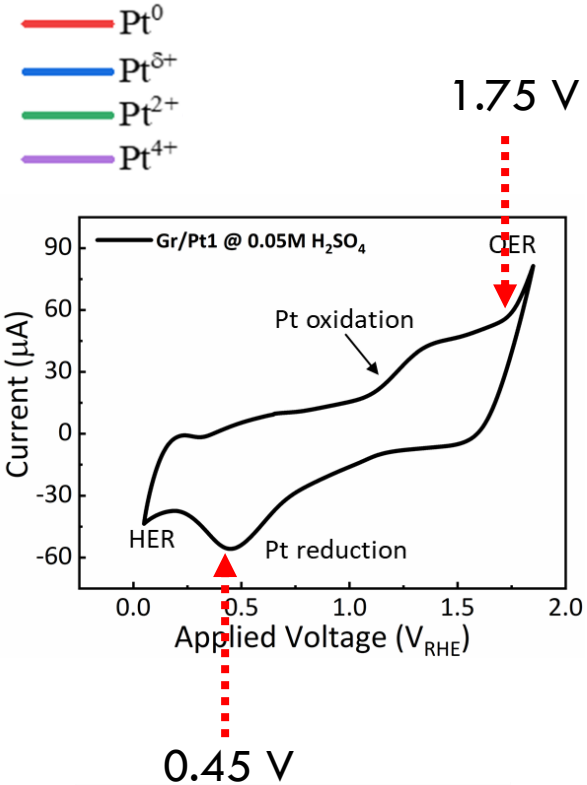

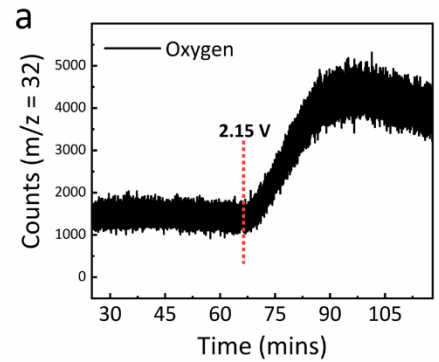

- Operando observation of XP spectra was achieved with the static reaction cell under different applied voltages.

Oxide Species evolution during redox reaction

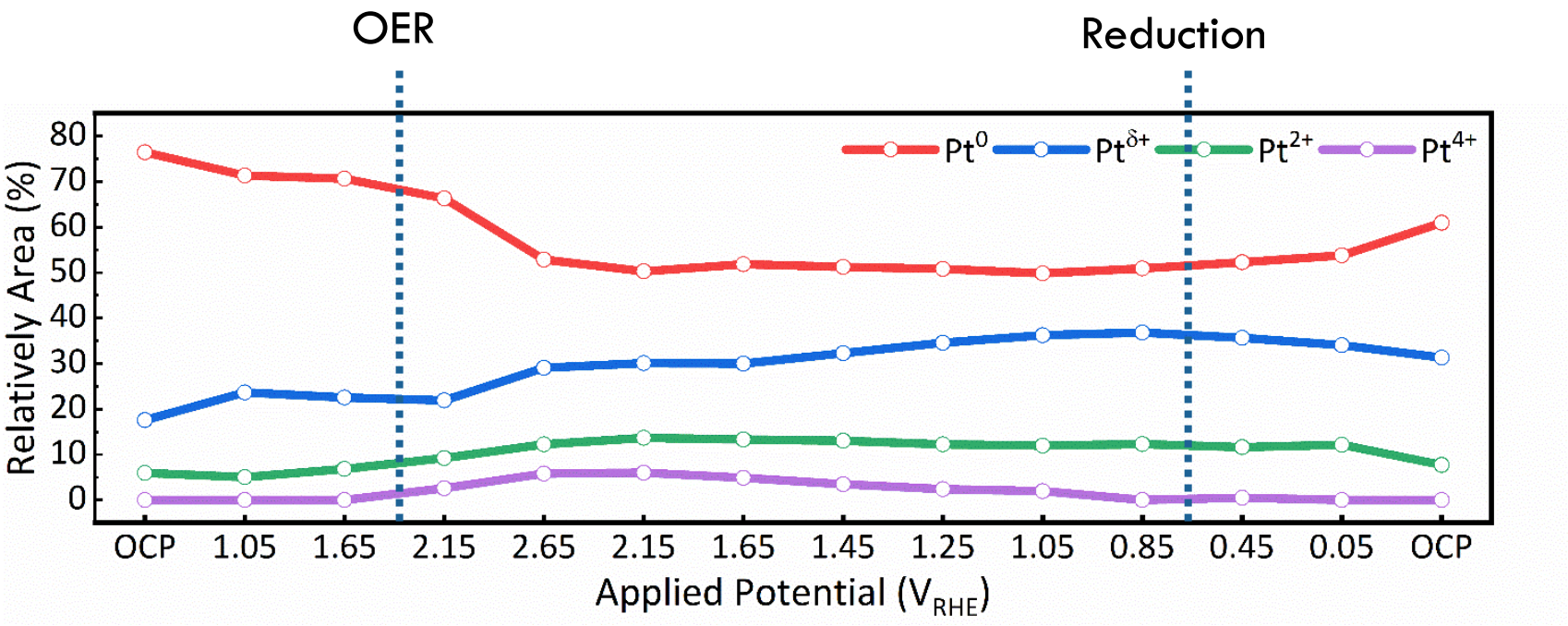

- The amount of Pt^{2+} increased with an increment of the anodic potential, whereas Pt^{4+} suddenly formed when the applied voltage was set to cross the threshold voltage of the OER.
- At the cathodic process, Pt^{4+} was completely reduced when returning to the open circuit potential. However, the Pt^{2+} species changed slightly, indicating the possibility of oxide reduction from tetravalent to divalent oxide or the formation of hydrated oxide species.

Evolution of the oxide species on the surface and subsurface

The probing depth is around 3.84 nm and 2.85 nm for the Pt catalyst using X-ray energies of 635 and 380 eV, respectively.

- Anodic Process

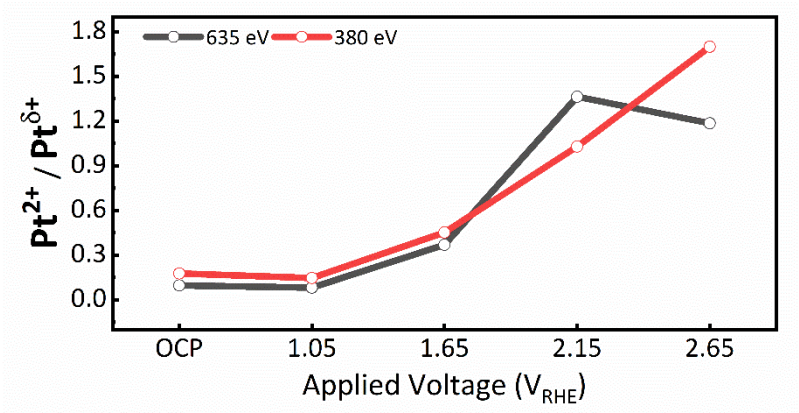

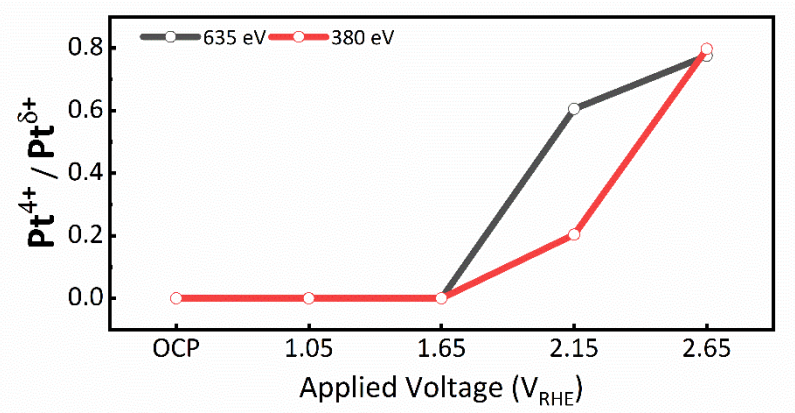

- The $Pt^{2+}/Pt^{\delta+}$ ratio was almost identical for the two X-ray energies when the applied voltage was changed from the OCP to 2.15 V. However, at an applied voltage of 2.65 V, the $Pt^{2+}/Pt^{\delta+}$ was higher by using the lower photon excitation energy.

- The $Pt^{4+}/Pt^{\delta+}$ ratio was higher when the X-ray energy of 635 eV was employed at the applied voltage of 2.15 V, indicating Pt^{4+} species has occurred at the subsurface of the catalyst.

Operando valence band spectra of Pt 1(nm) during an anodic sweep

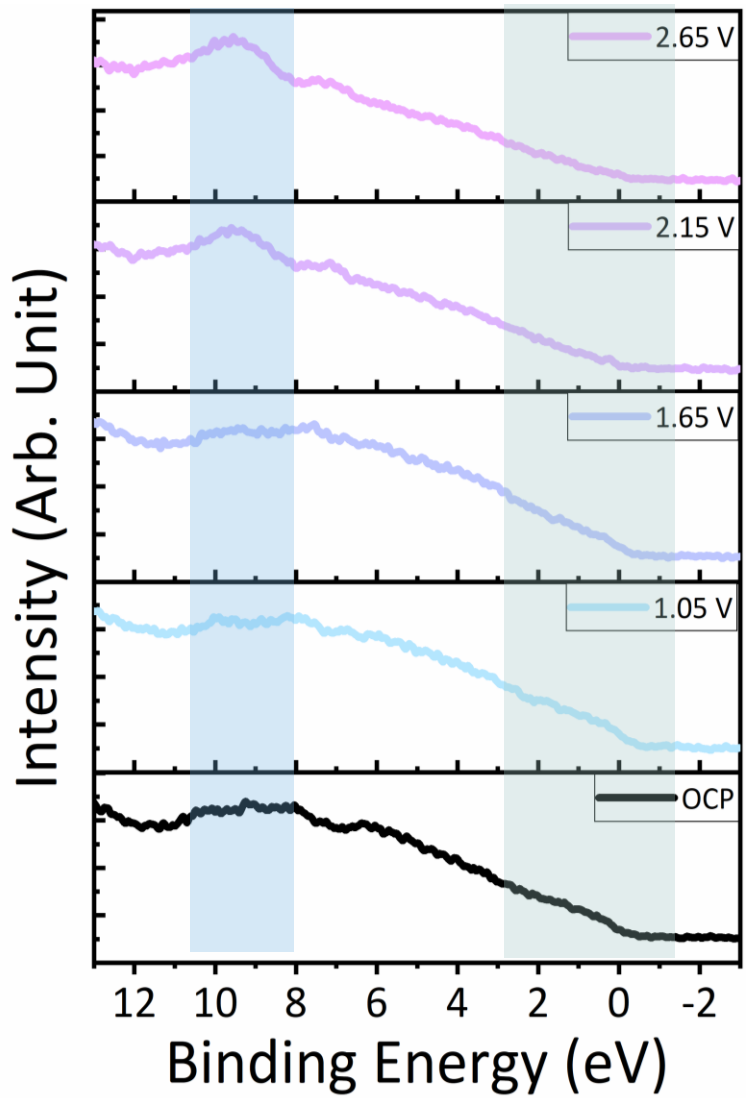

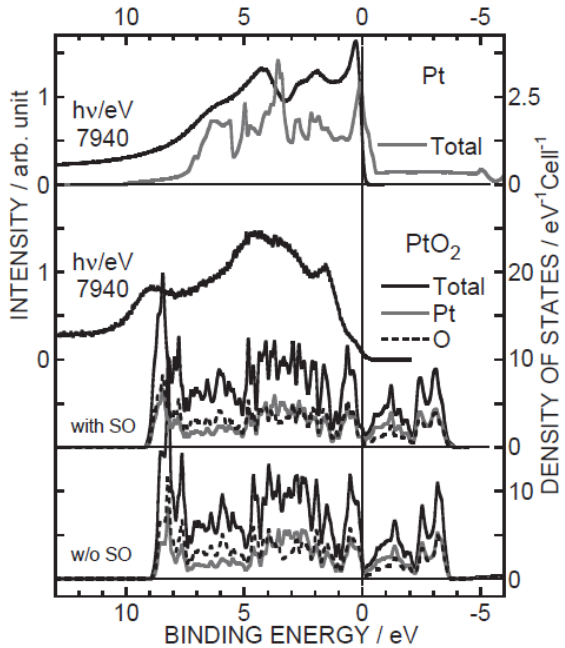

J. Phys. Soc. Jpn. 87, 044701 (2018)

As the anodic polarization progressed, a peak started to develop at approximately 9.5 eV, whereas the electron density near the Fermi edge decreased.

Schematic of surface oxide species evolution during redox process

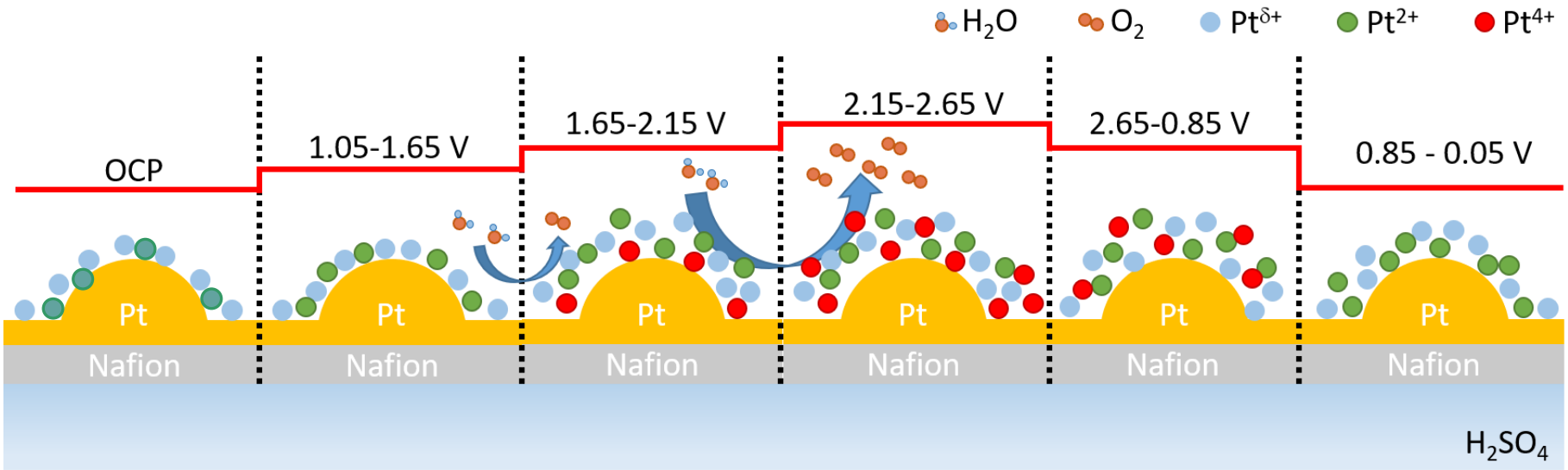

- We proposed that the mixed-valence oxidation layer at the Pt catalyst surface reinforces the absorption ability of water and hydroxyl groups; The interface between the metallic Pt and mixed-valence oxidation thin layer boosts the OER activity further.

ChemCatChem **2023**, *15*, e202300359.

RESEARCH ARTICLE

ADVANCED FUNCTIONAL MATERIALS
www.afm-journal.de

Decreasing the O_2-to-H_2O_2 Kinetic Energy Barrier on Dilute Binary Alloy Surfaces with Controlled Configurations of Isolated Active Atoms

Adv. Funct. Mater., **2024**, *23*, 14281.

Shang-Cheng Lin, Chun-Wei Chang, Meng-Hsuan Tsai, Chih-Hao Chen, Jui-Tai Lin, Chia-Ying Wu, I-Ting Kao, Wen-Yang Jao, Chia-Hsin Wang, Wen-Yueh Yu, Chi-Chang Hu, Kun-Han Lin, and Tung-Han Yang**

O_2 Reduction Reaction (ORR)

The mechanism of 4e-ORR: **Thermodynamically favored**

$$O_2 + 4(H^+ + e^-) \rightarrow 2H_2O \qquad E^o = 1.23\ V_{RHE} \qquad (3)$$

$$* + O_2 + (H^+ + e^-) \rightarrow OOH^* \qquad (3a)$$

$$OOH^* + (H^+ + e^-) \rightarrow H_2O + O^* \qquad (3b)$$

$$O^* + (H^+ + e^-) \rightarrow OH^* \qquad (3c)$$

$$OH^* + (H^+ + e^-) \rightarrow H_2O + * \qquad (3d)$$

The mechanism of 2e-ORR:

$$O_2 + 2(H^+ + e^-) \rightarrow 2H_2O_2 \qquad E^o = 0.70\ V_{RHE} \qquad (4)$$

$$* + O_2 + (H^+ + e^-) \rightarrow OOH^* \qquad (4a)$$

$$OOH^* + (H^+ + e^-) \rightarrow H_2O_2 + * \qquad (4b)$$

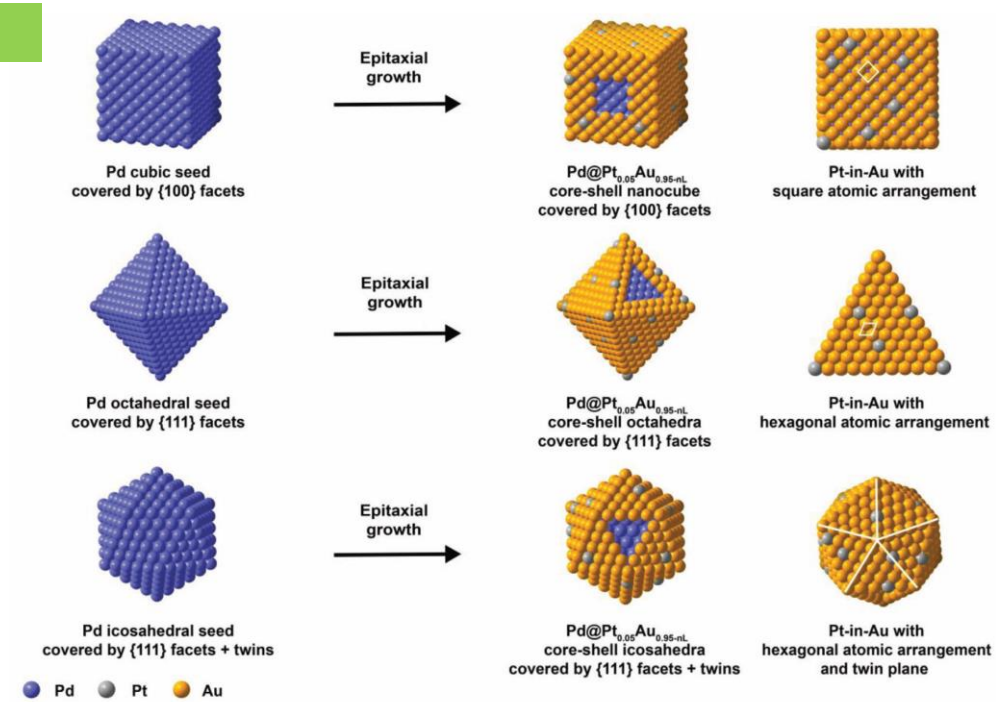

ACS Catal. 2020, 10, 7495−7511

RESEARCH ARTICLE

ADVANCED FUNCTIONAL MATERIALS
www.afm-journal.de

Decreasing the O_2-to-H_2O_2 Kinetic Energy Barrier on Dilute Binary Alloy Surfaces with Controlled Configurations of Isolated Active Atoms

Adv. Funct. Mater., **2024**, *23*, 14281.

Shang-Cheng Lin, Chun-Wei Chang, Meng-Hsuan Tsai, Chih-Hao Chen, Jui-Tai Lin, Chia-Ying Wu, I-Ting Kao, Wen-Yang Jao, Chia-Hsin Wang, Wen-Yueh Yu, Chi-Chang Hu, Kun-Han Lin, and Tung-Han Yang**

O_2 Reduction Reaction (ORR)

The mechanism of 4e-ORR: **Thermodynamically favored**

$$O_2 + 4(H^+ + e^-) \rightarrow 2H_2O \qquad E^o = 1.23\ V_{RHE} \qquad (3)$$

$$* + O_2 + (H^+ + e^-) \rightarrow OOH^* \qquad (3a)$$

$$OOH^* + (H^+ + e^-) \rightarrow H_2O + O^* \qquad (3b)$$

$$O^* + (H^+ + e^-) \rightarrow OH^* \qquad (3c)$$

$$OH^* + (H^+ + e^-) \rightarrow H_2O + * \qquad (3d)$$

The mechanism of 2e-ORR:

$$O_2 + 2(H^+ + e^-) \rightarrow 2H_2O_2 \qquad E^o = 0.70\ V_{RHE} \qquad (4)$$

$$* + O_2 + (H^+ + e^-) \rightarrow OOH^* \qquad (4a)$$

$$OOH^* + (H^+ + e^-) \rightarrow H_2O_2 + * \qquad (4b)$$

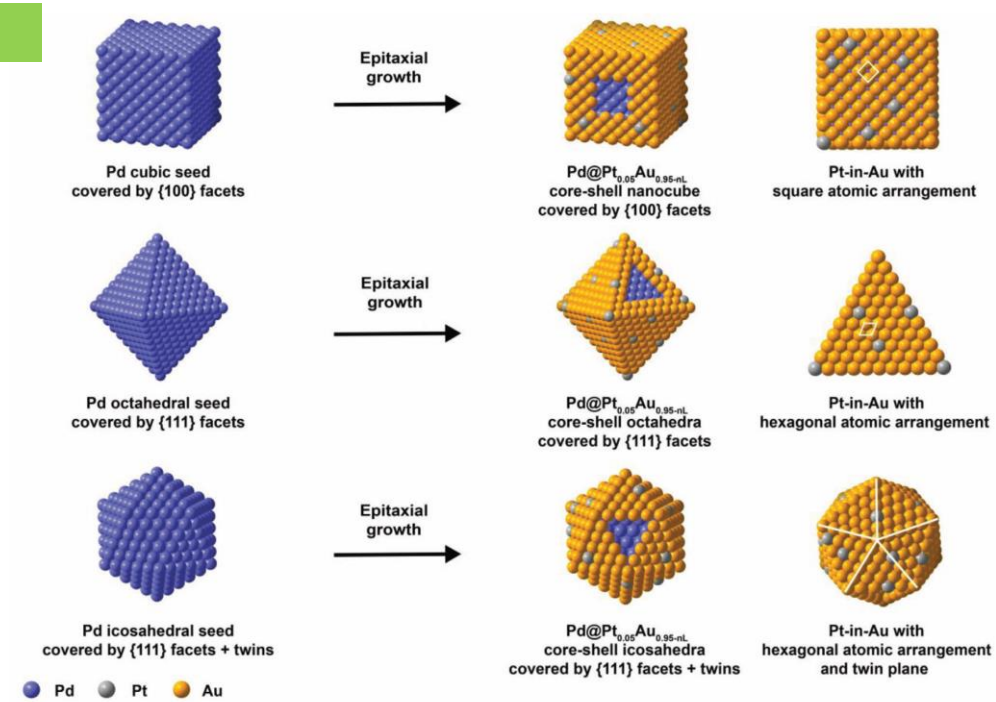

ACS Catal. 2020, 10, 7495−7511

Electrocatalytic ORR performance of Pd@M-in-Au core-shell nanocrystals through RRDE measurements in the O_2-saturated 0.1 M $HClO_4$ (M = Pt, Pd, and Rh).

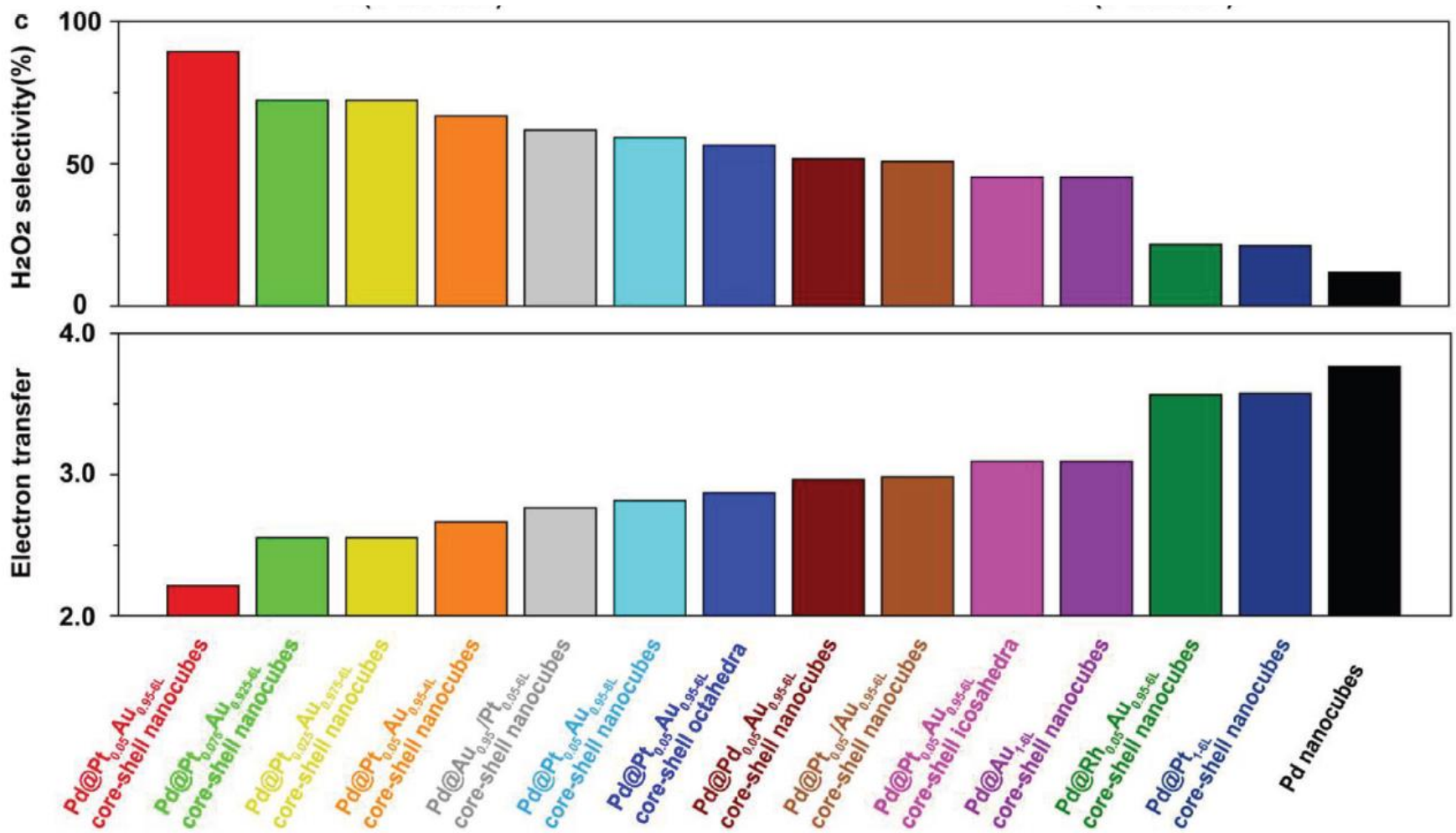

Operando synchrotron AP-XPS measurements of Pd@Pt-in-Au core-shell nanocrystals during the ORR.

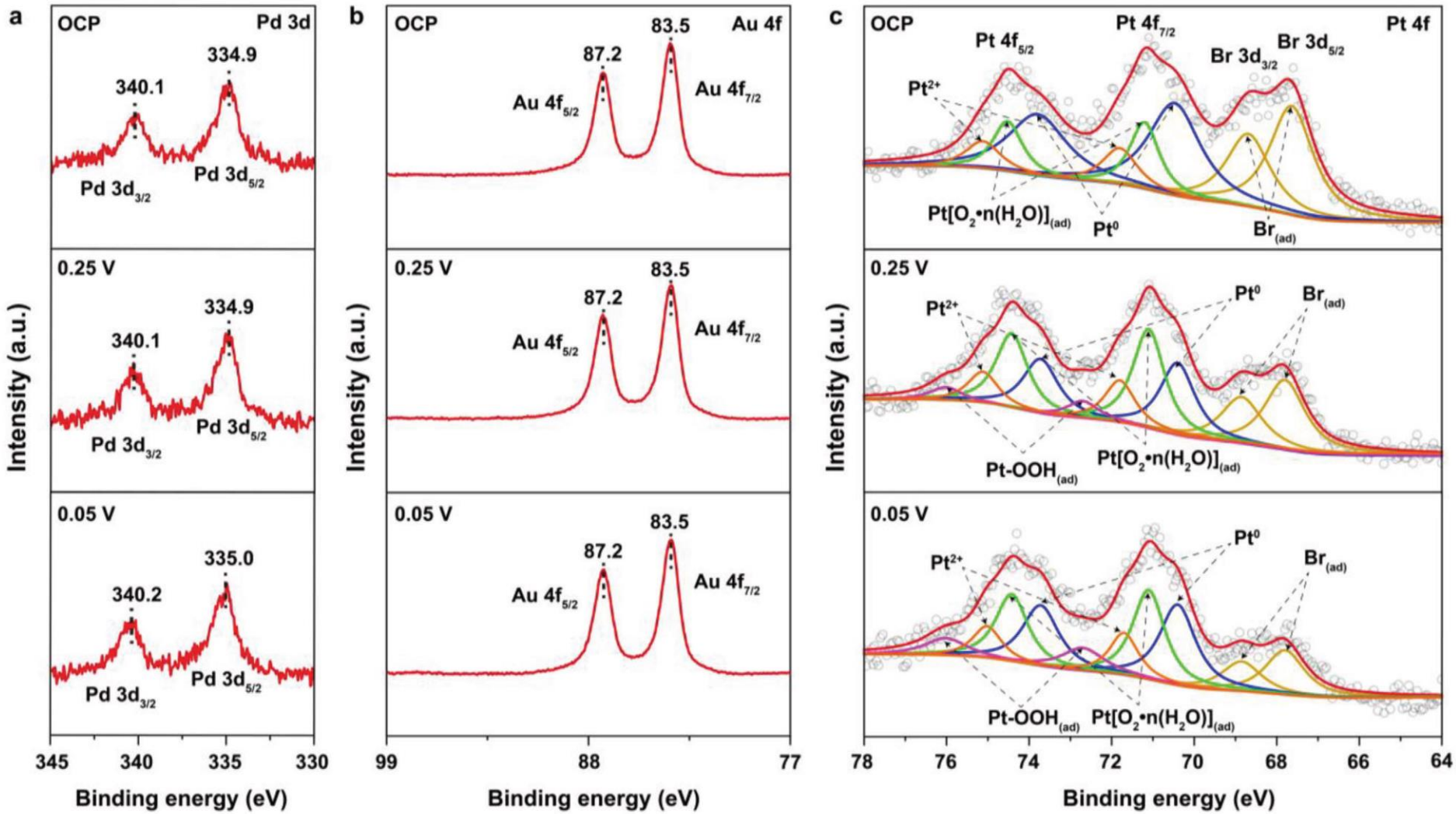

GC-DFT: kinetic Analysis. The relative grand potentials (ΔΩ) along the $2e^-$ ($OOH^* + H^+ + e^- \rightarrow H_2O_2$) and $4e^-$ ($OOH^* + H^+ + e^- \rightarrow O^* + H_2O$) ORR reaction pathways at U = 0.4 V (vs SHE) on Pd@Pt-in-Au (100) surface with a single-atom Pt (Pt1).

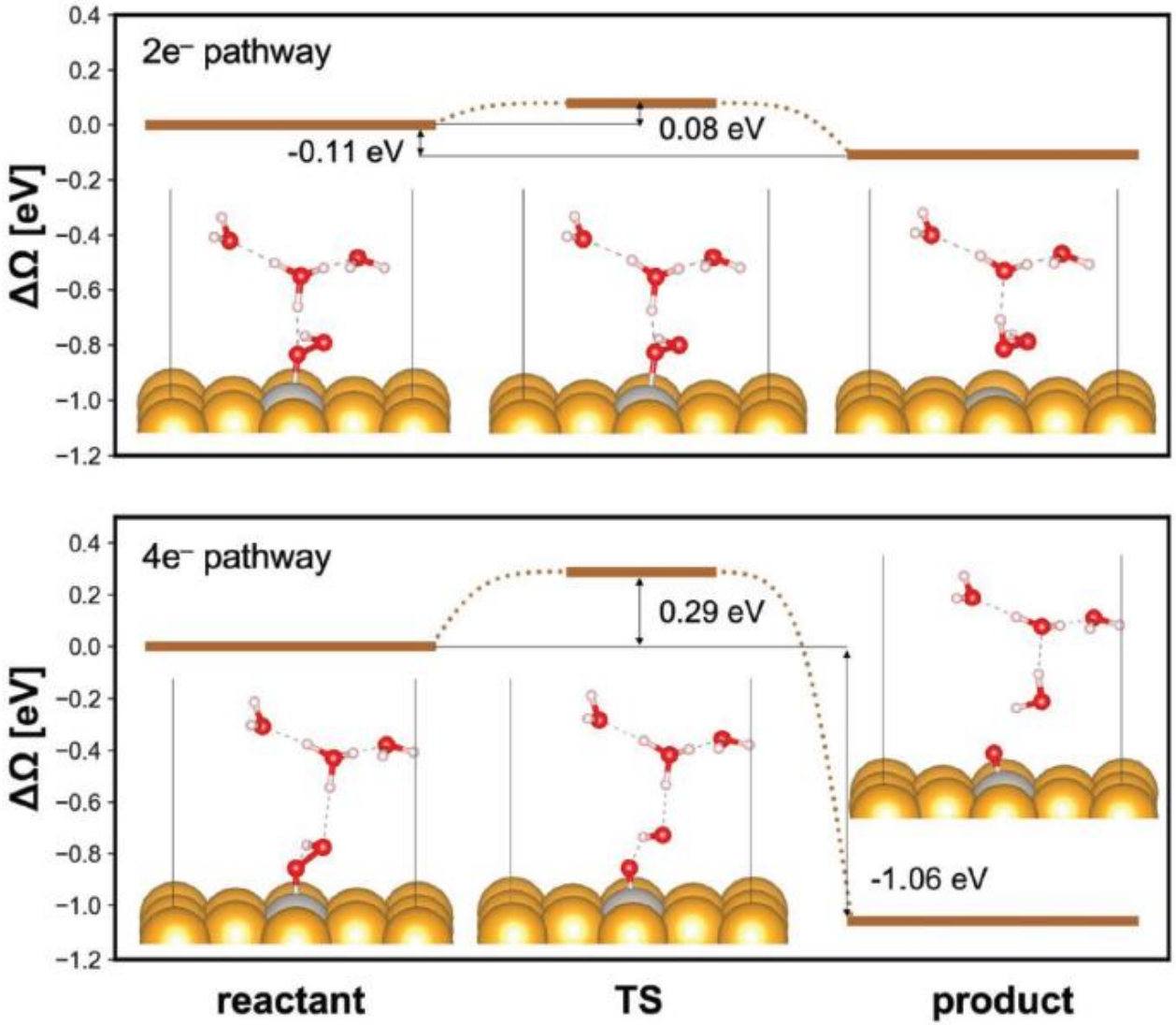

Adv. Funct. Mater., **2024**, *23*, 14281.

Heterogeneous Interfaces of Ni_3Se_4 Nanoclusters Decorated on Ni_3N Surface Enhance Efficient and Durable Hydrogen Evolution Reactions in Alkaline Electrolyte

Prof. Wei-Nien Su,

Prof. Bing-Joe Hwang, NTUST

Color	GREY HYDROGEN	BLUE HYDROGEN	TURQUOISE HYDROGEN*	GREEN HYDROGEN
Process	SMR or gasification	SMR or gasification with carbon capture (85-95%)	Pyrolysis	Electrolysis
Source	Methane or coal	Methane or coal	Methane	Renewable electricity

Note: SMR = steam methane reforming.
** Turquoise hydrogen is an emerging decarbonisation option.*

Source: International Renewable Energy Agency

HER Reaction Pathway

Acid Electrolyte:

Volmer step : $H^+ + e^- \rightarrow H^*$ ----(1)

Heyrovsky step: $H^* + H^+ + e^- \rightarrow H_2$ ----(2)

Tafel step : $H^* + H^* \rightarrow H_2$ ----(3)

Alkaline Electrolyte:

Volmer step : $H_2O + e^- \rightarrow H^* + OH^-$ ----(1)

Heyrovsky step: $H_2O + e^- + H^* \rightarrow H_2 + OH^-$ ----(2)

Tafel step : $H^* + H^* \rightarrow H_2$ ----(3)

Hydrogen evolution reaction (HER) volcano plot on metal electrodes under low pH environment.

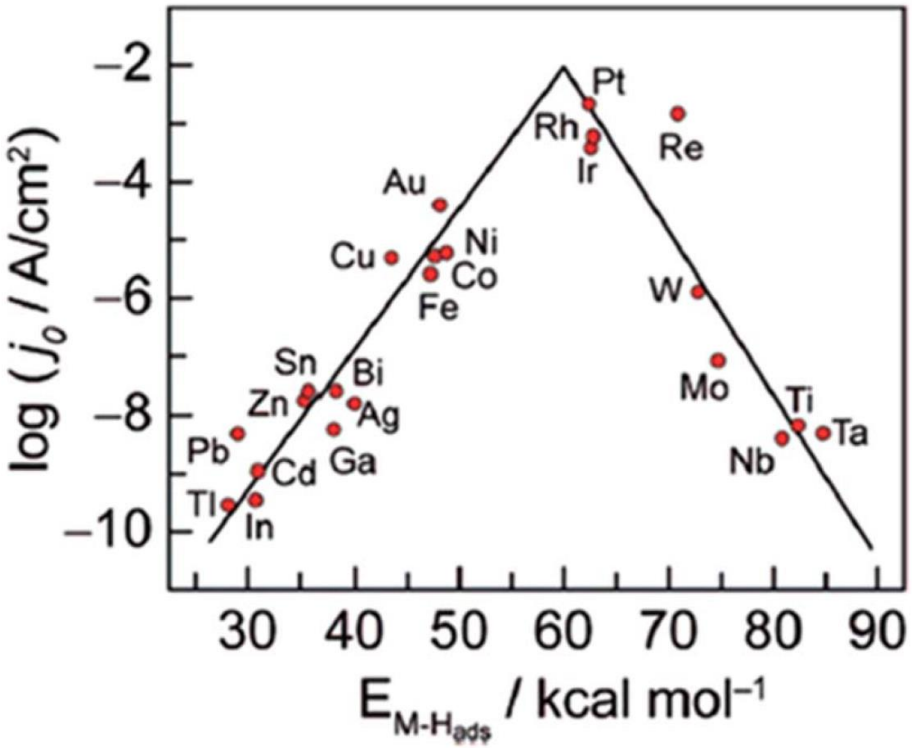

RSC Adv., **2023**, *13*, 3843–3876.

From Single Metal to Heterostructure Electrocatalysts

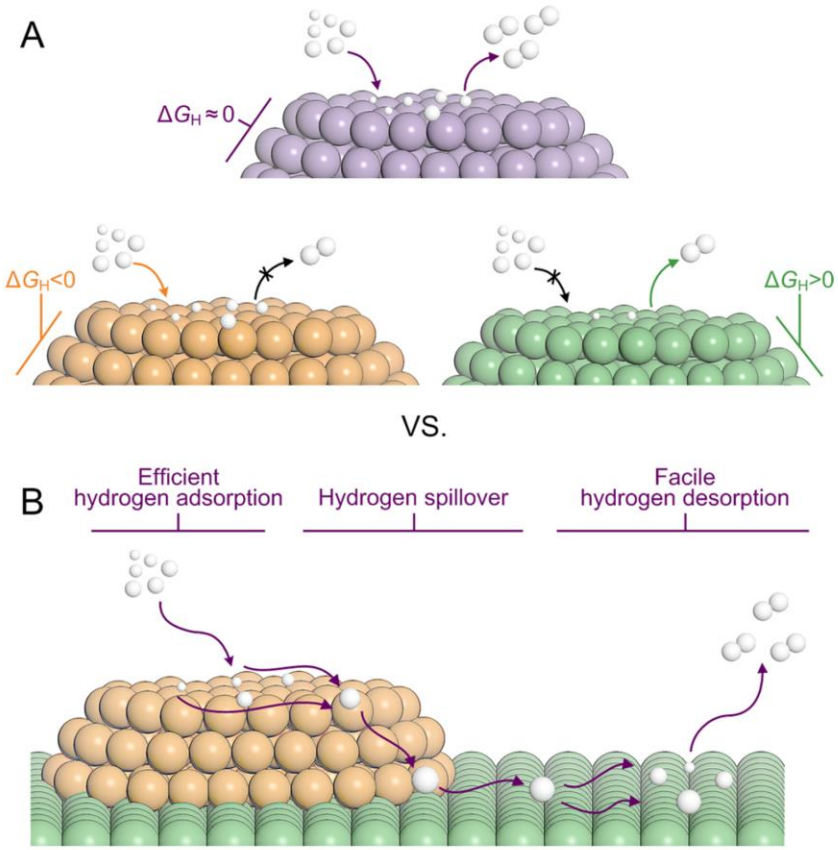

(A) The state-of-the-art design concept for HER electrocatalysts is based on ΔG_H. (B) The design of HER electrocatalysts based on hydrogen spillover effects.

Acc. Chem. Res. **2024**, *57*, 895−904.

Synthesis of Ni_3Se_4-Ni_3N electrocatalyst

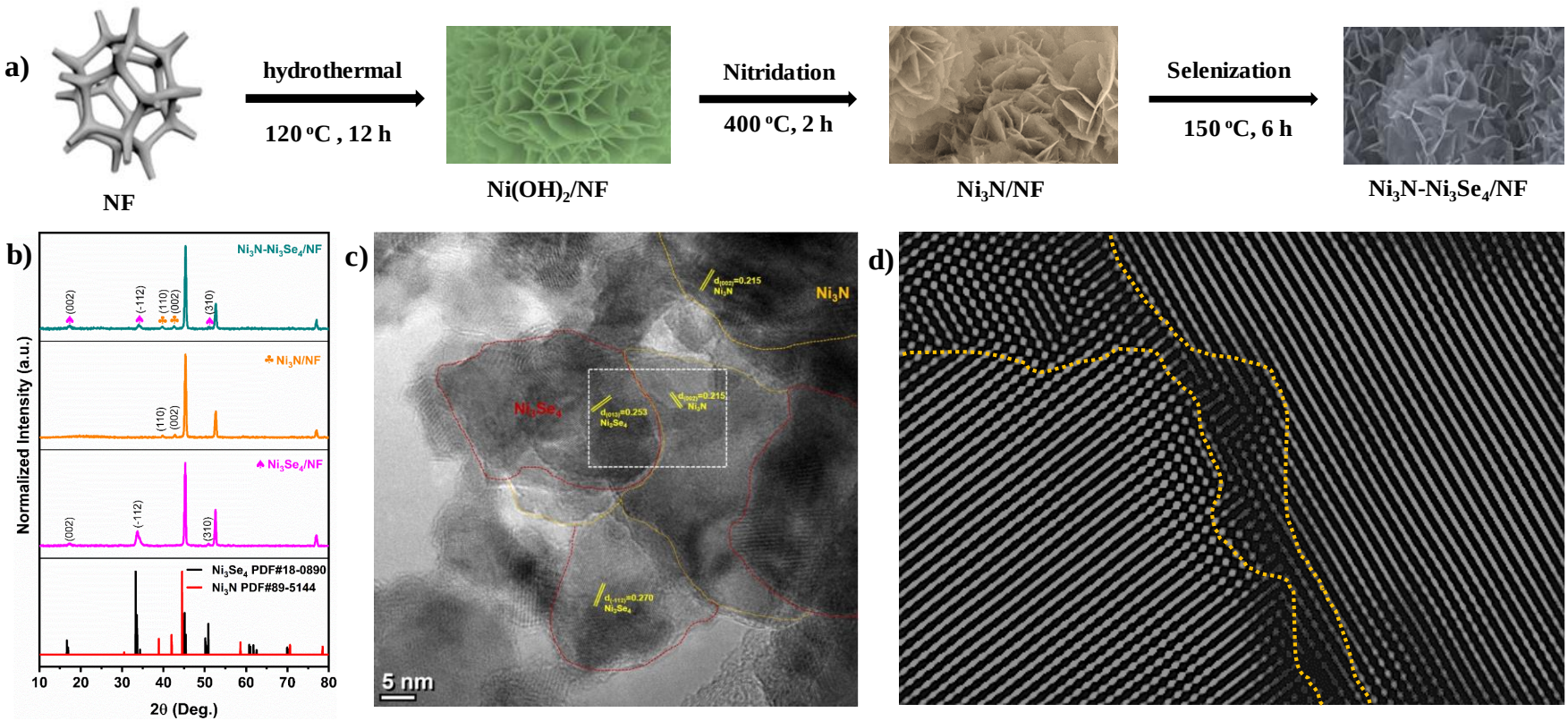

X-ray Photoelectron Spectroscopy Characterization.

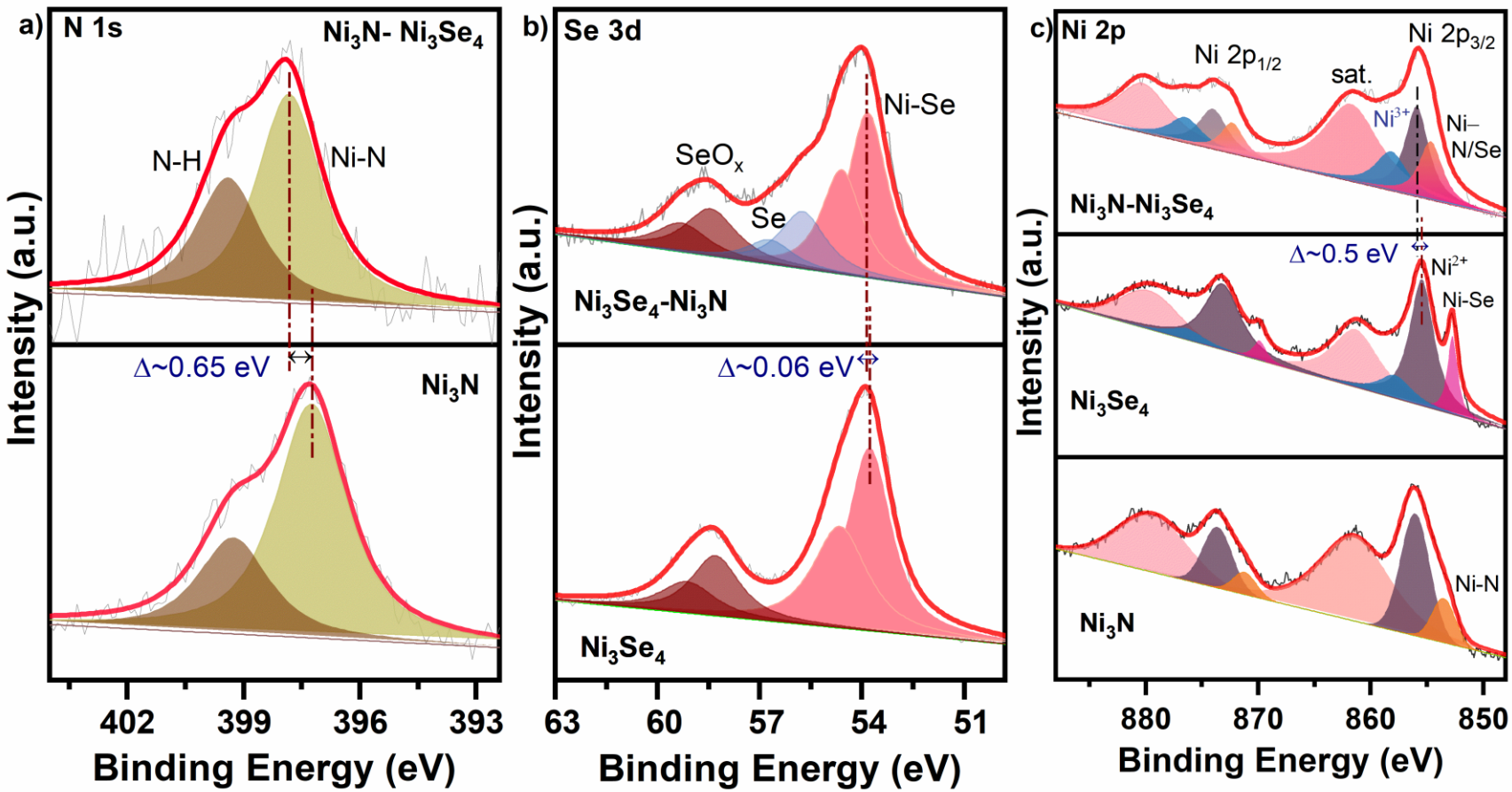

Electrochemical Performance of as-prepared Electrocatalysts

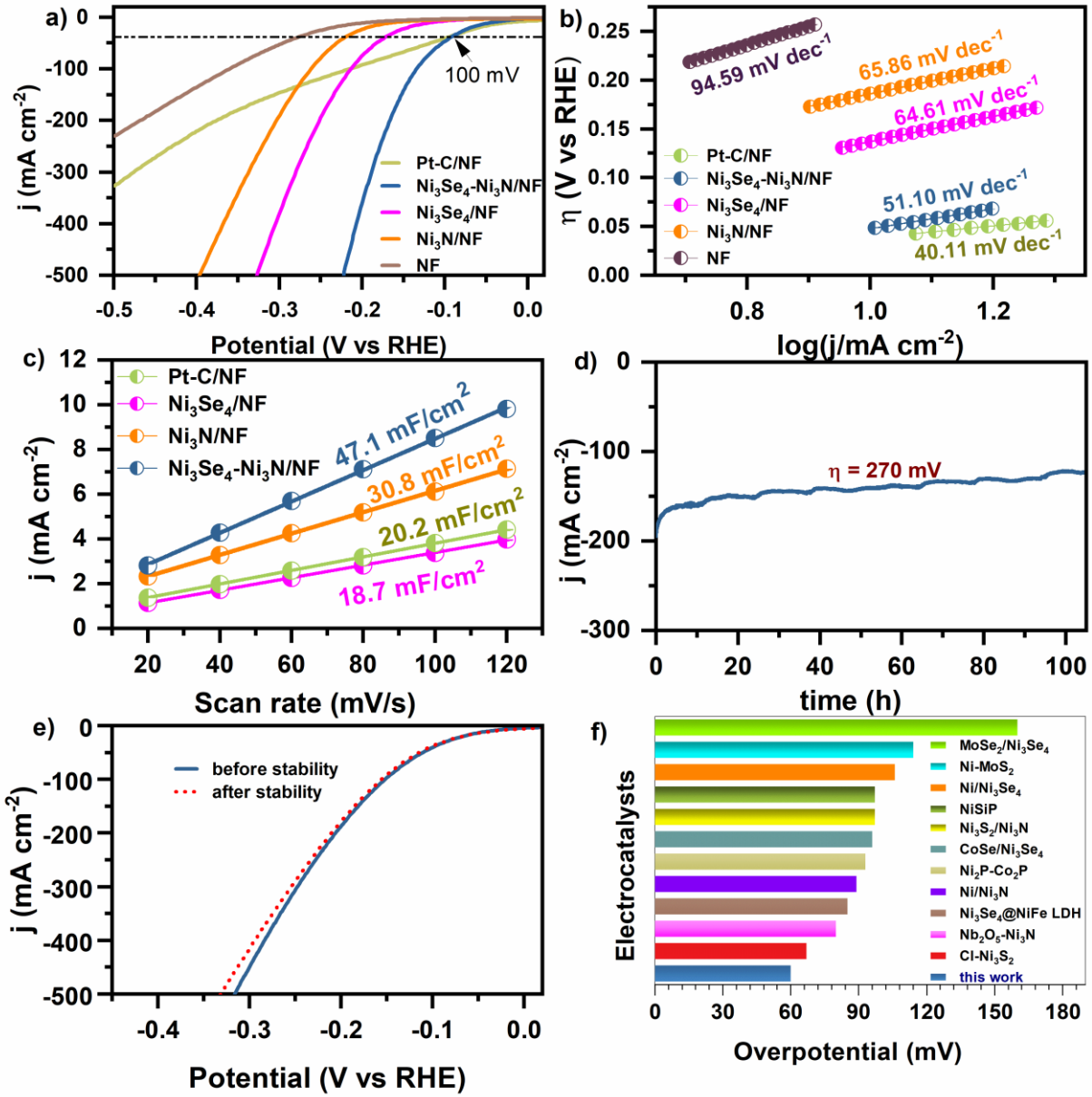

Ni_3Se_4-Ni_3N (η_{10} =60 mV)
Ni_3Se_4 (η_{10} =110 mV)
Ni_3N (η_{10} =130 mV).
Pt-C (η10 = 42 mV)

Water adsorption characterizations using NAPXPS

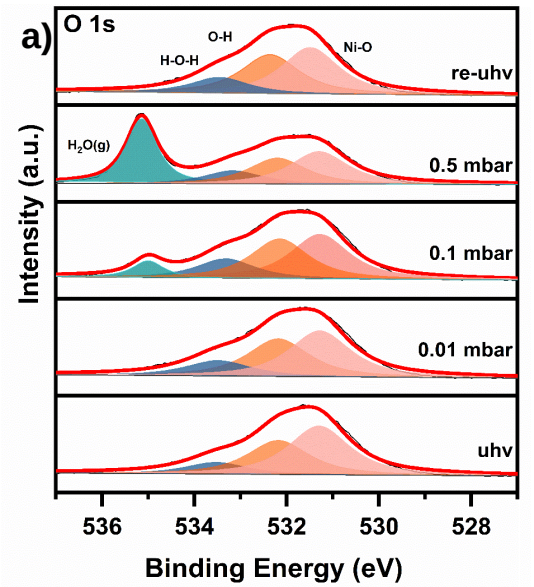

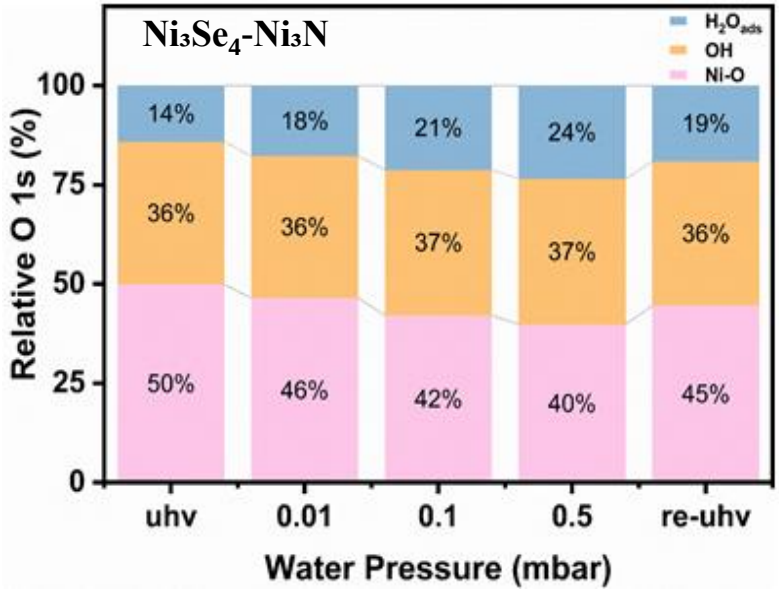

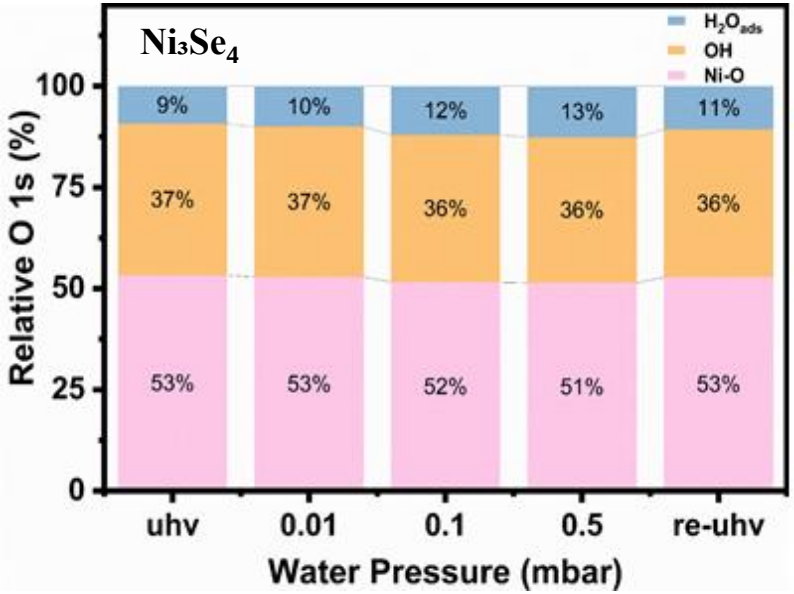

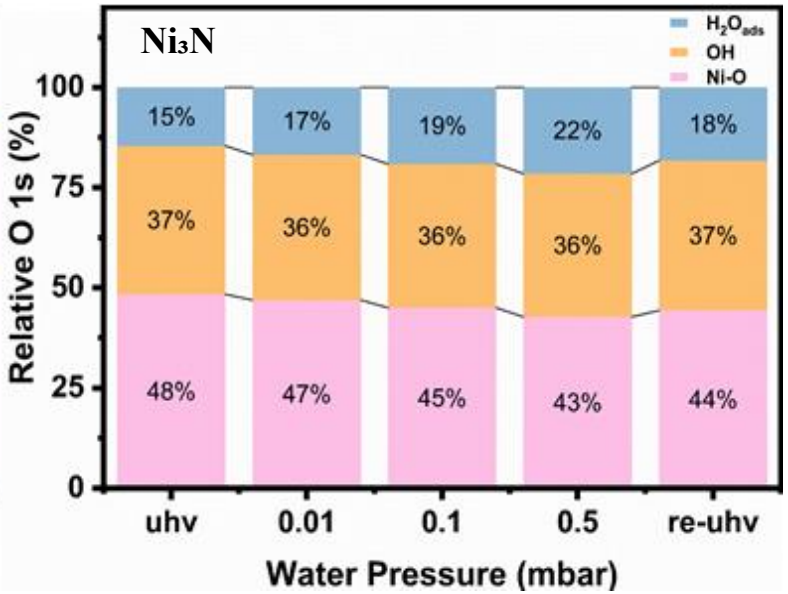

Water adsorption characterizations using NAPXPS

Ni_3Se_4-Ni_3N

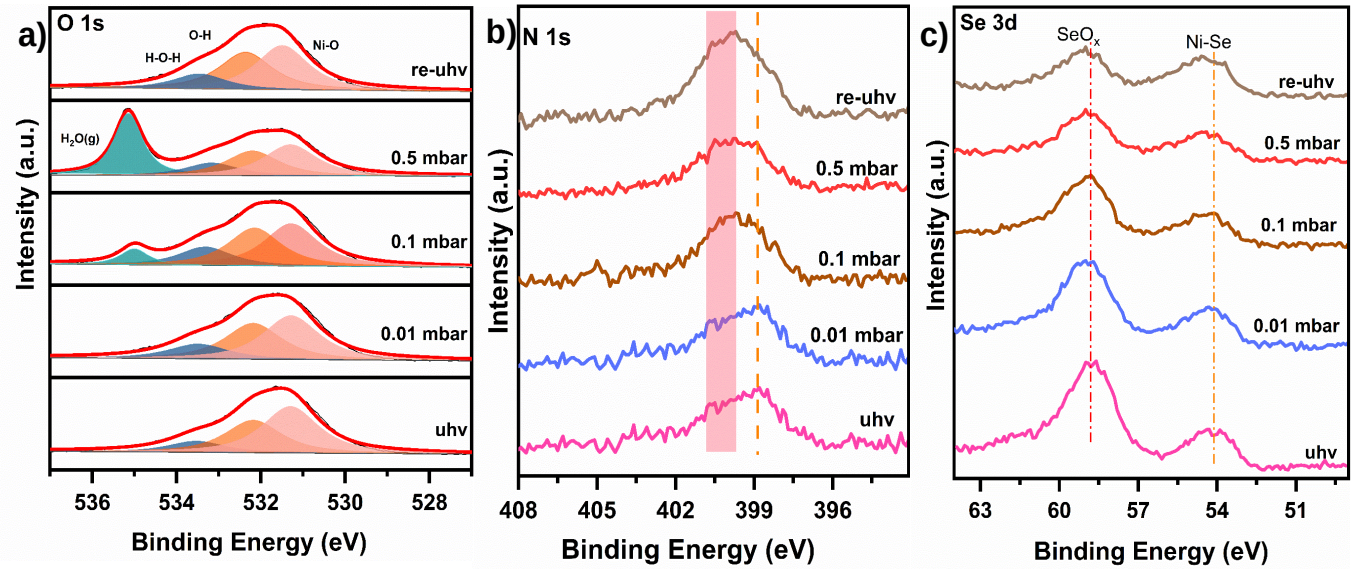

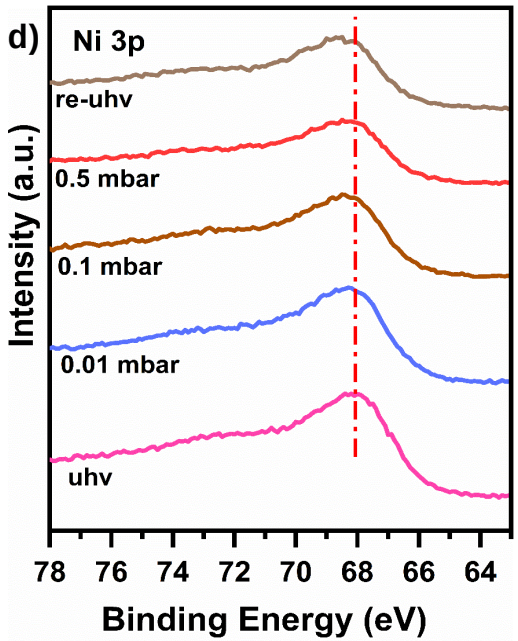

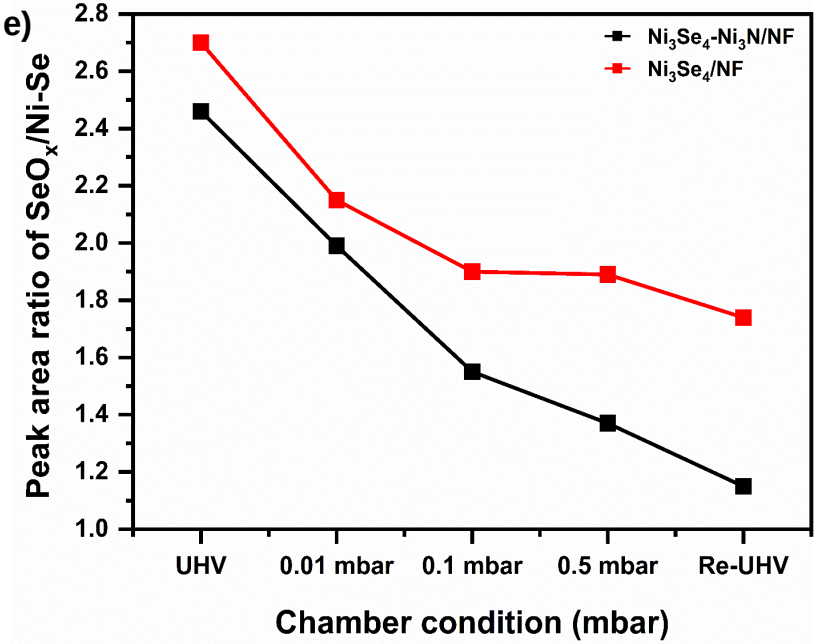

In-situ APXPS characterization under different applied potentials

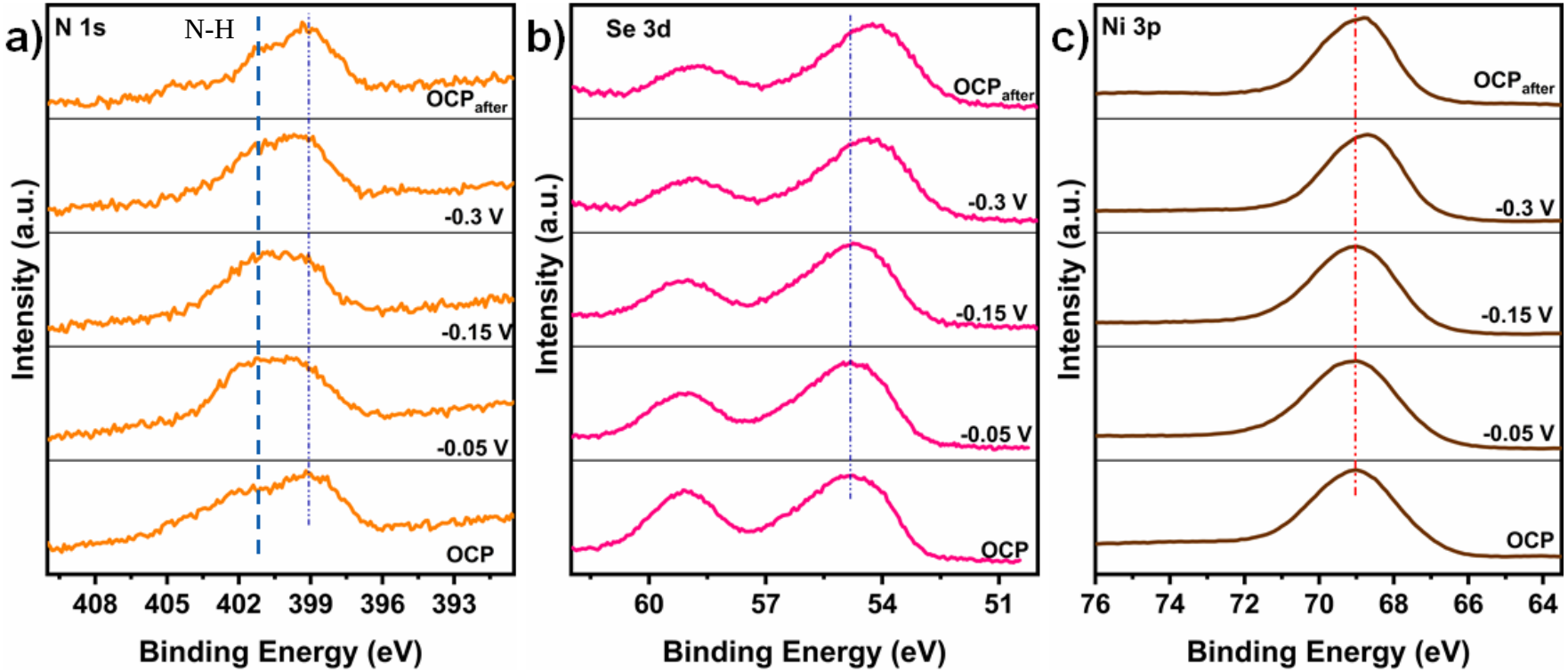

Kinetic Isotope Effects

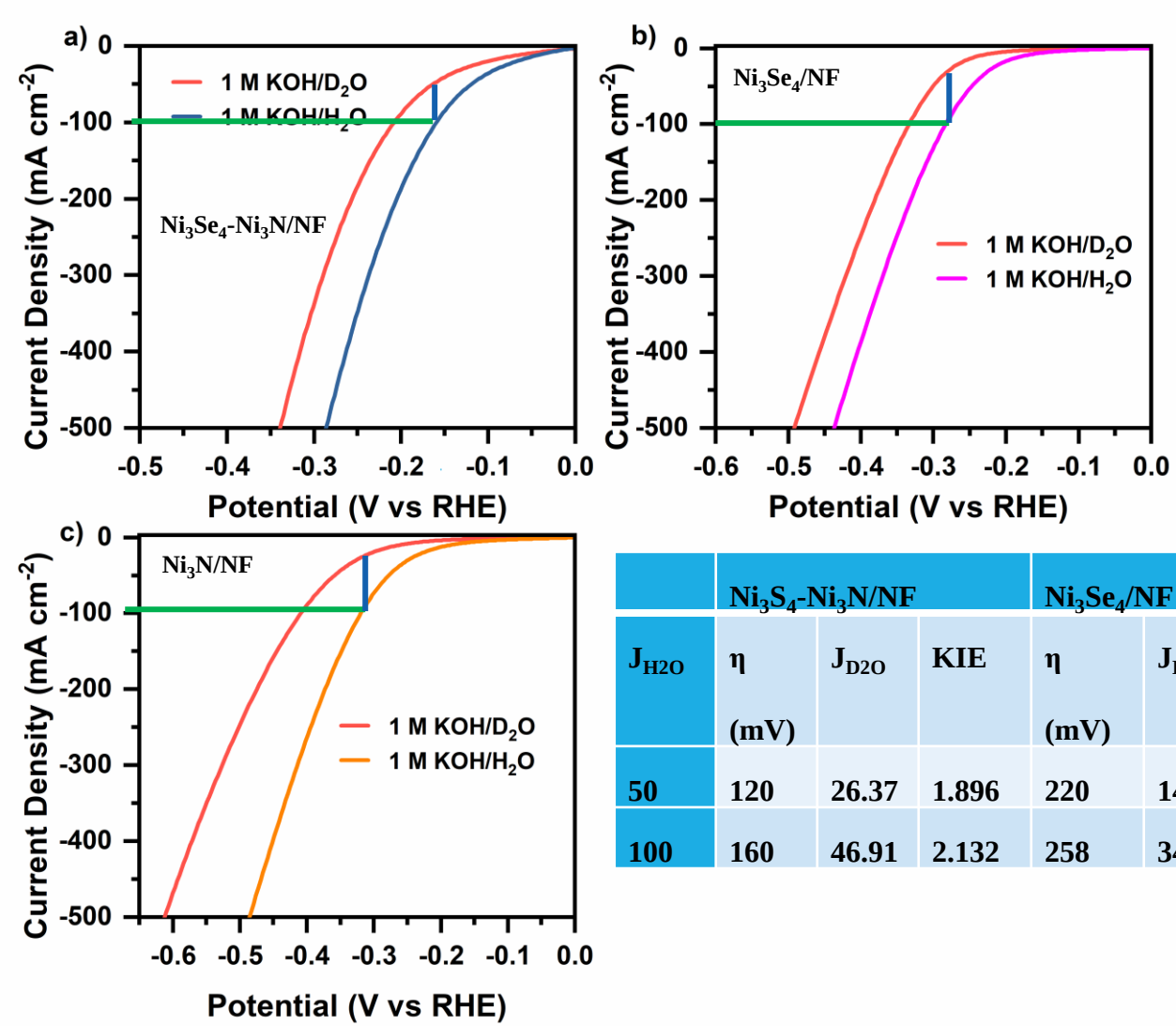

	Ni_3S_4-Ni_3N/NF			Ni_3Se_4/NF			Ni_3/NF		
J_{H2O}	η (mV)	J_{D2O}	KIE	η (mV)	J_{D2O}	KIE	η (mV)	J_{D2O}	KIE
50	120	26.37	1.896	220	14.30	3.495	270	14.27	3.496
100	160	46.91	2.132	258	34.68	2.890	319	25.49	3.922

The schematic diagram for the proposed HER mechanism on Ni_3Se_4-Ni_3N/NF electrocatalysts.

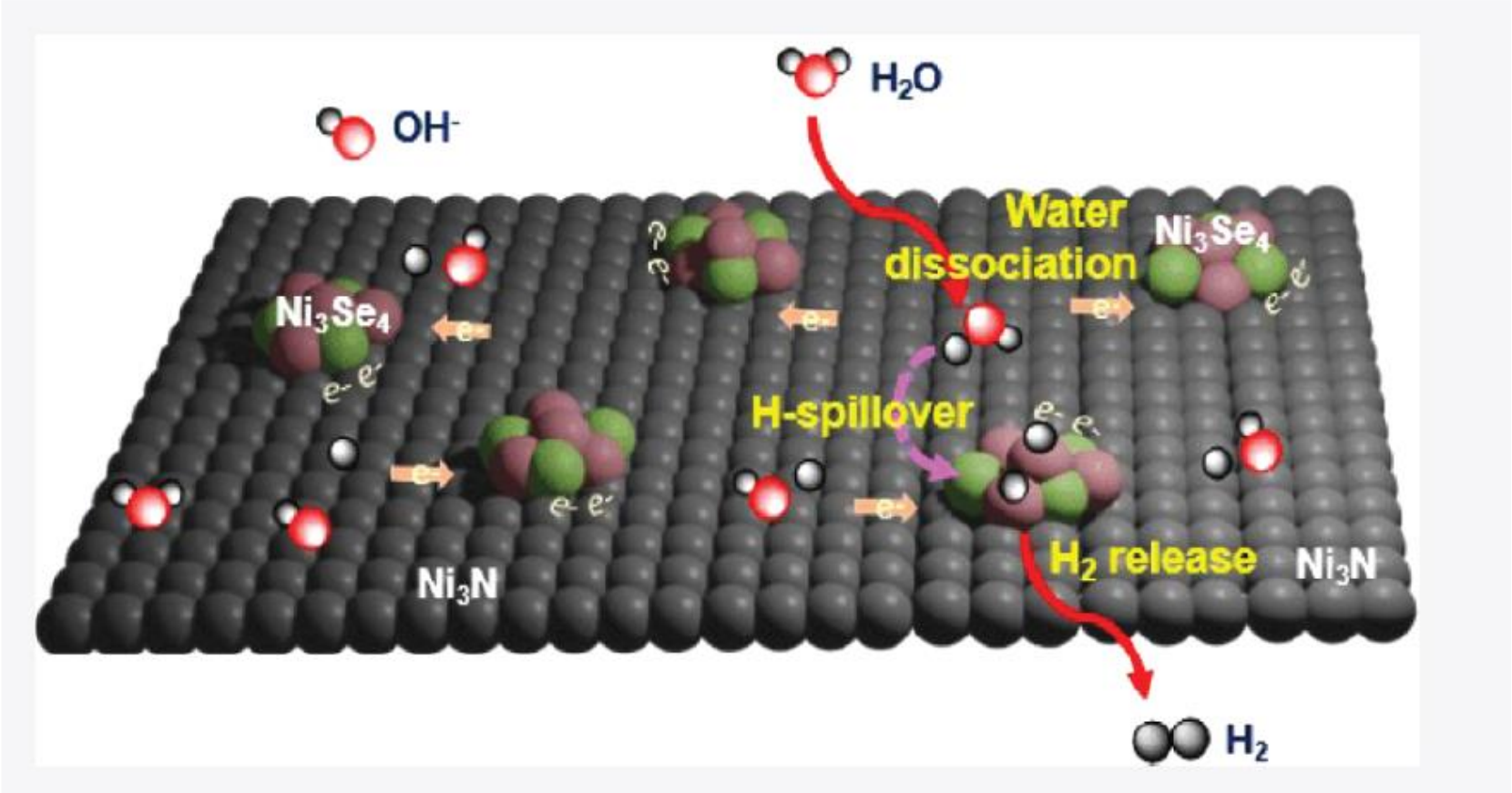

J. Am. Chem. Soc. **2025**, *147*, 16047−16059

Selected Scientific Results at TLS BL 24A

ChemComm

COMMUNICATION

View Article Online
View Journal | View Issue

Check for updates

Cite this: *Chem. Commun.*, 2019, 55, 6946

Received 21st January 2019, Accepted 15th May 2019

DOI: 10.1039/c9cc00518h

Anhydrous amorphous calcium carbonate (ACC) is structurally different from the transient phase of biogenic ACC†

Chieh Tsao,[a] Pao-Tao Yu,[a] Chin-Hsuan Lo,[a] Chung-Kai Chang,[b] Chia-Hsin Wang,*[b] Yaw-Wen Yang *[bc] and Jerry Chun Chung Chan *[a]

2019, *55*, 6946.

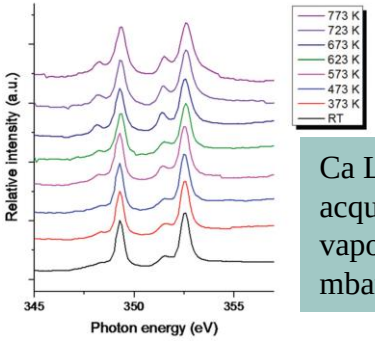

Ca L edge of ACC acquired at a water vapor pressure of 0.4 mbar.

Constant flow electrochemical cell system

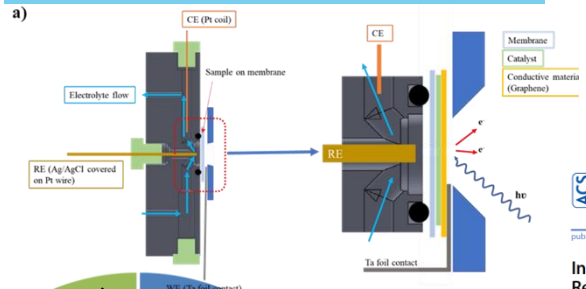

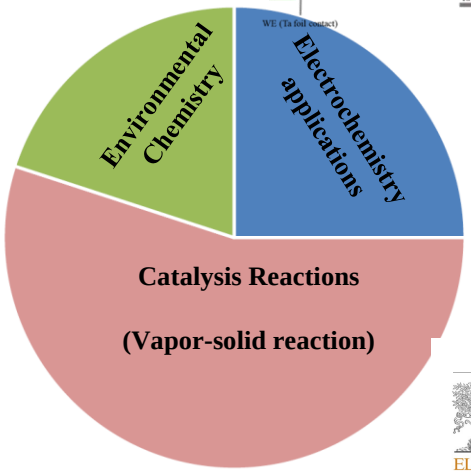

nature communications

Article

https://doi.org/10.1038/s41467-022-33150-x

Interface engineering breaks both stability and activity limits of RuO_2 for sustainable water oxidation

2022, *13*, 5488.

Received: 27 February 2022

Accepted: 6 September 2022

Published online: 16 September 2022

Kun Du[1,6], Lifu Zhang[2,6], Jieqiong Shan[3], Jiaxin Guo[1], Jing Mao[1], Chueh-Cheng Yang[4,5], Chia-Hsin Wang[4,6], Zhenpeng Hu[2] & Tao Ling[1]

ACS Catalysis

2023, *13*, 13434.

pubs.acs.org/acscatalysis

Research Article

Investigation of Zn-Substituted $FeCo_2O_4$ for the Oxygen Evolution Reaction and Reaction Mechanism Monitoring through *In Situ* Near-Ambient-Pressure X-ray Photoelectron Spectroscopy

Pongsatorn Patta, Ya-Yu Chen, Manjula Natesan, Chien-Lin Sung, Chueh-Cheng Yang, Chia-Hsin Wang,* Tsuyohiko Fujigaya,* and Yu-Hsu Chang*

Decreasing the O_2-to-H_2O_2 Kinetic Energy Barrier on Dilute Binary Alloy Surfaces with Controlled Configurations of Isolated Active Atoms

Adv. Funct. Mater., **2024**, *23*, 14281.

Shang-Cheng Lin, Chun-Wei Chang, Meng-Hsuan Tsai, Chih-Hao Chen, Jui-Tai Lin, Chia-Ying Wu, I-Ting Kao, Wen-Yang Jao, Chia-Hsin Wang, Wen-Yueh Yu, Chi-Chang Hu, Kun-Han Lin, and Tung-Han Yang**

Journal of Materials Chemistry A

ROYAL SOCIETY OF CHEMISTRY

PAPER

View Article Online
View Journal | View Issue

Check for updates

Cite this: *J. Mater. Chem. A*, 2020, 8, 12744

Local synergetic collaboration between Pd and local tetrahedral symmetric Ni oxide enables ultra-high-performance CO_2 thermal methanation†

Che Yan,[a] Chia-Hsin Wang,*[b] Moore Lin,[c] Dinesh Bhalothia,[a] Shou-Shiun Yang,[a] Gang-Jei Fan,[c] Jia-Lin Wang,[c] Ting-Shan Chan,[b] Yao-lin Wang,[d] Xin Tu,[d] Sheng Dai,[e] Kuan-Wen Wang,[f] Jr-Hau He[g] and Tsan-Yao Chen *[ahi]

2020, *8*, 12744.

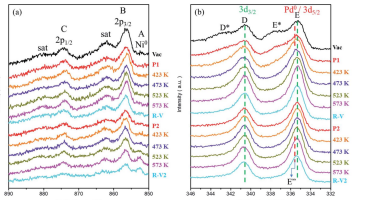

Fig. 5 In situ ambient-pressure X-ray photoelectron spectroscopy (APXPS) spectra of NiO-Pd-T in the (a) Ni 2p and (b) Pd 3d regions. The spectra are measured starting from under vacuum (Vac) to an atmosphere of CO_2 at 0.11 mbar at room temperature (P1) and then with the temperature increasing up to 573 K. After that, the chamber was placed under vacuum and allowed to cool to room temperature (R-V), then purged using a reaction gas of CO_2 and H_2 with a ratio of 1 : 3 for CO_2: H_2 (P2) and heated from 423 to 573 K.

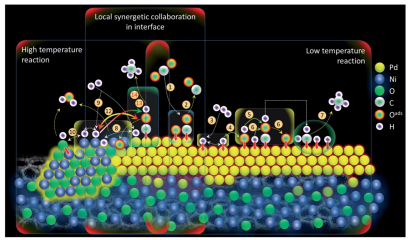

Scheme 1 Schematic representation of the reaction coordinates in the NiO_1Pd-T.

Nano Energy 83 (2021) 105830

Contents lists available at ScienceDirect

Nano Energy

journal homepage: http://www.elsevier.com/locate/nanoen

ELSEVIER

Electrochemical reduction of CO_2 in ionic liquid: Mechanistic study of Li–CO_2 batteries via *in situ* ambient pressure X-ray photoelectron spectroscopy

2021, *83*, 105830.

Yu Wang [a], Wanwan Wang [a], Jing Xie [a], Chia-Hsin Wang [b], Yaw-Wen Yang [b], Yi-Chun Lu [a,*]

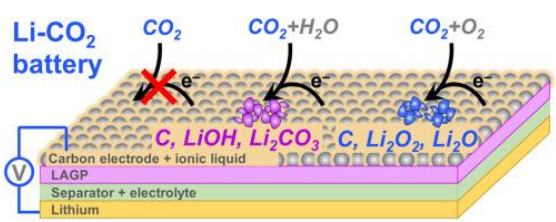

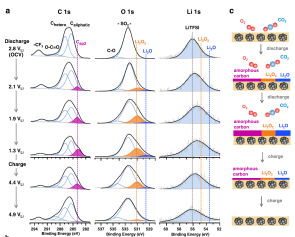

Selected Publications by using APXPS at TLS BL 24A

New ambient pressure X-ray photoelectron spectroscopy endstation at Taiwan light source

Cite as: AIP Conference Proceedings **2054**, 040012 (2019); https://doi.org/10.1063/1.5084613
Published Online: 16 January 2019

Chia-Hsin Wang, Sun-Tang Chang, Sheng-Yuan Chen, and Yaw-Wen Yang

ChemComm 台大化學陳振中教授

COMMUNICATION

View Article Online

Check for updates

Anhydrous amorphous calcium carbonate (ACC) is structurally different from the transient phase of biogenic ACC†

Cite this: *Chem. Commun.*, 2019, 55, 6946

Received 21st January 2019, Accepted 15th May 2019

DOI: 10.1039/c9cc00518h

Chieh Tsao,[a] Pao-Tao Yu,[a] Chin-Hsuan Lo,[a] Chung-Kai Chang,[b] Chia-Hsin Wang,*[b] Yaw-Wen Yang *[bc] and Jerry Chun Chung Chan *[a]

XAS

Nano Energy 67 (2020) 104163

Contents lists available at ScienceDirect

Nano Energy

journal homepage: http://www.elsevier.com/locate/nanoen

2020, *67*, *104163*.

Full paper

Identification of dual-active sites in cobalt phthalocyanine for electrochemical carbon dioxide reduction

Yujian Xia[a], Stepan Kashtanov[b], Pengfei Yu[c], Lo-Yueh Chang[a,**], Kun Feng[a], Jun Zhong[a], Jinghua Guo[d], Xuhui Sun[a,*]

Journal of Materials Chemistry A

ROYAL SOCIETY OF CHEMISTRY

PAPER **Cited: 26**

View Article Online

Check for updates

Local synergetic collaboration between Pd and local tetrahedral symmetric Ni oxide enables ultra-high-performance CO_2 thermal methanation†

Cite this: *J. Mater. Chem. A*, 2020, 8, 12744

Che Yan,[a] Chia-Hsin Wang,*[b] Moore Lin,[c] Dinesh Bhalothia,[a] Shou-Shiun Yang,[a] Gang-Jei Fan,[c] Jia-Lin Wang,[c] Ting-Shan Chan,[b] Yao-lin Wang,[d] Xin Tu,[d] Sheng Dai,[e] Kuan-Wen Wang,[f] Jr-Hau He[g] and Tsan-Yao Chen[a]*

ARTICLE

https://doi.org/10.1038/s41467-021-21956-0 OPEN

Rational strain engineering of single-atom ruthenium on nanoporous MoS_2 for highly efficient hydrogen evolution

Nature Comm.. **2021**, *12*, 1687.

Kang Jiang[1], Min Luo[2], Zhixiao Liu[1], Ming Peng[1], Dechao Chen[1], Ying-Rui Lu[3], Ting-Shan Chan[3], Frank M. F. de Groot[4] & Yongwen Tan[1]

Contents lists available at ScienceDirect

Nano Energy

journal homepage: http://www.elsevier.com/locate/nanoen

Electrochemical reduction of CO_2 in ionic liquid: Mechanistic study of Li–CO_2 batteries via *in situ* ambient pressure X-ray photoelectron spectroscopy

2021, *83*, 105830.

Yu Wang[a], Wanwan Wang[a], Jing Xie[a], Chia-Hsin Wang[b], Yaw-Wen Yang[b], Yi-Chun Lu[a,*]

nature materials **2022**, *21*, 681.

ARTICLES https://doi.org/10.1038/s41563-022-01252-y

Check for updates

A single-atom library for guided monometallic and concentration-complex multimetallic designs

Lili Han[1,11], Hao Cheng[1,11], Wei Liu[2,11], Haoqiang Li[2], Pengfei Ou[3], Ruoqian Lin[4], Hsiao-Tsu Wang[5], Chih-Wen Pao[6], Ashley R. Head[4], Chia-Hsin Wang[6], Xiao Tong[4], Cheng-Jun Sun[7], Way-Faung Pong[5], Jun Luo[2,8], Jin-Cheng Zheng[9,10] and Huolin L. Xin[1]

XAS

Hydrogen Spillover and Storage on Graphene with Single-Site Ti Catalysts

Jhih-Wei Chen,[⊥] Shang-Hsien Hsieh,[⊥] Sheng-Shong Wong,[⊥] Ya-Chi Chiu, Hung-Wei Shiu, Chia-Hsin Wang, Yaw-Wen Yang, Yao-Jane Hsu, Domenica Convertino, Camilla Coletti, Stefan Heun, Chia-Hao Chen,* and Chung-Lin Wu*

ACS Energy Letters **2022**, *7*, 2297.

RESEARCH ARTICLE

ADVANCED FUNCTIONAL MATERIALS www.afm-journal.de

Complementary Metal–Oxide–Semiconductor Compatible 2D Layered Film-Based Gas Sensors by Floating-Gate Coupling Effect

Adv. Funct. Mater. **2022**, *32*, 2108878

Po-Hung Tan, Che-Hao Hsu, Ying-Chun Shen, Chien-Ping Wang, Kun-Lin Liou, Jiaw-Ren Shih, Chrong Jung Lin, Ling Lee, Kuangye Wang, Hong-Min Wu, Tsung-Yu Chiang, Yue-Der Chih, Jonathan Chang, Ya-Chin King, and Yu-Lun Chueh**

nature communications

2022, *13*, 5488.

Article https://doi.org/10.1038/s41467-022-33150-x

Interface engineering breaks both stability and activity limits of RuO_2 for sustainable water oxidation

Received: 27 February 2022
Accepted: 6 September 2022
Published online: 16 September 2022

Kun Du[1,6], Lifu Zhang[2,6], Jieqiong Shan[3], Jiaxin Guo[1], Jing Mao[1], Chueh-Cheng Yang[4,5], Chia-Hsin Wang[4,6], Zhenpeng Hu[2] & Tao Ling[1]

Revealing the Surface Species Evolution on Low-loading Platinum in an Electrochemical Redox Reaction by Operando Ambient-Pressure X-ray Photoelectron Spectroscopy

Chueh-Cheng Yang,[a] Meng-Hsuan Tsai,[b] Zong-Ren Yang,[b] Yuan-Chieh Tseng,*[a] and Chia-Hsin Wang*[b]

ACS Catalysis

ChemCatChem, **2023**, *15*, e202300359

pubs.acs.org/acscatalysis Research Article

2023, *13*, 13434.

Investigation of Zn-Substituted $FeCo_2O_4$ for the Oxygen Evolution Reaction and Reaction Mechanism Monitoring through *In Situ* Near-Ambient-Pressure X-ray Photoelectron Spectroscopy

Pongsatorn Patta, Ya-Yu Chen, Manjula Natesan, Chien-Lin Sung, Chueh-Cheng Yang, Chia-Hsin Wang,* Tsuyohiko Fujigaya,* and Yu-Hsu Chang*

Article https://doi.org/10.1038/s41467-024-44840-z

Investigating the role of undercoordinated Pt sites at the surface of layered $PtTe_2$ for methanol decomposition

Nature Comm. **2024**, *15*, 653.

Received: 23 May 2023
Accepted: 8 January 2024
Published online: 22 January 2024

Jing-Wen Hsueh[1], Lai-Hsiang Kuo[1], Po-Han Chen[2], Wan-Hsin Chen[3], Chi-Yao Chuang[3], Chia-Nung Kuo[4,5], Chin-Shan Lue[4,5,6], Yu-Ling Lai[7], Bo-Hong Liu[7], Chia-Hsin Wang[7], Yao-Jane Hsu[7], Chun-Liang Lin[3], Jyh-Pin Chou[8] & Meng-Fan Luo[1]

RESEARCH ARTICLE

ADVANCED FUNCTIONAL MATERIALS www.afm-journal.de

Decreasing the O_2-to-H_2O_2 Kinetic Energy Barrier on Dilute Binary Alloy Surfaces with Controlled Configurations of Isolated Active Atoms

Adv. Funct. Mater. **2024**, *23*, 14281.

Shang-Cheng Lin, Chun-Wei Chang, Meng-Hsuan Tsai, Chih-Hao Chen, Jui-Tai Lin, Chia-Ying Wu, I-Ting Kao, Wen-Yang Jao, Chia-Hsin Wang, Wen-Yueh Yu, Chi-Chang Hu, Kun-Han Lin, and Tung-Han Yang**

Ammonia synthesis over cesium-promoted mesoporous-carbon-supported ruthenium catalysts: Impact of graphitization degree of the carbon support

清大化學楊家銘教授

Shih-Yuan Chen[a], Li-Yu Wang[b‡], Kai-Chun Chen[b‡], Cheng-Hsi Yeh[c‡], Wei-Chih Hsiao[b‡], Hsin-Yu Chen[d], Masayasu Nishi[a], Martin Keller[e], Chih-Li Chang[f], Chien-Neng Liao[d], Takehisa Mochizuki[a], Hsin-Yi Tiffany Chen[c d ii], Ho-Hsiu Chou[f], Chia-Min Yang[b g]

Appl. Catal. B: Environ. **2024**, *346*, 123725.

Research papers

***In situ* ambient pressure x-ray photoelectron spectroscopy study on O_2/H_2O-assisted Na–CO_2 batteries**

J. Energy. Storage **2024**, *100*, 113467.

Kevin Iputera[a‡], Chia-Hui Yi[a‡], Jheng-Yi Huang[a], Masanobu Nakayama[b], Bo-Hong Liu[c], Chia-Hsin Wang[c], Yaw-Wen Yang[c], Ru-Shi Liu[a e]

台大化學劉如熹教授

Enhanced CO_2 photoreduction to CH_4 via *COOH and *CHO intermediates stabilization by synergistic effect of implanted P and S vacancy in thin-film SnS_2

Nano Energy **2024**, *128*, 109863.

Tadios Tesfaye Mamo[a,b,c,d], Mohammad Qorbani[e,f,*], Adane Gebresilassie Hailemariam[b,g,h,i,j], Raghunath Putikam[b], Che-Men Chu[k], Ting-Rong Ko[e,f], Amr Sabbah[e,f,l], Chih-Yang Huang[e,m,n], Septia Kholimatussadiah[b,c,e,o], Tadesse Billo[p], Mahmoud Kamal Hussien[e,q], Shuo-Yun Chang[e,r], Ming-Chang Lin[b], Wei-Yen Woon[k], Heng-Liang Wu[a,e,f,s,**], Ken-Tsung Wong[a,b], Li-Chyong Chen[e,f,e,*], Kuei-Hsien Chen[b,e,***]

JACS JOURNAL OF THE AMERICAN CHEMICAL SOCIETY

Open Access

This article is licensed under CC-BY 4.0

pubs.acs.org/JACS Article

Heterogeneous Interfaces of Ni_3Se_4 Nanoclusters Decorated on a Ni_3N Surface Enhance Efficient and Durable Hydrogen Evolution Reactions in Alkaline Electrolyte

Dessalew Dagnew Alemayehu, Meng-Che Tsai,* Meng-Hsuan Tsai, Chueh-Cheng Yang, Chun-Chi Chang, Chia-Yu Chang, Endalkachew Asefa Moges, Keseven Lakshmanan, Yosef Nikodimos, Wei-Nien Su,* Chia-Hsin Wang,* and Bing Joe Hwang*

2025.06 updated

Future plan of APXPS end station at NSRRC

APXPS end- station at BL 24A of TLS will relocate to soft x-ray spectroscopy beamline at TPS 43A.

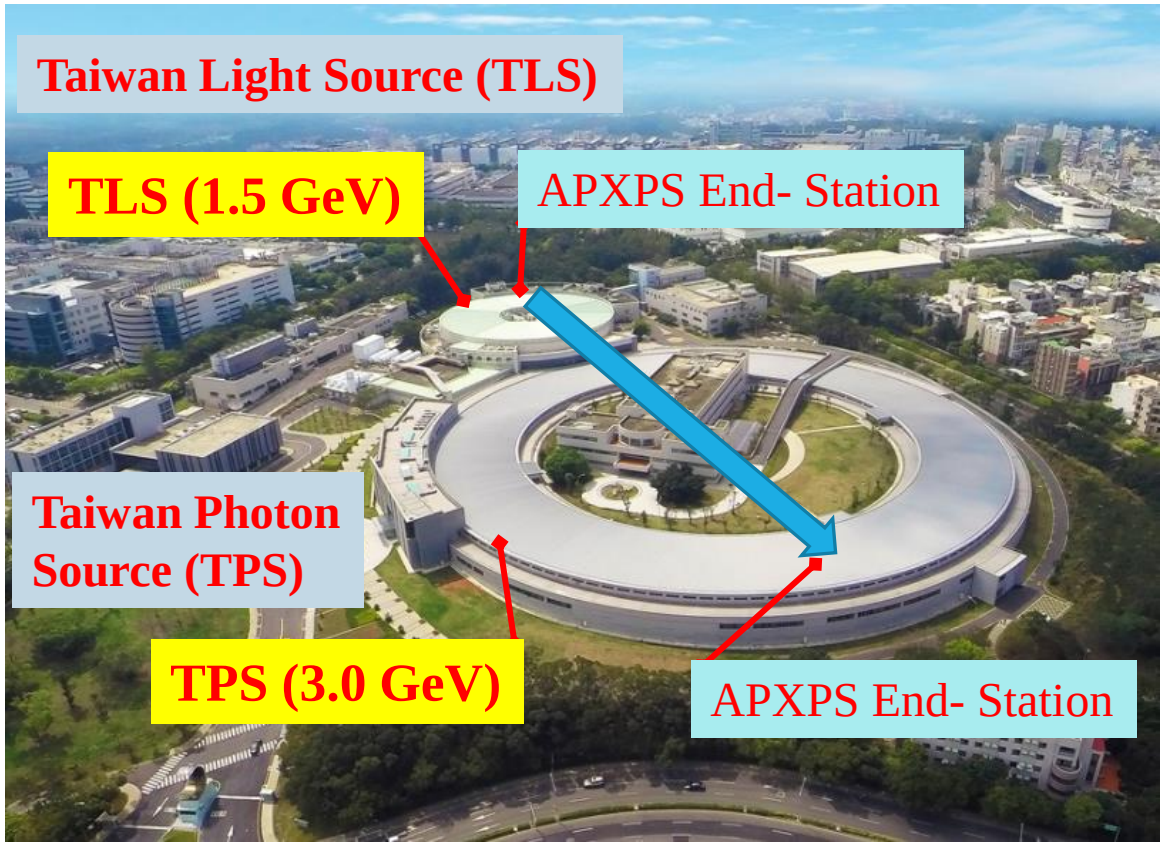

TPS 43A Beamline

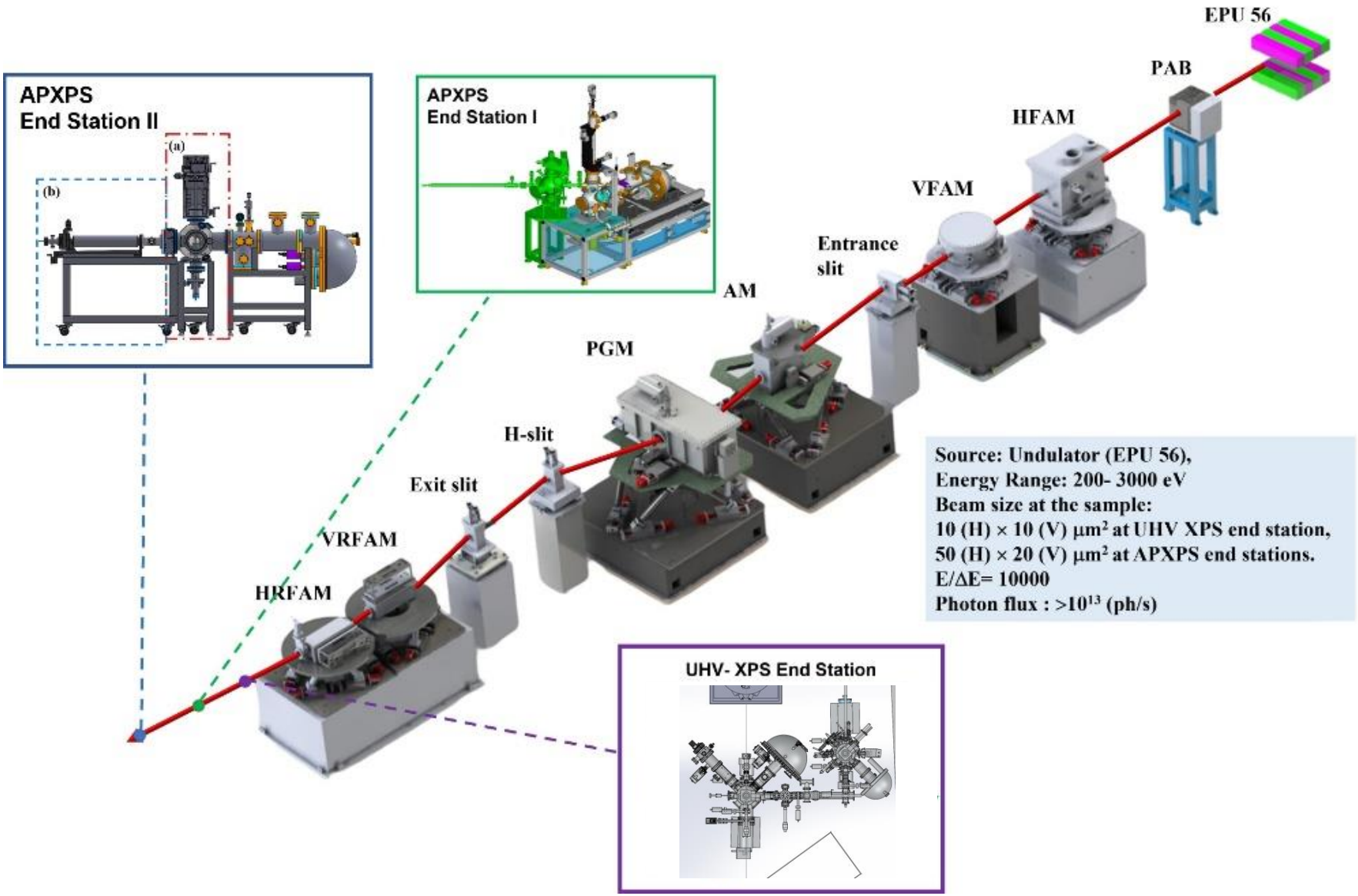

Variation of estimated photon flux with photon energy

Resolving power :10,000

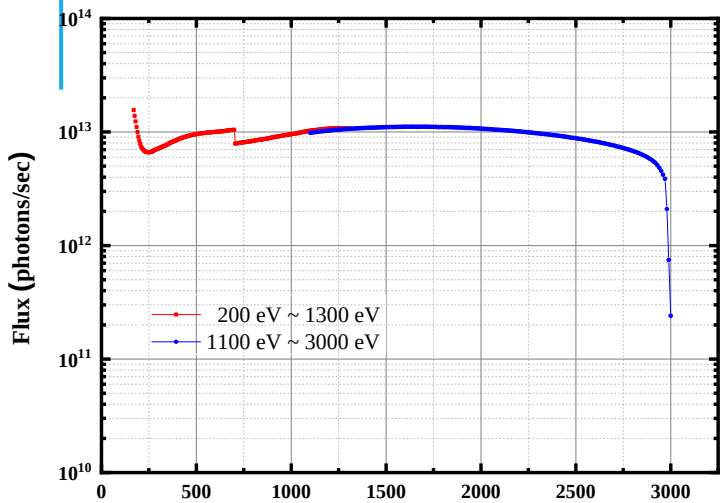

Resolving power :20,000

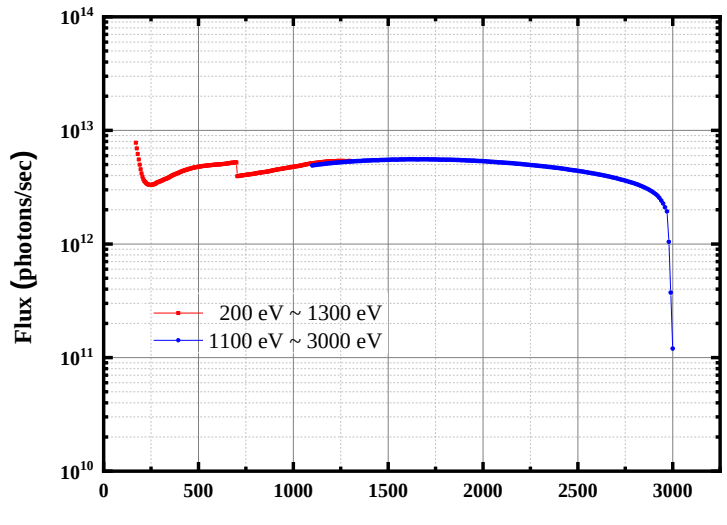

Data from Dr. C.-T. Chen

TLS BL24A

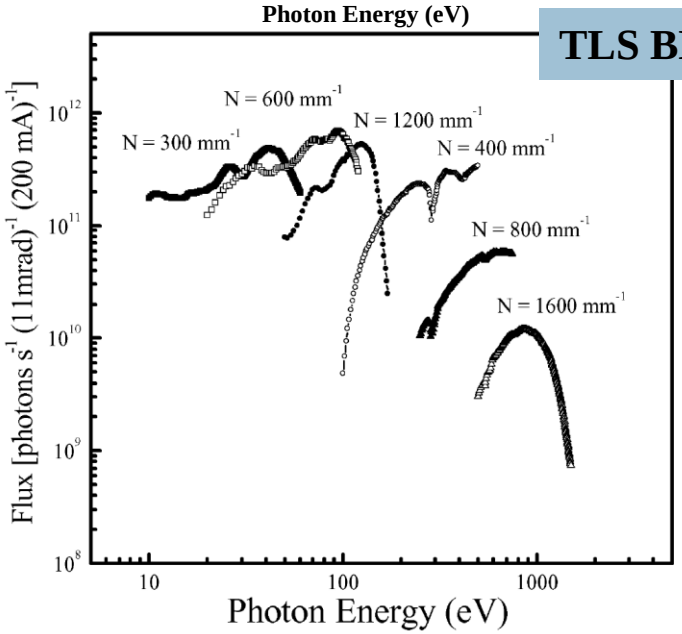

MAX-IV, HIPPIE

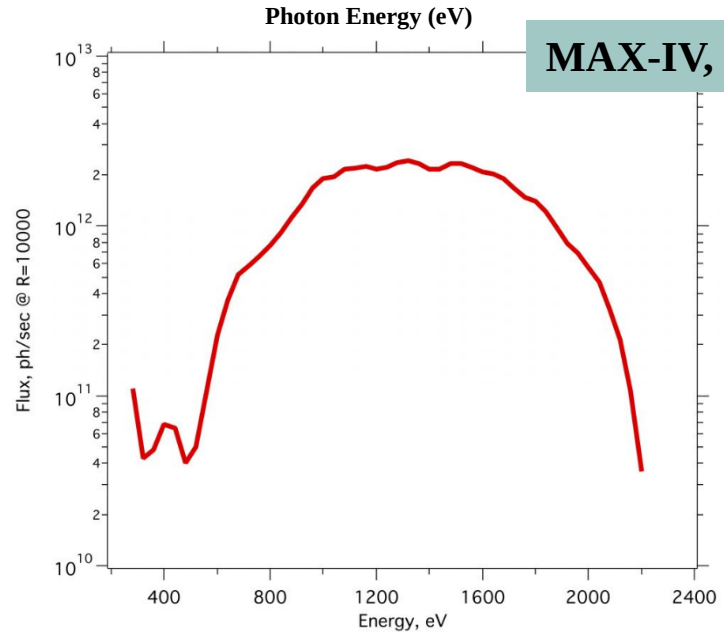

APXPS End Station I for Gas-Solid Reaction

Electron Analyzer	**SPECS PHOIBOS 150 Analyzer line detector**
Photon Energy	15- 1600 eV, (200- 3000 eV)*
Pressure	UHV to 10 mbar, (UHV to 100 mbar) *
Operating temperature range.	RT to 1073 K
Gases	N_2, O_2, H_2, CO_2, CO, Ar, H_2O(g), CH_3OH(g)
Surface science instruments	Ar+ sputter gun, H_2 cracker, LEED, Residual gas analyzer (RGA)
Ambient pressure XAS based on electron detection modes.	AEY, TEY
Applicable research area	Gas sensor mechanism, gas-solid heterogeneous catalysis such as carbon dioxide hydrogenation, photocatalytic reaction…., Alkali metal-air batteries charging and discharging reaction, …etc.

***Red highlight the changes expected when the existing APXPS end station at TLS BL24A is relocated to TPS 43A.**

Infrared reflection adsorption spectroscopy (IRRAS) and gas chromatography will also be included.

APXPS End Station II for Liquid-Solid Reaction

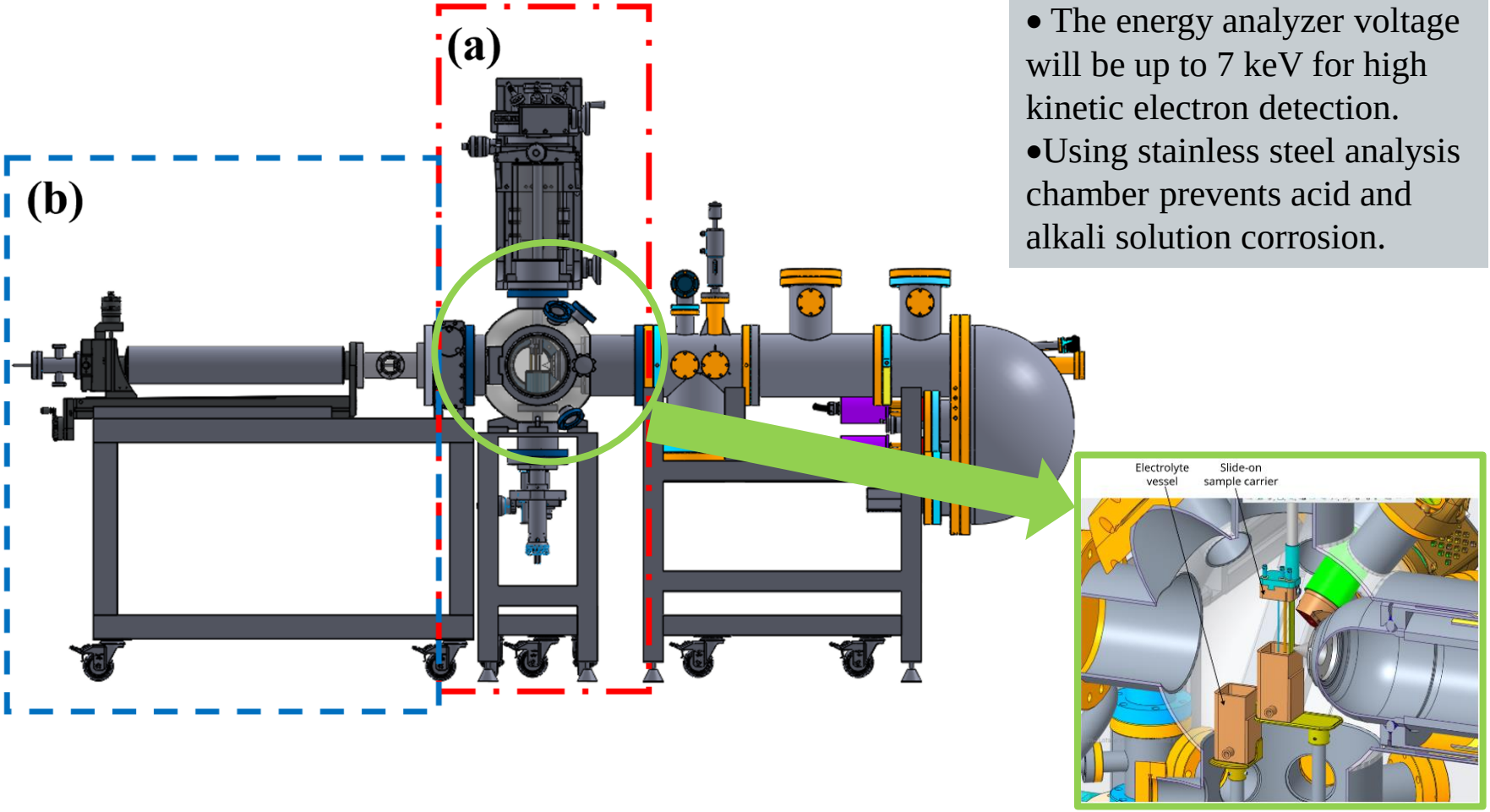

- The energy analyzer voltage will be up to 7 keV for high kinetic electron detection.
- Using stainless steel analysis chamber prevents acid and alkali solution corrosion.

(a)A dip-and-pull setup that works well with thick electrolyte layers.
(b) A liquid electrochemical cell with a polymer-based membrane for studying liquid-solid reactions with flow-thin electrolyte layers.

TPS 43A Ambient Pressure/UHV X-ray Photoelectron Spectroscopy

End stations Construction

Beamline Construction

EPU 56 construction

Front End, Completed. (2023.12.31)

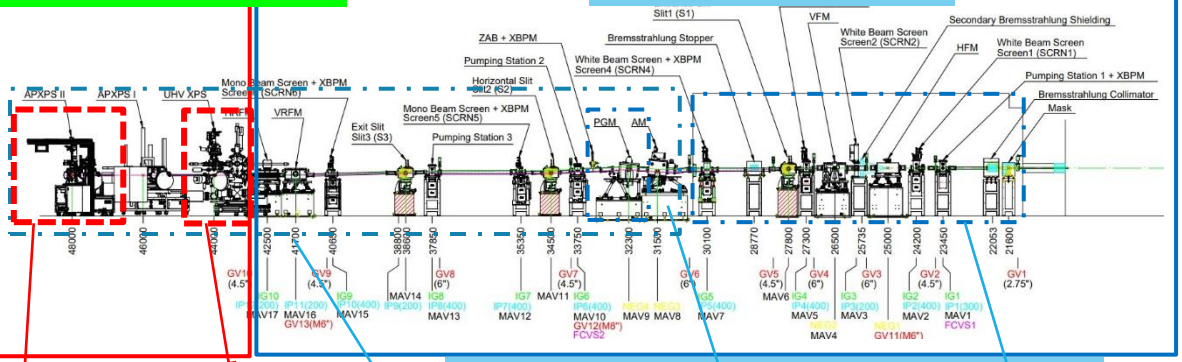

The detailed Optical layout is nearing the final decision.

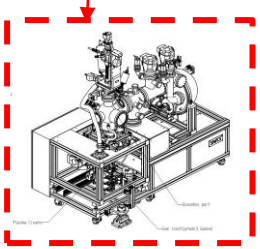

The liquid-solid APXPS system is expected to be delivered before Nov. 2025.

The UHV XPS analyzer is scheduled for delivery by the end of 2024.

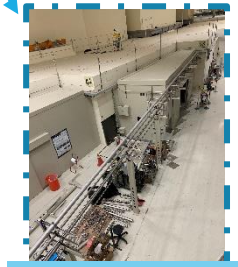

The beamline infrastructure and most of optic devices are currently under construction.

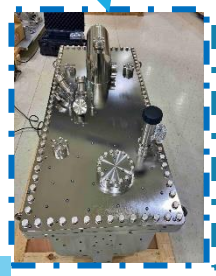

PGM chamber completed (2024.06.30)

Beamline Hutch completed (2023. 12. 31)

Assembly Completed in 2024.06.30.
Magnetic field measurement, and correction in laboratory are currently in process.
Installation in the storage ring is expected by the end of 2025.

Construction Plan and Current Progress of TPS 43A

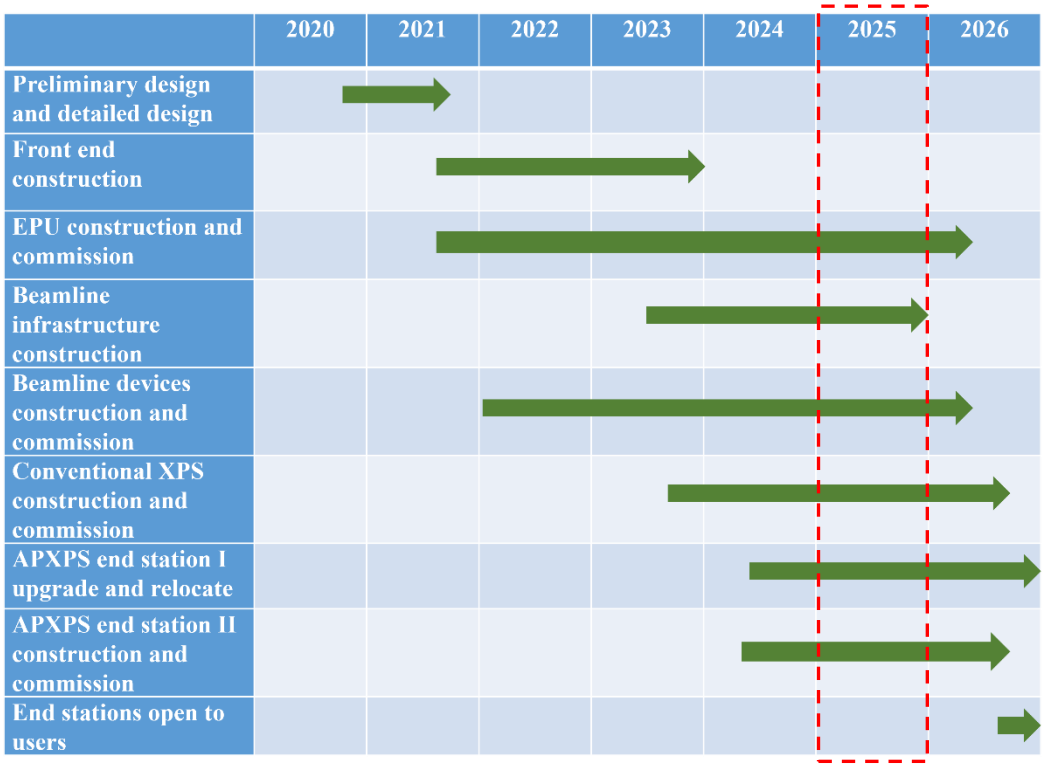

Beamline and End Stations Construction

This year, we plan to complete the beamline and end station constructions. We expect to start commissioning the beamline and end stations at the beginning of 2026 and open them to users in O3 or Q4 of the same year.

XPS Peak Fitting

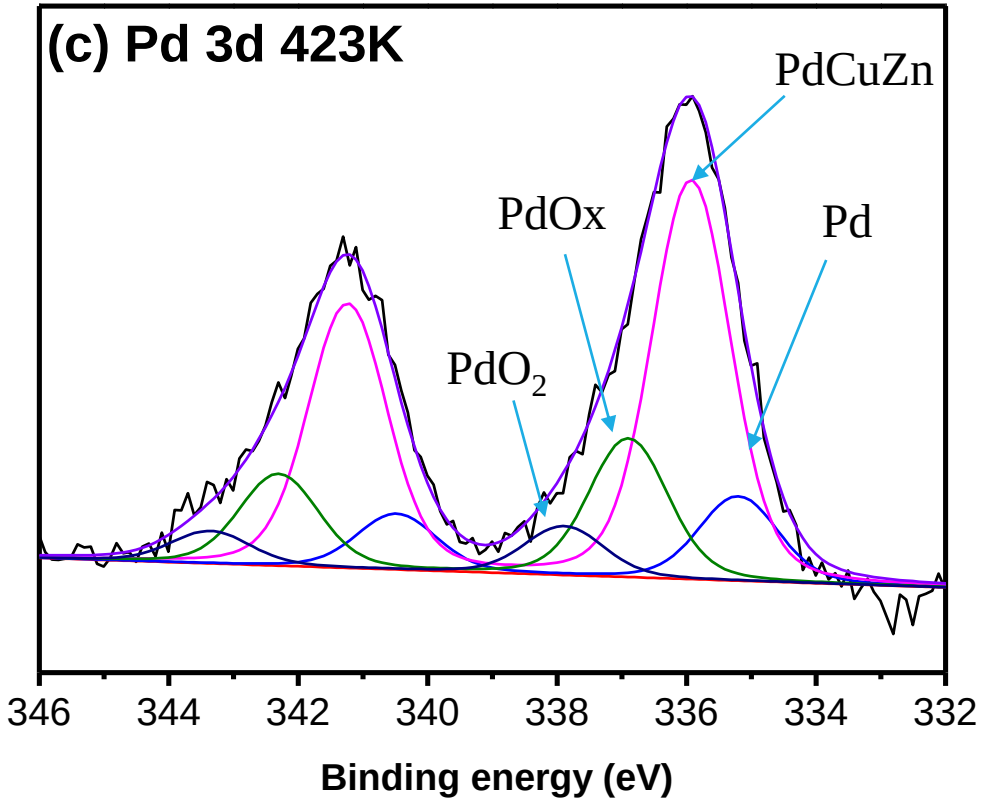

Software:
XPSPeak 4.1, CasaXPS, Unifit20XX

Background Modelling and Treatment

Type of background commonly used: constant, linear, polynomial, Shirley, Tougaard

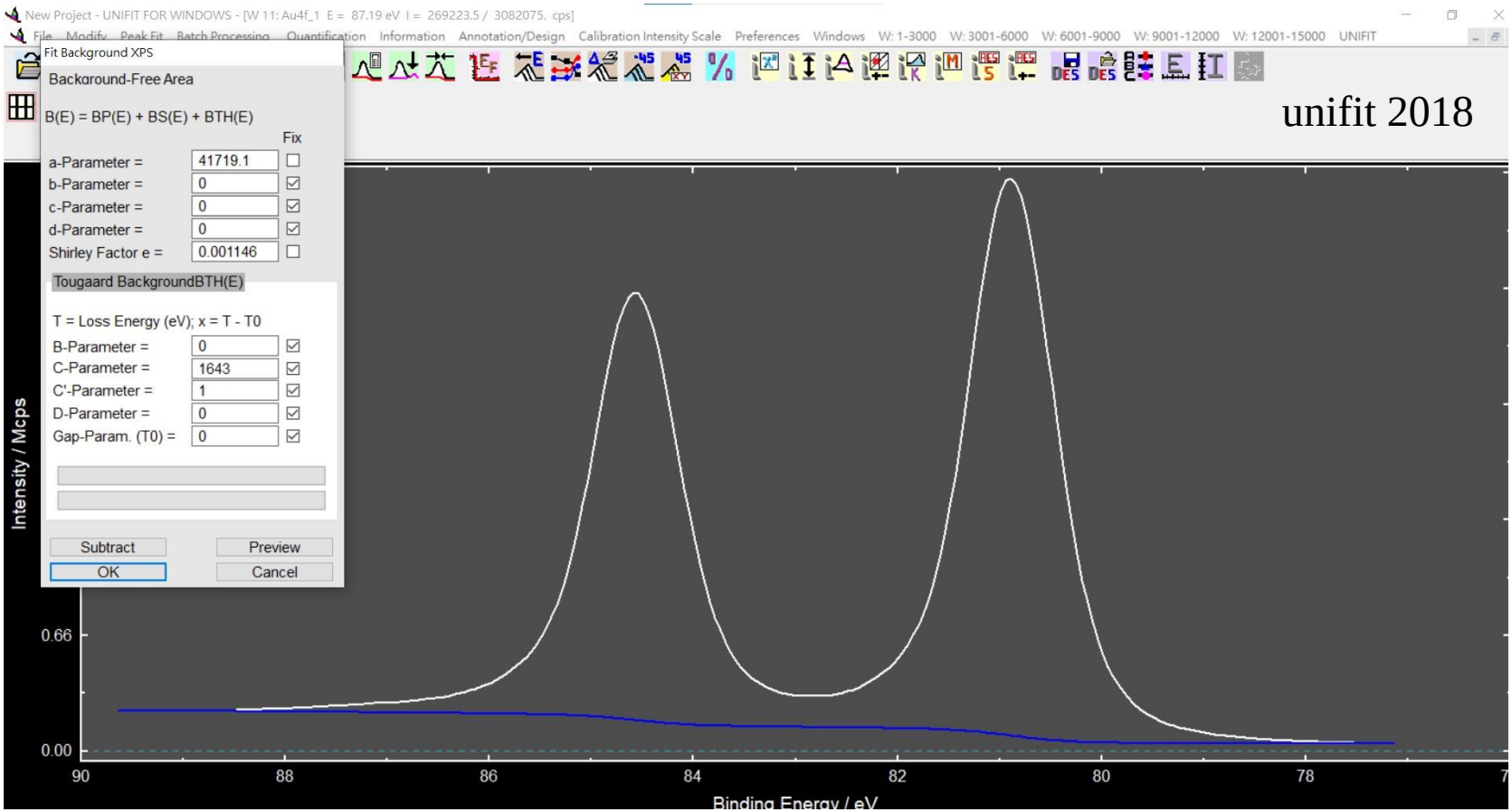

Constant Background:

$$B_C(E) = c$$

Linear Background:

$$B_L(E) = a(E_2 - E) + c$$

Polynomial Background:

$$B_P(E) = a' + b'(i_2 - i) + c'(i_2 - i)^2 + d'(i_2 - i)^3 .$$

Linear Background:
The linear background may be applied for spectra with small intensity differences between the low and high-energy side of the peak, e.g. for peaks derived from surface species, which are hardly affected by inelastic losses.

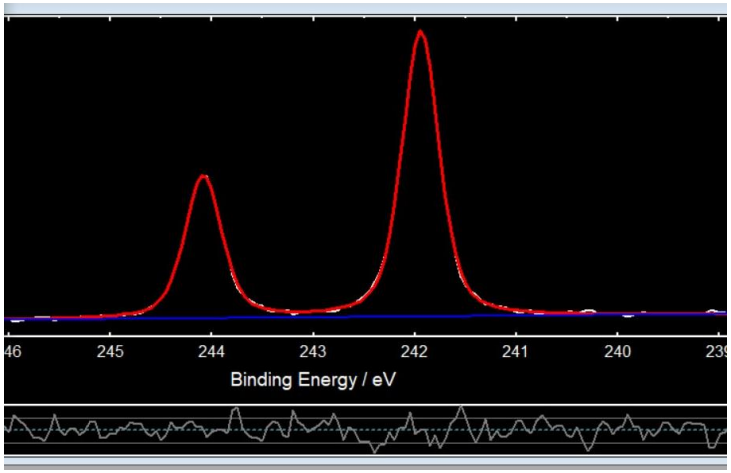

Shirley Background:
In many cases the Shirley model turned out to be a successful approximation for the inelastic background of core level peaks of buried species, which suffered significantly from inelastic losses of the emitted photoelectrons.

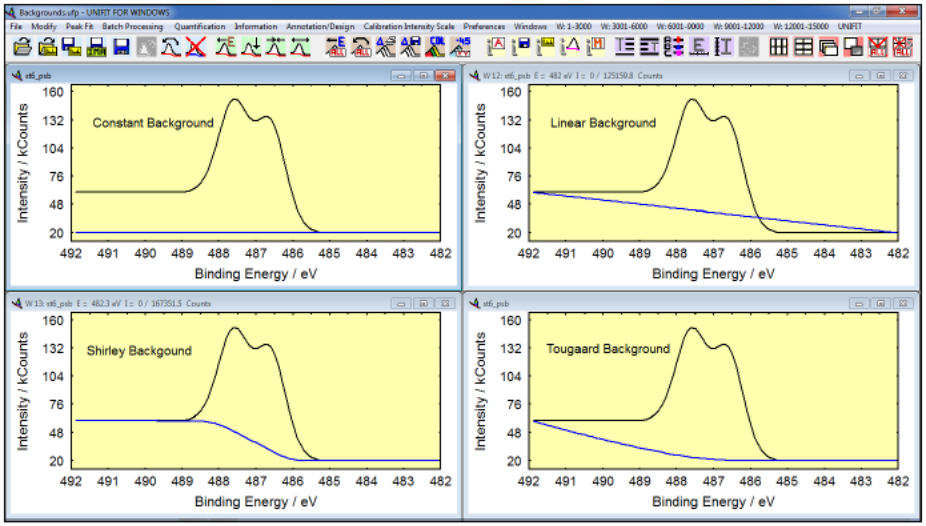

$$B_S(E) = \int_E^{\infty} F(E')dE' + c .$$

Tougaard Background:

The Tougaard background model has originally been developed as an alternative to the Shirley background for transition metals and is therefore especially suited for asymmetrical signals like metal 4f lines.

$$B_{TH}(E) = \lambda \int_{E}^{\infty} K(E'-E) M^{*}(E') dE' .$$

It integrates the experimental function while weighting it with a universal energy loss function *K(E)* and the inelastic mean free path of the electrons (λ) .

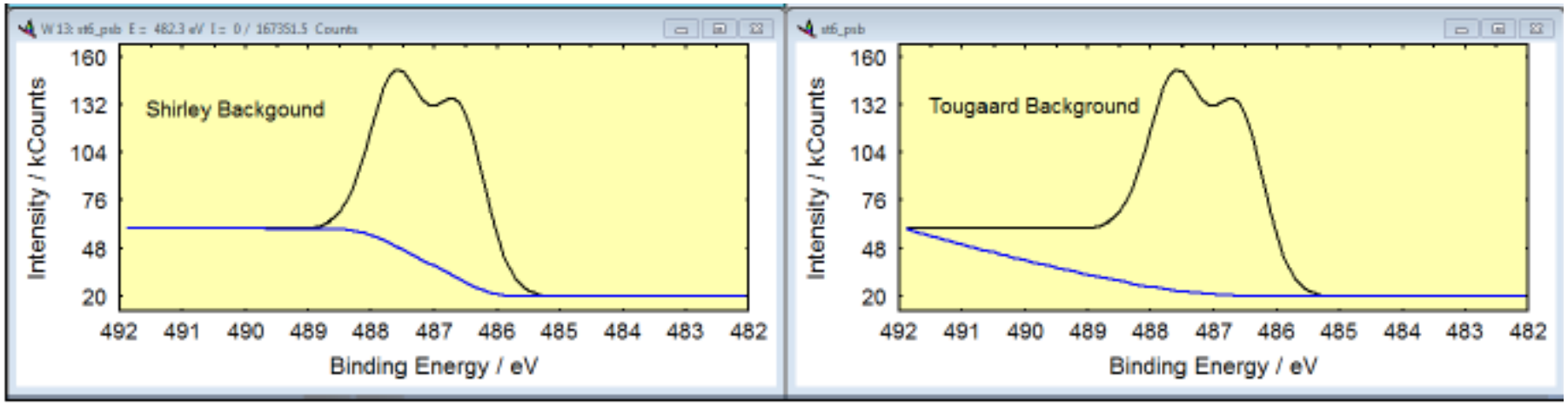

Modelling Peak shape

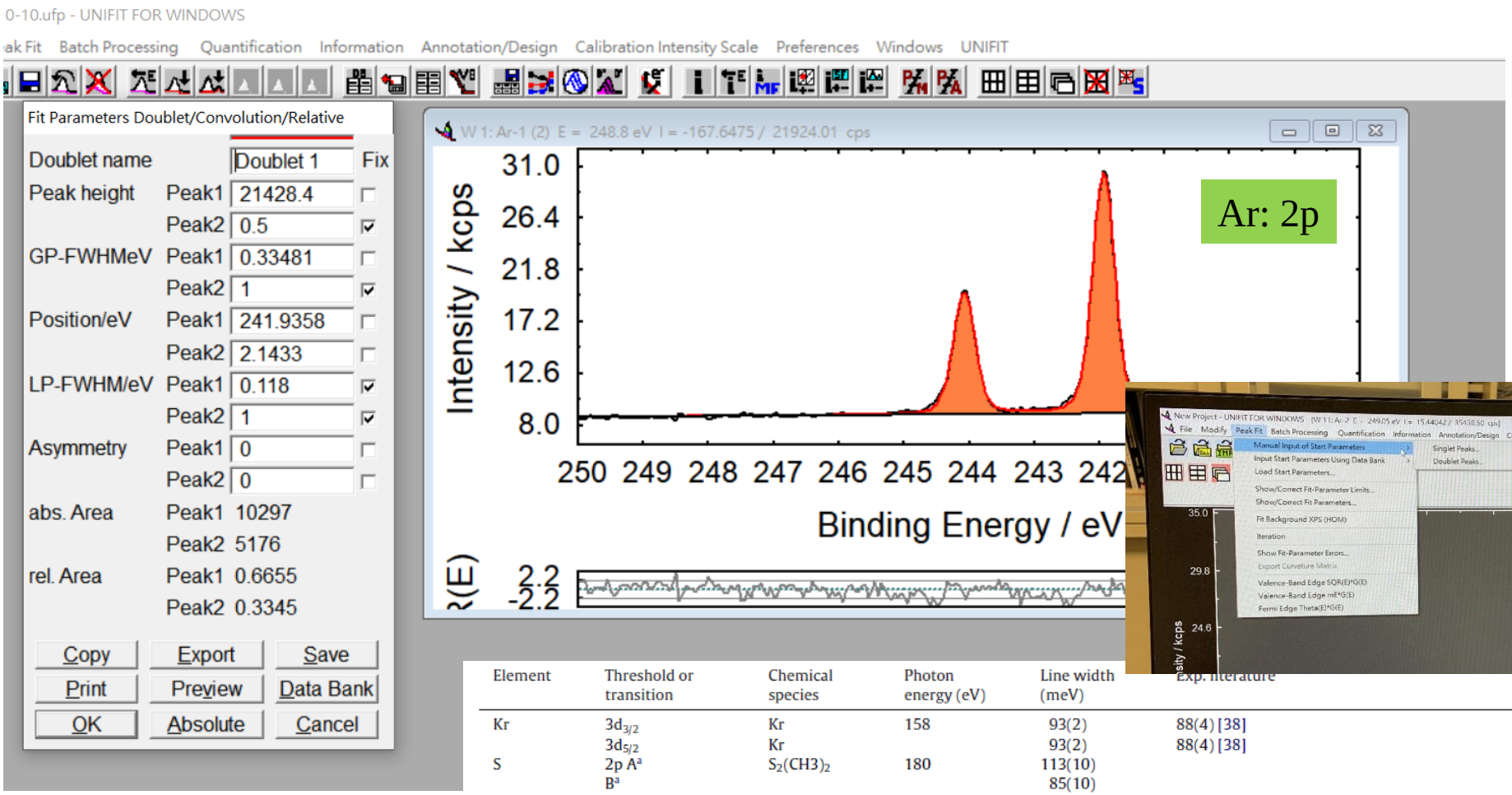

Element	Threshold or transition	Chemical species	Photon energy (eV)	Line width (meV)	Exp. literature
Kr	$3d_{3/2}$	Kr	158	93(2)	88(4) [38]
	$3d_{5/2}$	Kr		93(2)	88(4) [38]
S	2p A[a]	$S_2(CH3)_2$	180	113(10)	
	B[a]			85(10)	
	C[a]			105(10)	
B	1s	BF_3	370	71(4)	72(2) [14]
Cl	$2p\ (^2\Pi_{1/2})$	HCl	250	83(2)	84(9) [30]
	$2p\ (^2\Sigma_{1/2})$			81(5)	71(13) [30]
	$2p\ (^2\Pi_{3/2})$			100(5)	103(10) [30]
Ar	$2p_{1/2}$	Ar	400	116(2)	118(4) [38], 120 [39], 130(5) [40], 100(10) [41]
	$2p_{3/2}$	Ar		119(2)	118(4) [38], 120 [39], 130(5) [40], 110(10) [41]
Ar	$2p_{3/2} \rightarrow 4s$	Ar		109(2)	111(3) [42], 114(2) [43], 116(3) [44]
C	1s	CH_4	500	104(5)	95(2) [20], 83(10) [45], 120(10) [46], 107(10) [47]

Peak widths

Peak widths: The contributions that the intrinsic and instrumental effects make to the peak width are given, to a first approximation, by:

$$\mathrm{FWHM_{tot}} = (\mathrm{FWHM}_n^2 + \mathrm{FWHM}_x^2 + \mathrm{FWHM}_a^2 + \mathrm{FWHM}_{ch}^2 + \cdots)^{1/2} \quad (3.12)$$

where FWHM is the full-width at half-maximum of the observed peak (tot), core hole lifetime (n), X-ray source (x), analyzer (a), and charging contribution (ch).

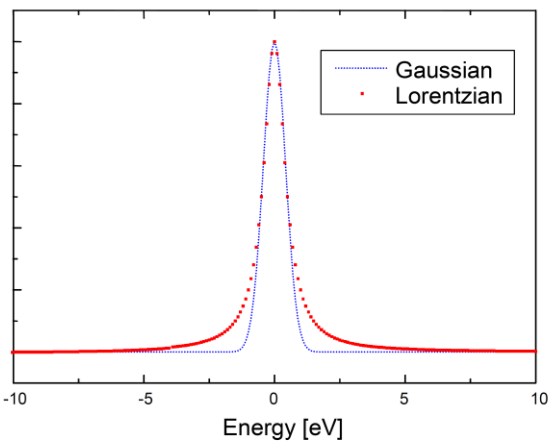

Fig. 3. Comparison of Gaussian and Lorentzian function (FWHM = 1 eV)

$$L(E) = \left\{1 + \left[\frac{(E - E_0)}{\beta}\right]^2\right. \quad G(E) = \exp\left\{-\ln 2 \frac{(E - E_0)^2}{\beta^2}\right\}$$

β, i.e. half of the full width at half maximum (FWHM), and E_0, the peak position.

Lorentzian width (Γ): is related to lifetime of the core hole state by Heisemberg's Uncertainty Principle. $\Gamma = h/\tau$, h is the Plank constant

Gaussian width (G): is related to instrument factors, for example x-ray source resolution, analyzer resolution, thermal broadening

Lifetime of the core hole—the natural linewidth

τ For s< p < d

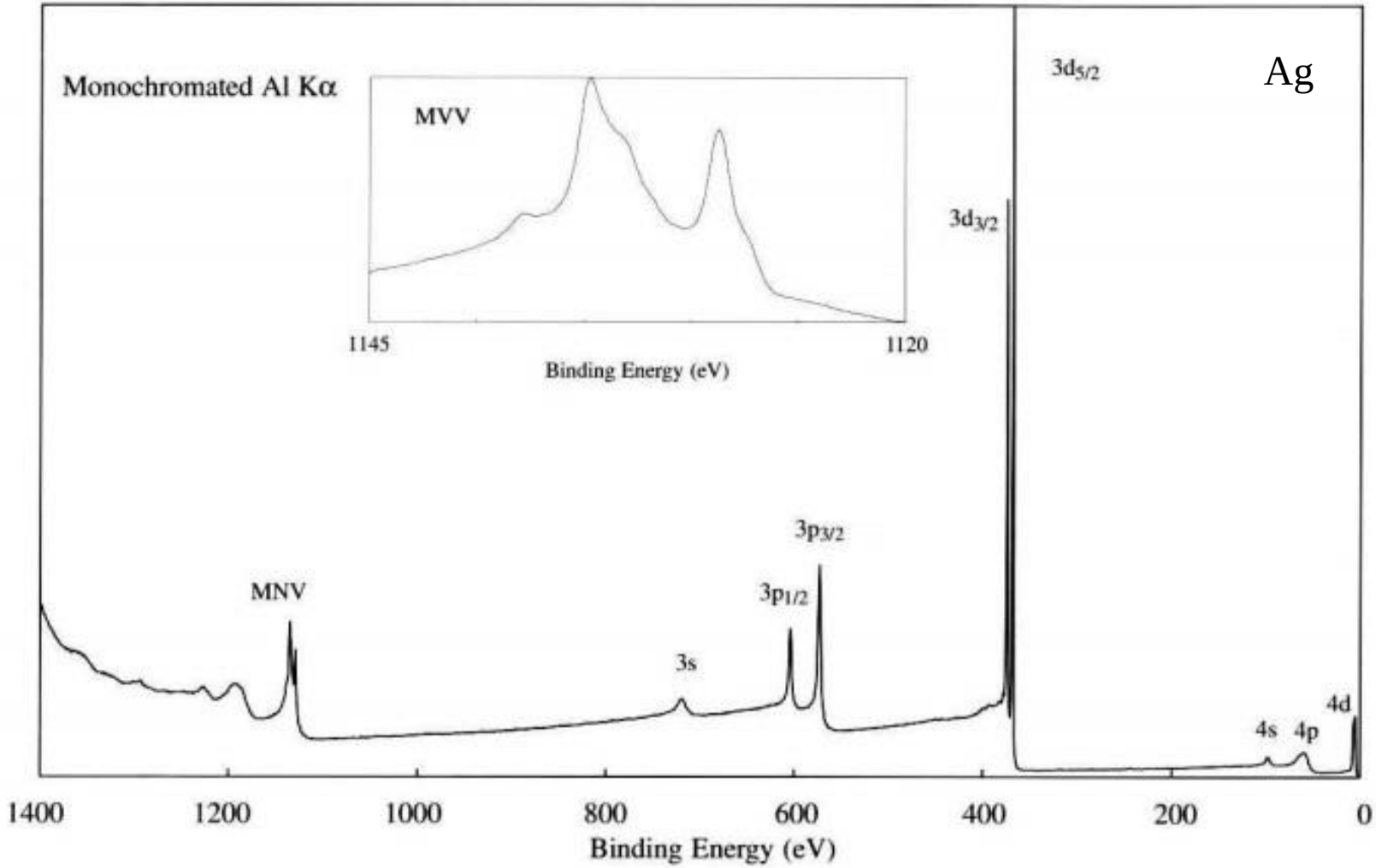

Natural linewidth of Au $4f_{7/2}$, Ag $3d_{5/2}$, Cu $2p_{3/2}$

TABLE V. Results of *simultaneous* least squares fits to data at all takeoff angles. All quoted error limits include estimates of reproducibility.

	Hole-state lifetime Γ (eV)	Singularity index α	Gaussian broadening Γ_G (eV)	Surface-bulk shift $\Delta_{s,b}$ (eV)
Au $4f_{7/2}$	0.339±0.02	0.048±0.006	0.276±0.03[a]	−0.389±0.01
Ag $3d_{5/2}$	0.274±0.01	0.066±0.006	0.262±0.03[a]	−0.076±0.03
Cu $2p_{3/2}$	0.595±0.01	0.042±0.006	[0.230][b]	−0.241±0.02

[a]Average of angle-dependent values.
[b]Constrained.

PHYSICAL REVIEW B, 1983, 27, 3160.

Product and Sum Function

A frequently used approach to describe XPS core level lines or XAS line has been the product or sum of Gaussian and Lorentzian functions of the same width

Product:

$$f(E) = h \cdot \left\{ 1 + M_V \cdot \left[\frac{E - E_0}{\beta + \alpha(E - E_0)} \right]^2 \right\}^{-1} \cdot \exp\left\{ -(1 - M_V) \cdot \ln 2 \cdot \left[\frac{E - E_0}{\beta + \alpha(E - E_0)} \right]^2 \right\}.$$

Sum:

$$f(E) = h \cdot M_V \cdot \left\{ 1 + \left[\frac{E - E_0}{\beta + \alpha(E - E_0)} \right]^2 \right\}^{-1} + h \cdot (1 - M_V) \cdot \exp\left\{ -\ln 2 \cdot \left[\frac{E - E_0}{\beta + \alpha(E - E_0)} \right]^2 \right\}.$$

XPSpeak Fit, CasaXPS

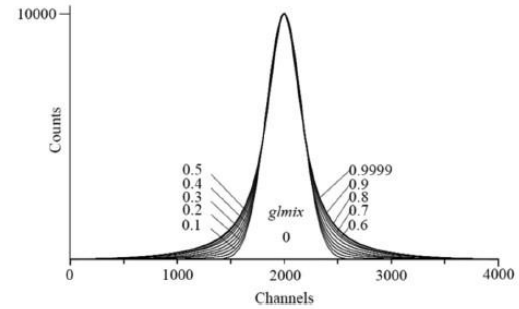

FIG. 2. Plot of Voigt functions that can be used to describe the shape of XPS peaks. The functions are calculated for a single peak with an FWHM of 400 channels and a peak maximum of 10 000 counts over a range of 4001 channels, 2000 channels to the right and left of the peak. When these parameters take a value of 0, the peak is a pure Gaussian. When they take a value of 1, the peak is a pure Lorentzian (Ref. 21).

J. Vac. Sci. Technol. A **38**, 061203 **(2020)**.

Convolution Function (Voigt profile)

A more adequate description of the photoelectron- or X-ray absorption spectra line shape may be obtained by convoluting Gaussian and Lorentzian (or Doniach-Sunjic (DS) type) contributions rather than by simply product and sum function.

$$f(E) = f(L * G) = \int_{-\infty}^{\infty} L(E')G(E - E')dE' \ .$$

Unifit 20XX

$$F_V \approx 0.5346 F_L + \sqrt{0.2166 F_L^2 + F_G^2}$$

Determine the Instrument Resolution by using Au foil

Grating 800 line/mm, Photon Energy 340 eV,
entrance silt and existing silt= 20 um, Pass Energy=10 eV

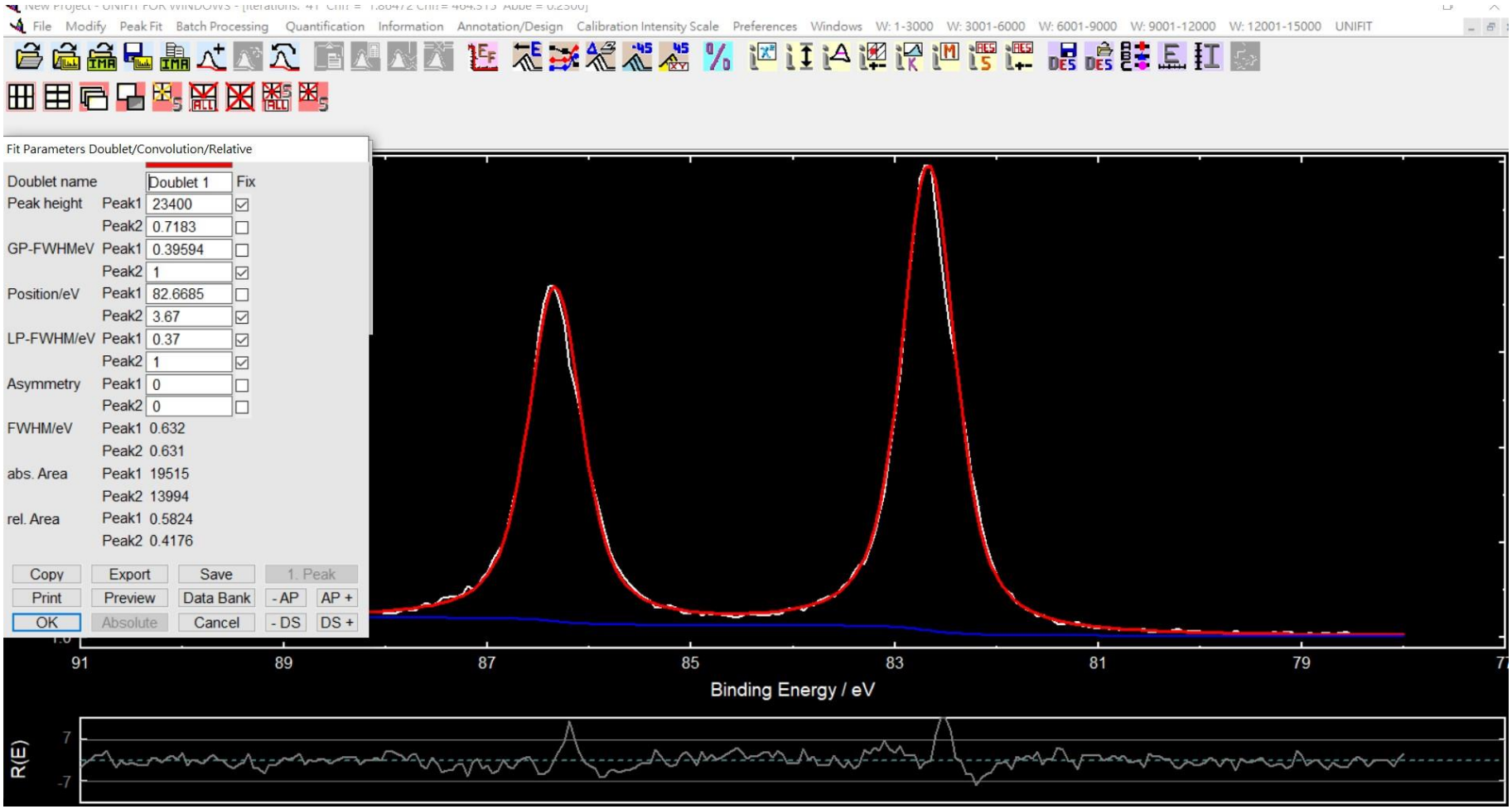

Asymmetric function: Doniach-Sunjic form

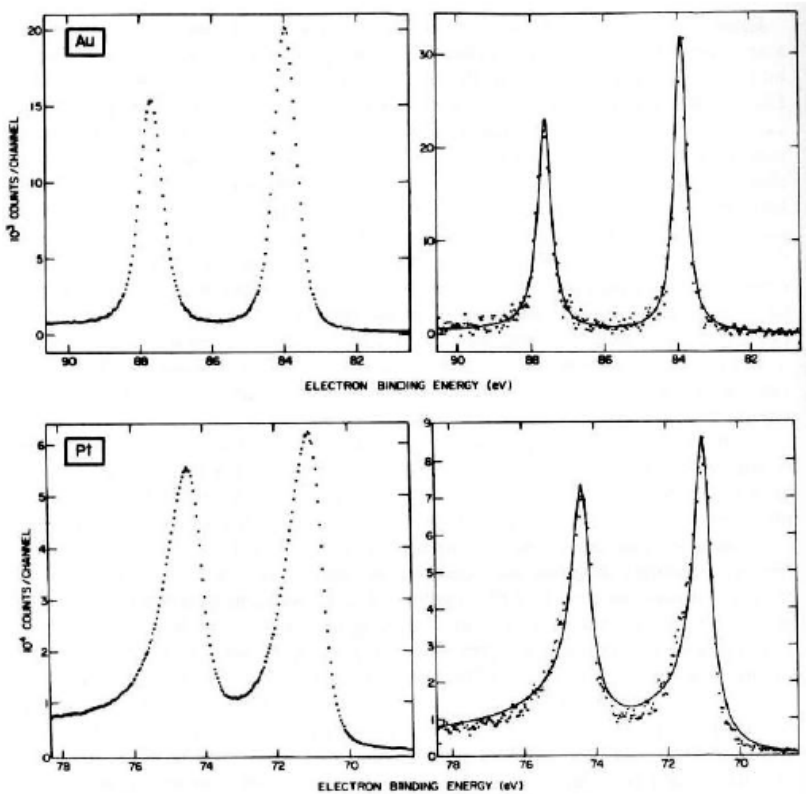

Fig. 37. 4*f* core spectra from polycrystalline Au and Pt (points) in comparison to a best fit of the asymmetric line shape predicted by Eq. (158) (curves). In the right panels, the data have been corrected by deconvolution of the instrumental line shape, but no correction for inelastic scattering effects has been made. The instrumental line shape was derived from the form of the cut-off near E_F (cf. Fig. 13). (From Hüfner and Wertheim, ref. 84.)

Creation of electron-hole pairs results in an askew background like those shown on the left.

$$I(E) = \frac{\cos\left[\pi\alpha/2 + (1-\alpha)\tan^{-1}(E/\gamma)\right]}{\left(E^2+\gamma^2\right)^{(1-\alpha)/2}}$$

where $\boldsymbol{E}$ = kinetic energy of the electron, γ = lifetime width of core hole, and $\boldsymbol{\alpha}$, asymmetry parameter,

$$\alpha = 2\sum_l (2l+1)(\delta_l/\pi)^2$$

with δ_l = phase shift of the *l*th partial wave for electrons at the Fermi energy scattering from the core hole.

In the limit of $\alpha \rightarrow 0$, DS line shape becomes a Lorentzian form.

Doniach, S.; Sunjic, M., Many-electron singularity in x-ray photoemission. *J. Phys. C* **1970,** *3*, 285-291.

Courtesy to Dr. Yaw-Wen Yang

CRITERION FOR GOODNESS OF FIT

Chi-square

Nonlinear least-square fitting method is aimed at ***a minimization of chi-square***. If the differences between the experimental spectrum *M(i)* and the calculated spectrum *S(i, **p**)* are *independent* and *distributed homogeneously (Abbe criterion)*, then fitting can be considered satisfactory. In that case only statistical measuring errors, i.e. following Poisson distribution, remain.

$$S(i,\vec{p}) = \sum_{j=1}^{k} SC_j(i) + B(i),$$

where *S(i, **p**)* is the sum over *k* fitted components, SC_j at data point *i*, and *B(i)* is the background at point i.

Chi-square, χ^2 is defined as

$$\chi^2(\vec{p}) = \sum_{i=1}^{N} \frac{(S(i,\vec{p}) - M(i))^2}{M(i)},$$

where *M(i)*, the measured value at *i*.

The **reduced Chi-square** χ^{2*} is the chi-square further divided by the degree of freedom,

$$\chi^{2*}(\vec{p}) = \frac{\chi^2}{N - F - 1}.$$

where here N is the number of data points, and F is the total number of fit parameters. The expected value of χ^{2*} **is about 1**.

GOODNESS OF FIT

Residual function:

The residual ***R*** expresses **the deviation** between sum curve and experimental data.

A normalized residual is defined as,

$$R(i) = \frac{S(i, \vec{p}) - M(i)}{\sqrt{M(i)}}.$$

where *M(i)* is the measured value in counts, and *S(i, **p**)* is fitted values. The normalization with the square root of intensity was introduced in order to obtain the same weight of errors for the complete spectrum.

An *ideal fitting* should give rise to a featureless residual function across the data range with its range not exceeding one std. deviation.

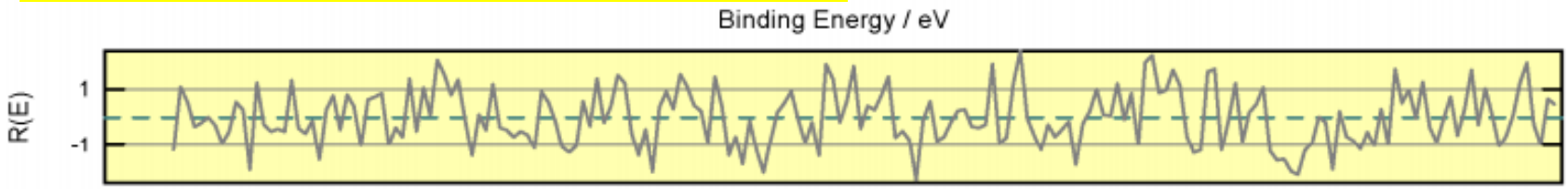

***Abbe* Criterion** is a mean to estimate the extent of *systematic* errors,

$$Abbe = \frac{1}{2} \frac{\sum_{i=1}^{N} (R'(i+1) - R'(i))^2}{\sum_{i=1}^{N} (R'(i))^2}.$$

A value of 0 pinpoints systematically correlated deviations; a value of 1 indicates statistical deviations and a value of 2 is obtained in case of systematically anti-correlated deviations. The expected value of *Abbe* is 1.

A spectrum with a satisfactory fit

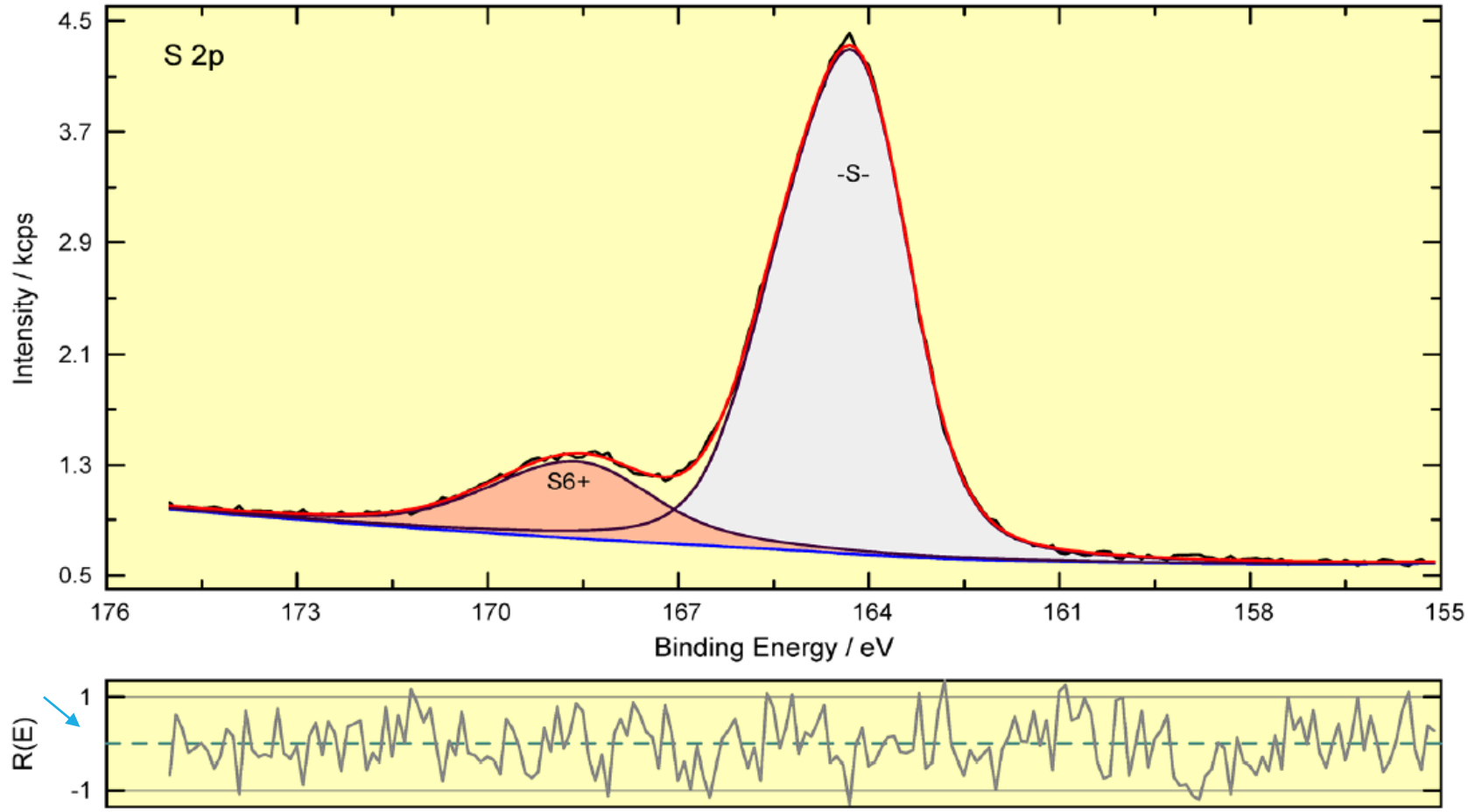

Fit Parameters Doublet/Convolution/Relative

Doublet	Fix	Peak height	Fix	Gauss	Fix	Energy	Fix	Lorentzian	Fix	Asym.	FWHM	abs. Area	rel. Area
1/1	0	3050.2	0	1.579	0	164.0822	0	0.50294	1	0	1.866	6647	0.552
1/2	1	0.5	1	1	1	1.2	1	1	1	0	1.866	3324	0.2761
2/1	0	0.14145	1	1	0	4.2411	0	2.93064	1	0	2.511	1383	0.1148
2/2	1	0.5	1	1	1	1.2	1	1	1	0	2.511	687	0.0571

Fit Background: a= 587.1065 b=-0.4407 c= 0.011 d= 0 e= 0.0003 B= 0 C= 1643 C'= 1 D= 0 T0= 0

Chi^{2*} = 1.113

Chi^2 = 194.9

Abbe = 0.8

A Satisfactory fit

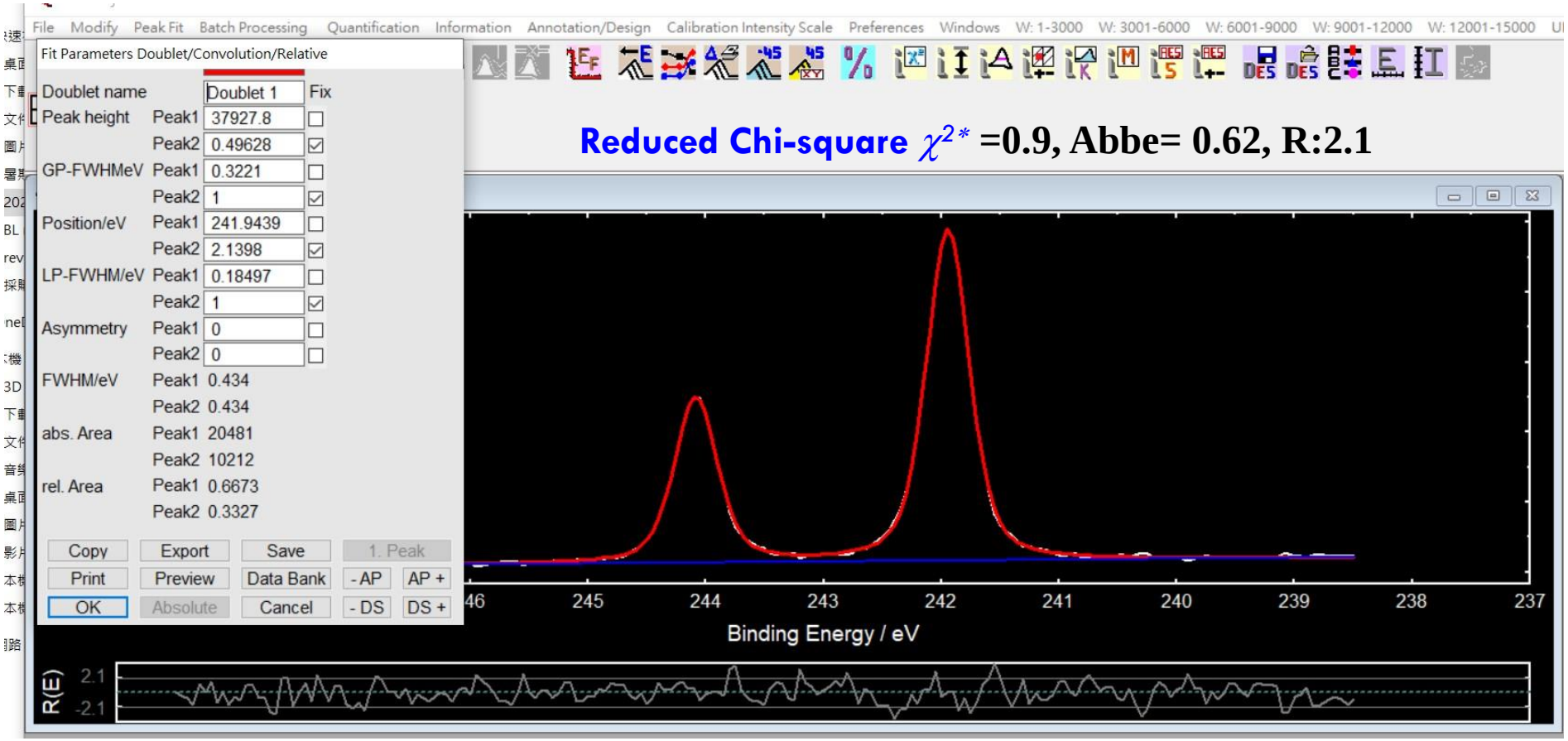

Linear Background- Au4f

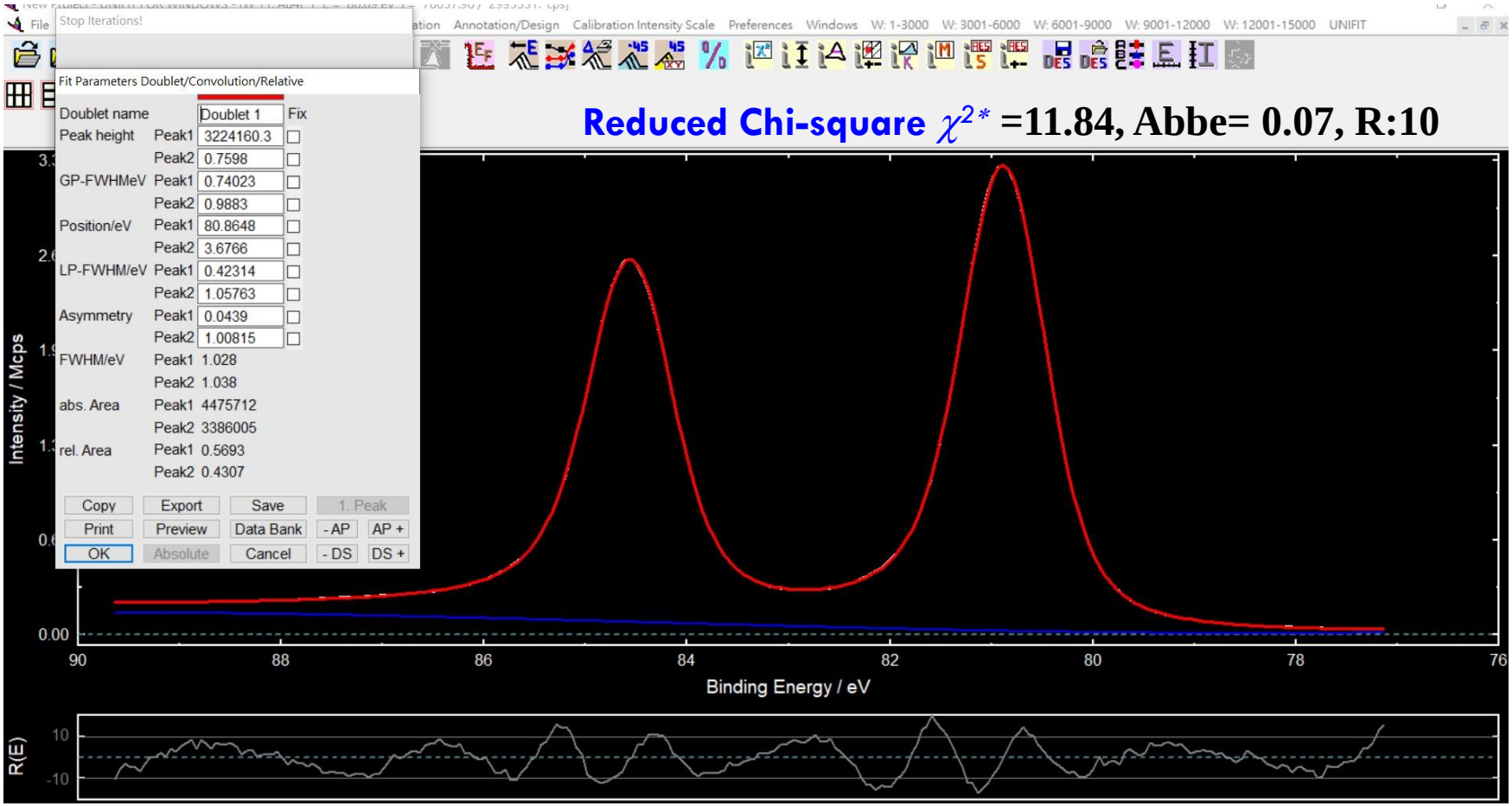

Shirley Background- Au4f

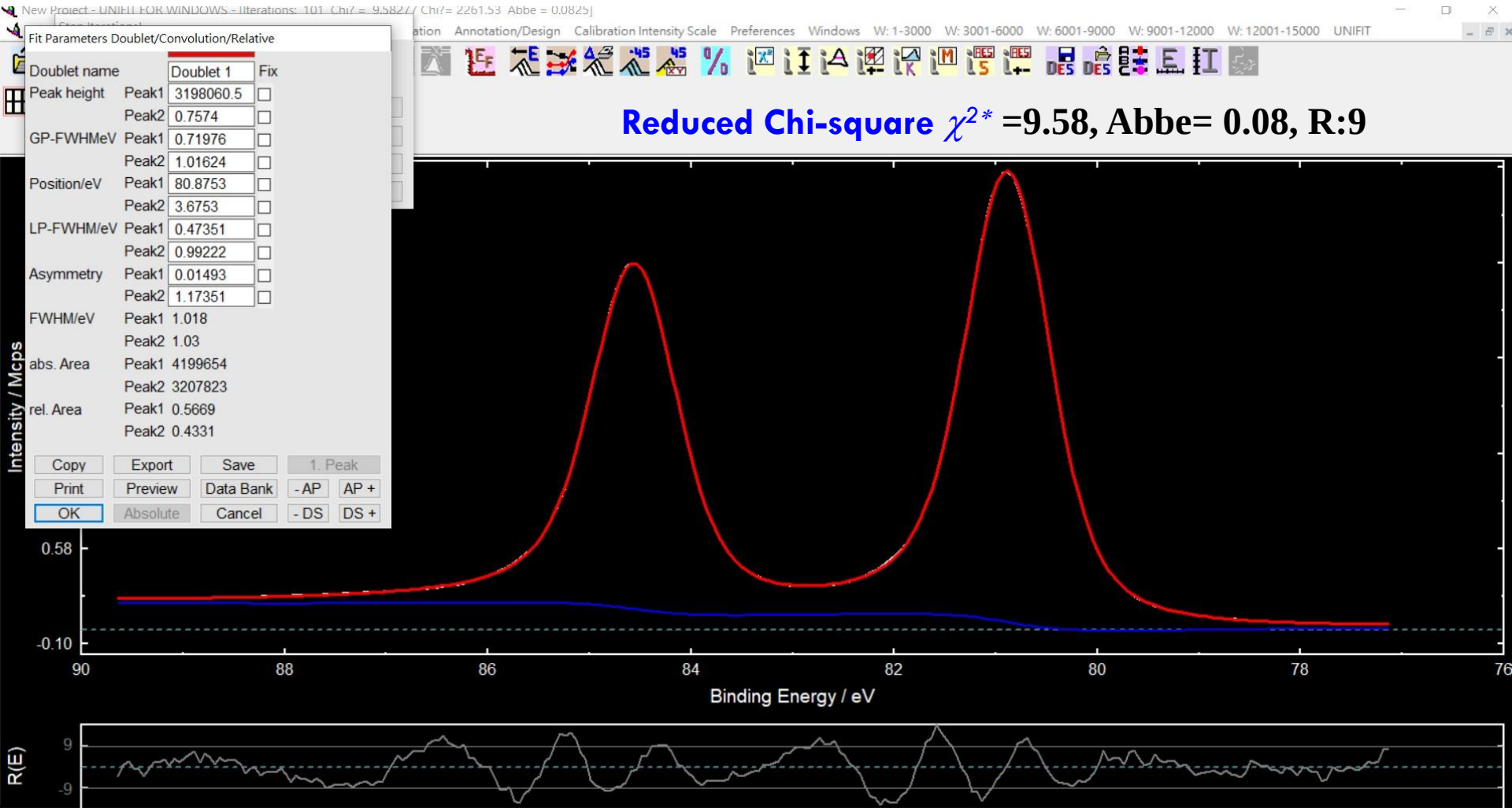

Shirley Background+ Tougaard- Au4f

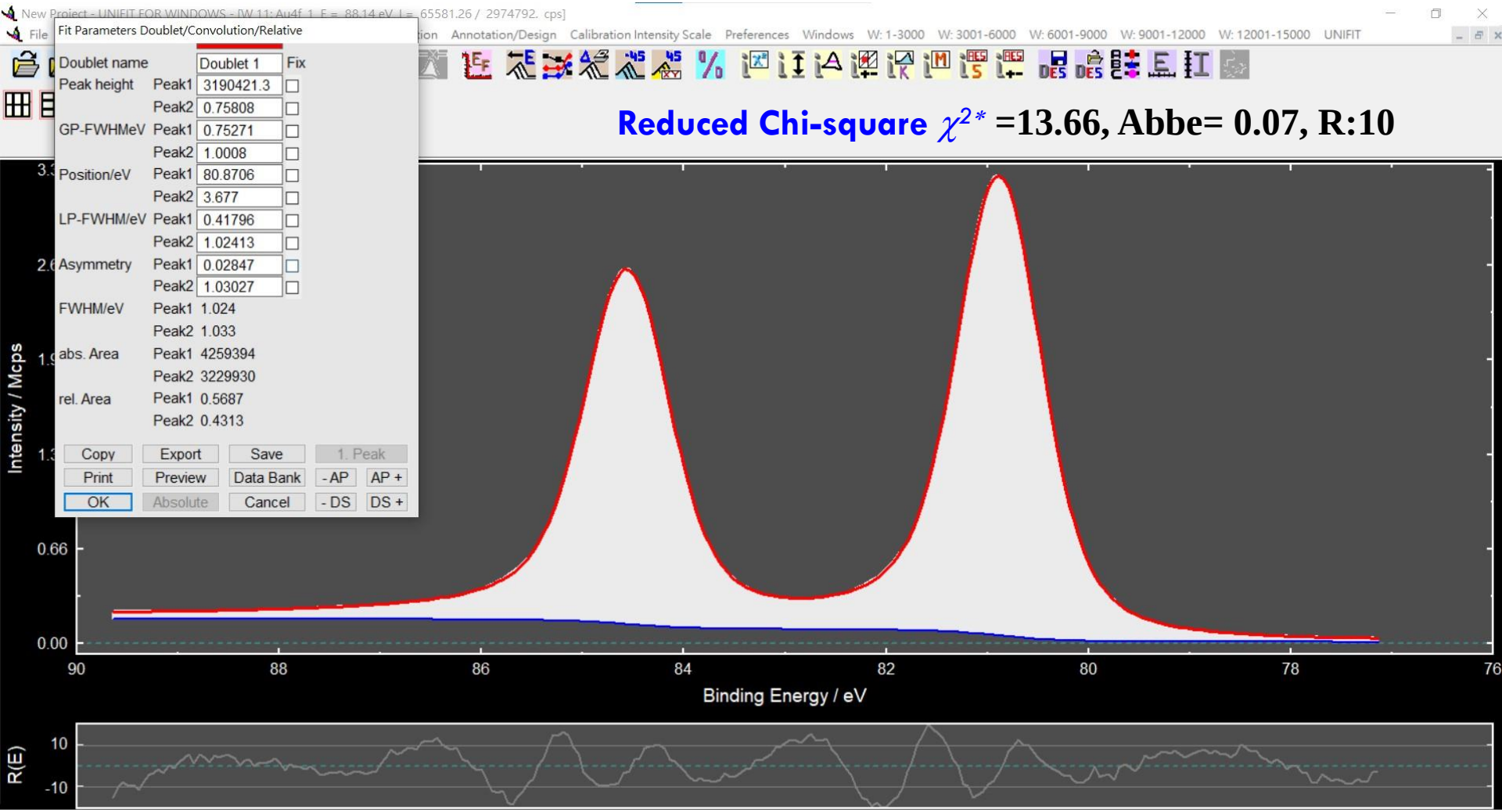

General guidelines of choosing the fitting parameters

- Start with a minimal number of fitted components based on the discernible number of peaks. Increase the number of fitted components when the fitting runs aground, justifying additional components.

- A fit with a smallest chi-square, achieved by invoking too many peaks, may not necessarily be a good fit. The existence of fitted components needs to *based on science, not mathematics*, and *make good scientific sense*.

The End ~ Thank You !!

Contact information：
E-mail: wang.ch@nsrrc.org.tw
Phone: 03-5780281, Ext:7323 (O),
3175 (Lab.), 1241 (End Stations)

References:

1.augustus.scs.uiuc.edu/nuzzogroup
2. www.cem.msu.edu/~cem924sg
3.Handbook of X-ray Photoelectron Spectroscopy (Perkin-Elmer Co.)
4*John C. Vickerman, and Ian S, Gilmore, “Surface Analysis The Principal Techniques”
5. Manual Unifit 2022
6. Practical guide for curve fitting in X-ray photoelectron spectroscopy,
J. Vac. Sci. Technol. A **38**, 061203 **(2020)**.